

MECHANISTIC STUDIES OF LIGAND CONTROLLED SELECTIVITY
IN GOLD AND PALLADIUM CATALYZED REACTIONS

by

Zachary Louis Niemeyer

A dissertation submitted to the faculty of
The University of Utah
in partial fulfillment of the requirements for the degree of

Doctor of Philosophy

Department of Chemistry

The University of Utah

December 2017

Copyright © Zachary Louis Niemeyer 2017

All Rights Reserved

The University of Utah Graduate School

STATEMENT OF DISSERTATION APPROVAL

The dissertation of Zachary Louis Niemeyer

has been approved by the following supervisory committee members:

Matthew S. Sigman, Chair 10/09/2017
Date Approved

Ryan E. Looper, Member 10/09/2017
Date Approved

Janis Louie, Member 10/09/2017
Date Approved

Ryan P. Steele, Member 10/09/2017
Date Approved

Eric W. Schmidt, Member 10/09/2017
Date Approved

and by Cynthia Burrows, Chair/Dean of

the Department/College/School of Chemistry

and by David B. Kieda, Dean of The Graduate School.

ABSTRACT

Linear free energy relationships have been a staple of reaction mechanistic studies for nearly 100 years, enabling the quantification of subtle steric and electronic interactions between ligand, catalyst, and substrate. Recent work has offered an integrated approach to both interrogate reaction selectivity origins and to predict more optimal conditions. Classic and modern approaches to analyze ligand effects are presented in Chapter 1.

Chapter 2 focuses on the development of novel descriptors for monodentate phosphine ligands. The application of these parameters to a Suzuki reaction was complicated by multiple ligation states of the catalyst. Experimental outcomes indicated that two catalyst regimes are present in the reaction; thus, separation of the results into subclasses was necessary. Doing so simplified the selectivity models, revealing nuanced ligand effects that were quantified with the new parameters.

Further applications of these phosphine descriptors are detailed in Chapter 3. First, two gold-phosphine catalyzed cycloisomerization reactions are investigated using physical organic techniques along with reaction selectivity correlations. Overall, these data are used to identify the origin of ligand induced chemoselectivity, and to predict a novel ligand to increase the desired product ratio. Second, studies of an alkyl-aryl Suzuki reaction are described. In this instance, the phosphine ligand is shown to affect the enantiospecificity and chemoselectivity in two different fundamental steps. Evidence of

the role ligand size and electronics play in directing the reaction pathways are presented.

Chapter 4 details our team's efforts to identify a catalyst system that favors the atypical oxidative addition pathway within a Buchwald-Hartwig coupling reaction of differentially halogenated hetero-aromatics. Bidentate phosphine ligands were found to induce moderate selectivity; thus, ligand parameterization was utilized. Guided by univariate correlations, an exceedingly selective diaminophosphine ligand was successfully predicted, the origins of which were additionally analyzed with density functional theory (DFT) calculations.

Using similar multivariate techniques, Chapter 5 presents the parameterization of acyclic diaminocarbene ligands developed in the context of a gold-catalyzed rearrangement-cyclization reaction. Enantioselectivity in this case was found to be highly sensitive to two substituents on the ligand, and quantification of these effects enabled the identification of a reaction system that produces highly enantioenriched products.

TABLE OF CONTENTS

ABSTRACT.....	iii
LIST OF TABLES.....	vii
LIST OF FIGURES.....	ix
LIST OF ABBREVIATIONS.....	xiii
ACKNOWLEDGEMENTS.....	xviii
Chapters	
1. INTRODUCTION.....	1
Phosphine Descriptors.....	3
Multivariate Analysis.....	10
Model Development.....	19
Conclusions.....	21
References.....	22
2. DEVELOPMENT OF PHOSPHINE PARAMETERS AND APPLICATION TO AN ARYL-ARYL SUZUKI COUPLING REACTION.....	26
Introduction.....	26
Experimental Analysis and Multivariate Modeling of Observed Ligand Effects....	37
Mechanistic Interrogation and Reanalysis.....	44
Experimental.....	53
References.....	80
3. MECHANISTIC INTERROGATION OF THREE REACTIONS USING NEWLY DEVELOPED PHOSPHINE PARAMETERS.....	84
Ligand Effects in Gold-Catalyzed Cycloisomerization Reactions.....	85
Interrogating Alkyl-Aryl Suzuki Reaction Pathways.....	100
Experimental.....	112
References.....	121
4. SELECTIVE AMINE ARYLATION WITH MULTIPLY HALOGENATED	

PYRIDINES.....	127
Introduction.....	127
Bidentate Ligand Parameterization Background and Application.....	130
Computational Studies of Ligand Promoted Selectivity.....	136
Reaction Scope and Conclusions.....	142
Experimental.....	144
References.....	148
5. QUANTIFICATION OF ACYCLIC DIAMINO CARBENE LIGAND EFFECTS IN A GOLD(I) CATALYZED ISOMERIZATION-CYCLIZATION	152
Introduction.....	152
Development and Analysis of Descriptors for ADC Catalysts.....	155
Conclusion	168
Experimental.....	168
References.....	190

LIST OF TABLES

Tables

2.1. Phosphines in this study. Phosphines 27-38 comprise the “External Set.”	55
2.2. NMR parameters.....	57
2.3. Minimum cone angle conformer parameters	58
2.4. Maximum cone angle parameters	60
2.5. Average steric values	62
2.6. Product ratios for reaction 1.....	64
2.7. Product ratios as a function of ligand to metal ratio	65
2.8. Normalized values	66
2.9. Predicted versus measured values.....	68
2.10: Cyclic voltammetry studies	79
3.1. Phosphine data for [4+3]/[4+2] cycloisomerization	113
3.2. Phosphine data for [2+3]/[2+2] cycloisomerization	113
3.3. Raw data for reaction 5.....	114
3.4. Raw data for reaction 6.....	115
3.5. Calculated energy values	117
3.6. Parameters for eight new phosphines presented in this chapter	120
4.1. Data for Figure 4.3.....	146
4.2. Computational Energy Data.....	146

5.1. Tabulated data for biaryl carboxylic acids.....	185
5.2. Tabulated data for ureas.....	187
5.3. Values for Figure 5.7.....	189

LIST OF FIGURES

Figures

1.1. Henderson Jr. and coworkers identified trends between Taft's σ^* , pK_a , and rate of nucleophilic addition.....	4
1.2. Phosphine electronic parameters.....	6
1.3. Ligand size measurements	8
1.4. Suzuki reaction developed by Wu and Doyle in which differential proximal and remote steric hindrance from the ligand drastically influenced the yield.....	11
1.5. A Nozaki-Hiyama-Kishi allylation reaction was analyzed and the enantioselectivity correlated to the Charton value of the R groups.	13
1.6. Propargylation of acetophenone was shown to be poorly selective with oxazoline peptide ligands	15
1.7. Desymmetrization of biaryl substrates was first described using Sterimol parameters	17
1.8. Multivariate model prediction workflow centered on mechanistically relevant parameters	20
2.1. Giering and coworkers studied the type of ligand binding with phosphines, defining which types were π -acceptors and donors	27
2.2. Parameters from Fey and coworkers utilized seven computed structures	29
2.3. Infrared stretching parameters collected	31
2.4. Suzuki coupling reaction conditions between Aryl group 1 and <i>o</i> TolB(OH) ₂	33
2.5. Interaction/distortion analysis from Schoenebeck and Houk of Pd(PMe ₃) _n oxidative addition to 2.1	36
2.6. Phosphine ligands included in this study	38

2.7. All phosphine ligands tested in this study, as well as measured $\Delta\Delta G^\ddagger$ and predicted $\Delta\Delta G^\ddagger$ in three models presented	39
2.8. Differences in conformer geometry for PEt_3 as well as parameters collected and utilized in this study	40
2.9. Multiple visualization methods revealed complex trends between calculated infrared parameters	43
2.10. Measured and predicted values for all ligands tested	45
2.11. Models identified using the minimum and maximum cone angle conformers.....	46
2.12. Comparative analysis of product ratios versus ligand:metal ratios as well as cyclic voltammetry measurements.	48
2.13. Models developed using the split subsets of ligands	51
2.14. Cyclic voltammogram of $\text{Pd}_2(\text{dba})_3$ and dba	79
3.1. Bonding model developed by Goddard, Toste, and coworkers depicting a linear geometry about the gold atom.....	86
3.2. Two cycloisomerization reactions probed mechanistically	87
3.3. Isotope labeling revealed a significant change in reaction selectivity based on the choice of deuterio- or proteo-substrate 1.	90
3.4. Reaction 1 selectivities correlated to the Au–Cl distance.....	91
3.5. Results from reaction 2 screening and relationship to Au–Cl distance	94
3.6. Reaction 2 selectivities correlated to the average Sterimol L/B_1 , including two extrapolation points	95
3.7. Plausible mechanistic proposals considered	97
3.8. Deuterium labeling and Hammett study results.....	98
3.9. Open and cyclic transition states result in invertive and retentive transmetallation steps respectively	102
3.10. Alkyl-aryl Suzuki reaction developed by Biscoe and coworkers	104
3.11. Reaction 5 ligand selectivity trends	105

3.12. DFT calculated pathways with four ligands	107
3.13. Hammett plot constructed using differentially substituted aryl chlorides	110
3.14. Reaction outcomes from ligand variation using a modified nucleophile and correlation to the ³¹ P NMR shift	111
4.1. General reactivity trends with halogenated pyridines, model reaction and ligand screening outcomes	128
4.2. Parameters for bidentate phosphines	131
4.3. Univariate correlations suggest electronic rather than steric interactions dominate selectivity	133
4.4. Oxidative addition energy profile with four ligands	138
4.5. Distortion-Interaction differences between DMAPF and DTBPF indicating a more strained Pd-aryl species	139
4.6. Transition state structures from the four ligands interrogated	141
4.7. Reaction scope	143
5.1. Diamino carbene ligands utilized by various groups	154
5.2. Tandem [3,3]-sigmatropic rearrangement-[2+2]-cyclization under study and results from an initial screen	156
5.3. Two surrogate molecules were computationally constructed to analyze the appropriate aryl and heterocycle structures	158
5.4. Non-pyridine heterocycles were outliers compared to the pyridines	160
5.5. The nature of the R ¹ atom had a significant effect on enantioselectivity	161
5.6. Crystal structure of complex L23*(AuCl ₂) ₂	163
5.7. Overall multivariate model containing training and validation sets, as well as an external validation	164
5.8. Comparison of reaction enantioselectivity between dichloromethane (DCM) and toluene	166
5.9. Substrate scope of [3,3]-sigmatropic rearrangement-[2+2]-cyclization	167

5.10. Catalysts and the computed surrogate structures	170
5.11. Labels used for biaryl carboxylic acids	185
5.12. Labels used for ureas	187

LIST OF ABBREVIATIONS

Abbreviations

Å	Ångström
°	Degree
°C	Degree Celsius
% V_{bur}	Percent buried volume
1-Ad	1-Adamantyl
$^1J_{\text{P-Se}}$	NMR coupling between phosphorus and selenium one bond apart
^{31}P	Phosphorus-31 NMR
βHE	<i>beta</i> -hydride elimination
ϵ	Solvent dielectric
θ	Tolman cone angle
θ_s	Solid cone angle
μA	Microamperes
ν	Frequency
σ	Hammett parameter
σ^+	Positive charged resonance stabilized Hammett parameter
σ^*	Taft polar parameter
σ_p	para Hammett parameter
χ	Tolman substituent electronic parameter

Ac	Acetyl
ADC	Acyclic diaminocarbene
Ar	Aryl
B ₁	Sterimol minimum radius
B ₅	Sterimol maximum radius
BDE	Bond dissociation energy
BINAM	2,2'-bisamino-1,1'-binaphthyl
Bn	Benzyl
Boc	<i>tert</i> -butyloxycarbonyl
CDCl ₃	Deuteriochloroform
cm ⁻¹	Wavenumbers
cod	cyclooctadiene
<i>c</i> Pent	Cyclopentyl
Cy	Cyclohexyl
dba	Dibenzylideneacetone
DCM	Dichloromethane
DEAPF	1,1'-bis[di-(diethylamino)phosphino]ferrocene
DFT	Density Functional Theory
DIPAPF	1,1'-bis[di-(di- <i>iso</i> -propylamino)phosphino]ferrocene
DMAPF	1,1'-bis[di-(dimethylamino)phosphino]ferrocene
DTBPF	1,1'-bis[di- <i>tert</i> -butyl-phosphino]ferrocene
E(SCF)	Self-consistent field energy
ee	Enantiomeric excess

er	Enantiomeric ratio
es	Enantiomeric specificity
E_{ipa}	Potential at peak anodic current
E_{ox}	Oxidation Potential
equiv	Equivalents
Et	Ethyl
G	Gibbs free energy
G(solv)	Solvation energy
GC	Gas chromatography
h	Hours
HMPA	Hexamethylphosphoramide
HOMO	Highest occupied molecular orbital
Hz	Hertz
i	Current
IR	Infrared
iPr	<i>iso</i> -propyl
kcal	Kilocalorie
kJ	Kilojoule
L	Sterimol length
L_i	Ligand
LL	Bidentate ligand
LFER	Linear free energy relationship
LUMO	Lowest unoccupied molecular orbital

M	Metal
<i>m</i>	Meta
Me	Methyl
mg	Milligram
mL	Milliliter
mmol	Millimole
mol	Mole
<i>m</i> -Tol	Meta-tolyl
N/D	Not determined
N ₂	Nitrogen
NBO	Natural bond orbital
<i>n</i> Bu	<i>n</i> -butyl
neop	<i>neo</i> -pentyl
NHK	Nozaki-Hiyama-Kishi
NMR	Nuclear Magnetic Resonance
<i>n</i> Pr	<i>n</i> -propyl
<i>o</i>	ortho
<i>o</i> -Tol	ortho-tolyl
<i>p</i>	para
p <i>K</i> _a	Negative log ₁₀ of acid dissociation constant
Ph	Phenyl
ppm	Parts per million
PR ₃	Tertiary phosphine bearing three substituents

prod	Product
<i>p</i> -Tol	para-tolyl
QALE	Quantitative analysis of ligand effects
Quant	Quantitative
QSAR	Quantitative structure-activity relationships
R	Substituent
R ²	Correlation coefficient
RE	Reductive elimination
rt	Room temperature
S	Entropy
SCE	Standard Calomel Electrode
SCRF	Self-consistent reaction field
<i>t</i> Bu	<i>tert</i> -butyl
TEA	Triethylamine
TEP	Tolman Electronic Parameter
THF	Tetrahydrofuran
Trt	Trityl
Ts	Tosyl
TS	Transition state
TMSCl	Trimethylsilylchloride
Tol	Tolyl
V	Volts
ZPE	Zero point energy

ACKNOWLEDGEMENTS

Four-plus years have flown by, and a lot of science has been done. Amazingly, this dissertation is only a partial accounting of that work, and I most certainly would not have completed it all without the help and support of others. I don't think that I can remember everyone that has helped along the way, so only a few people are mentioned here by name. I hope all that read this know they have helped me.

To my family: I love you dearly for all that you have done. You all have kept me grounded throughout the trials of grad school. Your unconditional support cannot be appreciated enough.

To my teachers: you got me excited about science when I was young. You sparked my interest in organic chemistry. You helped me grow into a functional scientist. Thank you for everything.

To my advisor Matt: thank you for all you have taught. There have been times when I hated working with you and times when I loved working with you. I interpret that as a pretty good outcome.

To my committee: thank you for demanding the best out of me. By setting high expectations you have forced me to work harder and to raise my game.

To my collaborators: you were the ones to perform the synthetic chemistry. My work would mean nothing without your efforts and I am deeply indebted to you all.

To the Sigman group, alumni, current, and future: thank you for teaching me.

Thank you for being highly committed to doing good science. Thank you for inspiration.

Thank you for editing my writing. Thank you for all of this and so much more.

To my classmates, labmates, and friends: thanks for teaching me, hanging out with me, and generally being around. You've made a grueling time period lots of fun.

CHAPTER 1

INTRODUCTION

An enduring goal of synthetic chemists is the discovery of a reaction that yields a single desired product with perfect selectivity when multiple products are possible. Such an idealized reaction would require precise regulation of all reactants, catalysts, and additives, enabling the controlled trajectory of a single reaction pathway. Chemists have persevered in this endeavor by iteratively augmenting reaction conditions to access synthetically useful transformations. However, chemists' best intuitive knowledge can still be stymied by confounding reactions controlled by multiple influences, the results of which are poorly selective reactions.

Within organometallic chemistry, a key technique for interrogating reaction conditions involves the variation of donor ligands to identify optimal steric and electronic properties that lead to the desired reaction outcome. If adequate selectivity cannot be achieved via intuitive ligand evaluation, in-depth mechanistic examination often becomes the chemists' best tool for identifying principal considerations that can be systematically modified to yield an optimal result. One such method involves the development of linear free energy relationships (LFERs) that can provide nonintuitive extrapolations from the lower performing structures. In essence, an LFER produces a quantitative relationship between the results and known descriptors that can be used to predict a more optimal

ligand. Therefore, the ability to identify a LFER is highly beneficial for moving from low to high selectivity.

Construction of a ligand effect LFER requires three components. First, quantitative results must be obtained where the ligand is varied; this can include, but is not limited to, site-, chemo-, and stereo-selective outcomes, as well as rates or equilibria. Second, an intrinsic property of the compounds must each be quantitatively measured. Finally, the results and properties are related via mathematical equations. Importantly, by selecting mechanistically relevant descriptors, the LFER can yield clues about the reaction manifold. The prototypical example of a LFER is a Hammett plot that relates substrate acidity to reaction outcomes;¹ these correlations have been interpreted as indicating the change in charge density within the rate/selectivity determining step, and thus, are a quantification of the substrate electronic properties.² Within ligand variations, basicity³ and nucleophilicity⁴ have classically been considered, as well as size descriptors.⁵ Each of these measures relate fundamental ligand properties to how the ligand affects the energetics of the transition state. Thus, an LFER can simultaneously be used to probe a reaction mechanism through descriptor analysis and to enhance the desired reactivity via prediction.

My work has focused on kinetically controlled reactions; therefore, we have assumed Curtin-Hammett control so that the reaction outcomes can be related to the ligand parameters. In other words, our hypothesis is that the measured product ratios are solely a consequence of ligand variations affecting the energy differences between the transition states (TSs) leading to the observed products. Thus, ground state equilibria have generally been ignored. However, we expect that properties measured from ground

state molecules will similarly be present in the respective transition states due to the similarities of the chemical structure. Doing so drastically simplifies the collection of parameters as transition state calculations are computationally more expensive. These two fundamental assumptions have been guiding principles for my graduate work.

As much of my dissertation research has been focused on phosphine ligands, this chapter includes a discussion of the historical examples of parameters for this ligand class. Additionally, classic and modern approaches to LFERs and their integration into comprehensive mechanistic analysis are presented in the second section. Overall, the goal of this chapter is to introduce how ligand effects can be systematically interrogated and quantified.

Phosphine Descriptors

Phosphine ligands are ubiquitous in organometallic chemistry due to their high tunability and binding affinity. As phosphine performance is affected by steric and electronic considerations, parameters developed to describe these features will be discussed in the following paragraphs.

Electronic Parameters

Among the oldest phosphine parameters are electronic descriptors focused on their nucleophilicity^{4a} and basicity.³ For example, Henderson Jr. and coworkers correlated the pK_a values of 17 phosphines to the sum of Taft's σ^* parameters⁶ for substituents connected to the phosphorus atom (R of PR_3 , Figure 1.1).⁷ A linear relationship was identified between these measures. Interestingly, the slope of this

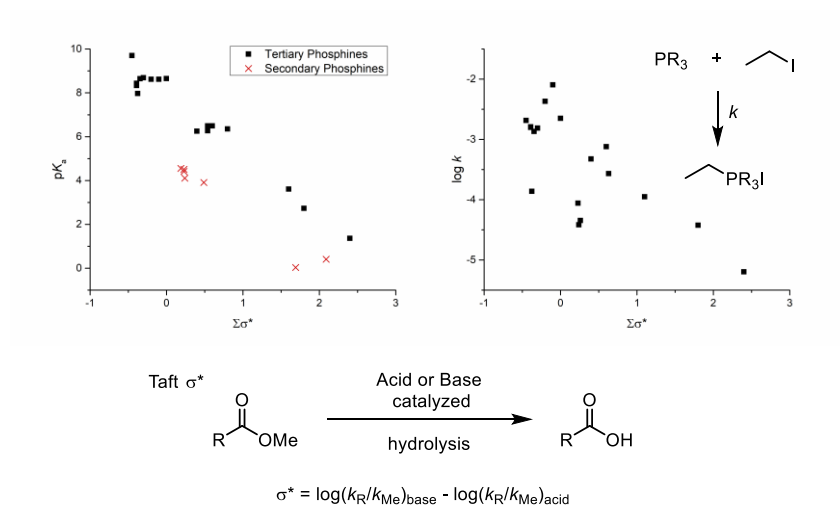
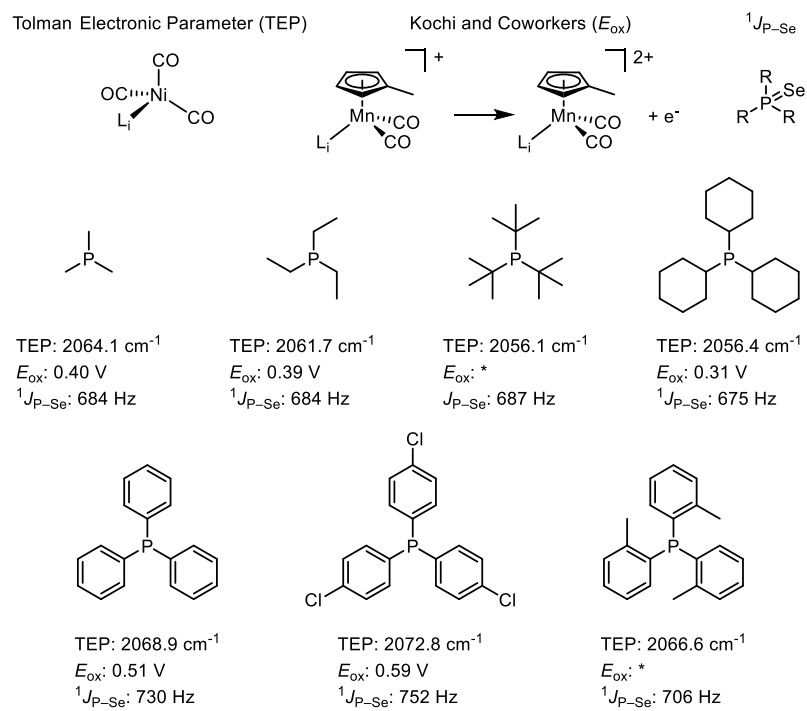


Figure 1.1. Henderson Jr. and coworkers identified trends between Taft's σ^* , pK_a , and rate of nucleophilic addition.

relationship was found to be constant between secondary and tertiary phosphines, indicating that substitution from hydrogen to carbon resulted in a consistent change of pK_a . Using the same sum of Taft's parameters, the group compared the relative tertiary phosphine nucleophilicity. A linear relationship was found between this parameter and the rate of reaction of the phosphines with ethyl iodide, though significant outliers were noted. Methyl substitution comprised one class of deviation, wherein the reaction rate was faster than expected. Complex steric and electronic effects were hypothesized to be the origin of this discrepancy suggesting that nucleophilicity is likely a combination of interactions that would be difficult to delineate.

The desire to develop a pure electronic parameter resulted in the development of the Tolman electronic parameter. Building on work from Strohmeier and Müller,⁸ Tolman interrogated 70 P-donor ligands (phosphine and nonphosphine, L_i) in $Ni(CO)_3L_i$ complexes, recognizing that the $C\equiv O$ infrared stretching frequency was sensitive to the bound ligand (Figure 1.2). For example, tri-*tert*-butyl phosphine ($PtBu_3$), a commonly utilized large, strongly donating ligand, resulted in a symmetric $C\equiv O$ stretching frequency of 2056.1 cm^{-1} whereas triphenyl phosphine (PPh_3) resulted in a frequency of 2068.9 cm^{-1} . This result was attributed to PPh_3 being significantly less electron donating, as the small size of the CO ligands would minimize steric interactions with the fourth ligand. Additionally, Tolman identified that the phosphine substituent effects are summative. Hence, each substituent (R of PR_3) was assigned a value (χ) that could be added to 2056.1 to predict with reasonable accuracy the $C\equiv O$ stretching frequency from $Ni(CO)_3L_i$. Overall, Tolman reasoned that these changes are results of the ligand donor-acceptor properties, and not purely an effect of the donation from phosphorus.



*not published

Figure 1.2. Phosphine electronic parameters.

Numerous parameters were similarly defined as alternatives to the carbonyl stretching frequency (Figure 1.2). Devised by Kochi and coworkers,⁹ the one electron oxidation potential of $\text{MeCpMn(CO)}_2\text{L}_i$ complexes were measured versus the standard calomel electrode in dichloromethane. This parameter was shown to correlate to both the $\text{C}\equiv\text{O}$ stretching frequency¹⁰ and the $\text{p}K_a$ of the protonated phosphine.¹¹ Other electronic descriptors have been derived by Giering,^{10, 12} Koga,¹³ and Cremer.¹⁴ NMR parameters have similarly been measured by multiple groups,¹⁵ including the ^{31}P shift and $^1J_{\text{P-Se}}$ coupling from the phosphine selenide. Specifically, the $^1J_{\text{P-Se}}$ coupling varies based on the electron-withdrawing or donating substituents, wherein more electron-poor phosphines result in larger $^1J_{\text{P-Se}}$. McFarlane and Rycroft argue that this outcome is due to less electron sharing between the phosphorus and selenium atoms, and thus increased σ -character (decreased π -character) of the bond. However, further examination of these outcomes using modern techniques is warranted. In sum, extensive parameter sets to describe electronic perturbations of phosphine ligands are available.

Steric Parameters

Concurrent work from Tolman in 1970 defined a steric parameter.⁵ Using rudimentary tools that consisted of molecular model kits and a protractor, Tolman quantified the footprint of 24 P-donor ligands by defining a cone angle as “the apex angle of a minimum cone, centered 2.28 Å away from the center of the P atom, which just touches the outermost extremities of a ligand folded back while maintaining C_3 symmetry” (Figure 1.3). The distance chosen (2.28 Å) was proposed to approximate the average distance between the centers of the phosphorus and nickel atoms in a crystal

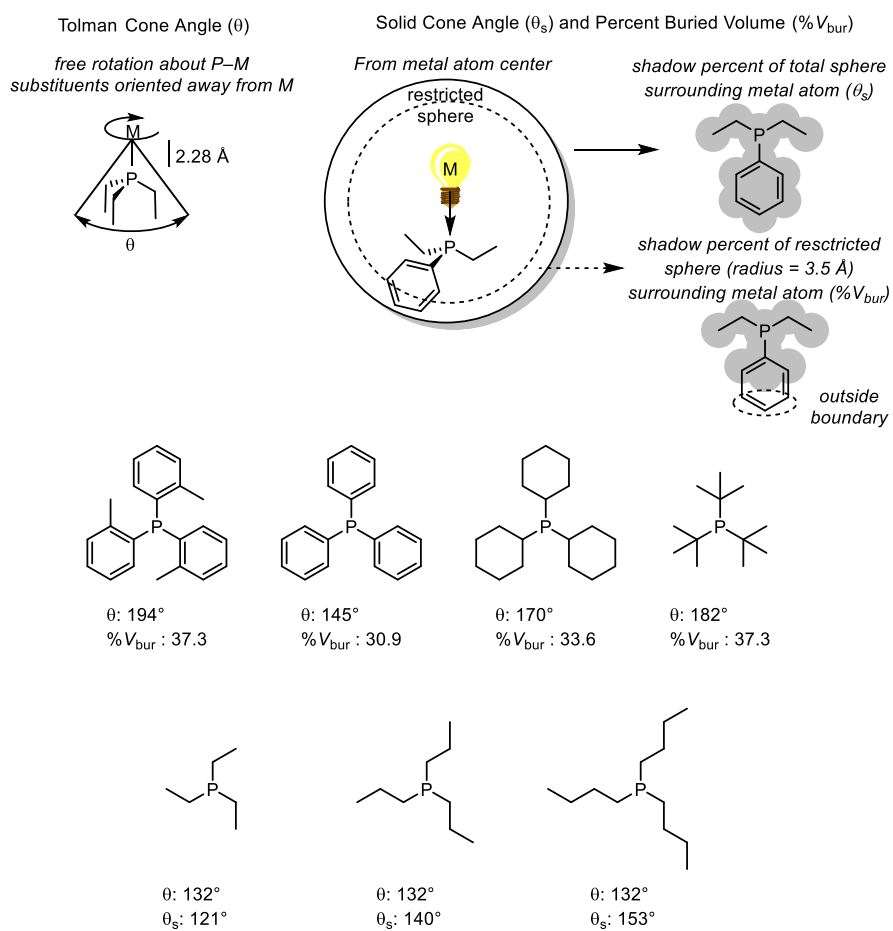


Figure 1.3. Ligand size measurements.

lattice. These angles were found to correlate to the ligand exchange equilibria of nickel complexes whereas the $\text{C}\equiv\text{O}$ stretching frequencies did not, highlighting the overwhelming influence of steric interactions. Importantly, the Tolman cone angles were found to be widely applicable to describing many reaction outcomes; Halpern and Phelan¹⁶ reported in 1972 that the substitution rate of benzyl bromide by cobalt complexes directly correlated to the size of the phosphine. Further uses were reviewed by Tolman in 1977,¹⁷ highlighting the extensive utility of the cone angle as well as the electronic parameter. These two descriptors have become common measures to correlate phosphine ligand effects.

Despite the ubiquity of the Tolman cone angle, this measurement has received substantial criticism for an inability to accurately describe more nuanced steric effects. The most common critique of the cone angle measurement has been that the conformation is high in energy, a problem recognized by Tolman.¹⁷ Therefore, some phosphines are functionally larger than originally measured. For example, tri-*n*-butyl phosphine ($\text{P}n\text{Bu}_3$), tri-*n*-propyl phosphine ($\text{P}n\text{Pr}_3$), and tri-ethyl phosphine (PEt_3) each have the same cone angle, an intuitively surprising result. In response to these criticisms, alternative parameters have been developed since 1970 that provide insight into the relevant steric considerations.

One modern method to quantify the size of phosphine ligands originated at nearly the same time as the Tolman cone angle.¹⁸ Immirzi and Musco introduced the “solid angle” to more accurately describe ligand sizes by measuring the “angular encumbrance” of metal-ligand crystal structures.¹⁸ Further refinement by Komatsuzaki et. al.¹⁹ and White and coworkers²⁰ defined the mathematical equations necessary to generalize the

measurement. Using a projection of a molecule onto the inside of a sphere, the measurement of the area of the resultant “shadow” was defined as the solid angle, and reported either as a percentage of the total sphere or the angle of a cone that would cover the equivalent percentage.

Building upon the idea of a solid cone, Nolan and coworkers hypothesized that proximal steric bulk would have a greater influence on reactivity. Therefore, atoms outside of a certain distance (initially 3.0 Å, most often 3.5 Å) were excluded in the “percent buried volume” ($\%V_{\text{bur}}$).²¹ Spurred by the relative ease of measurement using computational or crystal structures, this measure has become nearly as prevalent in organometallics as the cone angle. For example, Wu and Doyle recently utilized $\%V_{\text{Bur}}$ to interrogate the ligand effects of a nickel catalyzed Suzuki coupling (Figure 1.4). In this instance, the Tolman cone angle was insufficient at describing the reaction yield as large ligands resulted in highly variable outcomes. However, by considering the difference between the ligand cone angle and $\%V_{\text{Bur}}$, a modest trend can be identified. Thus, the remote steric hindrance has an outsized influence on the reaction yield. This trend can be further improved by additionally considering the electronic ligand effects in a multivariate analysis, the topic of the following section.

Multivariate Analysis

For nearly ten years, the Sigman group has been focused on developing quantitative methods to relate reaction outcomes to multiple parameters or descriptors, enabling several effects to be investigated simultaneously rather than separately. Through the use of statistical techniques more commonly used in quantitative structure-activity

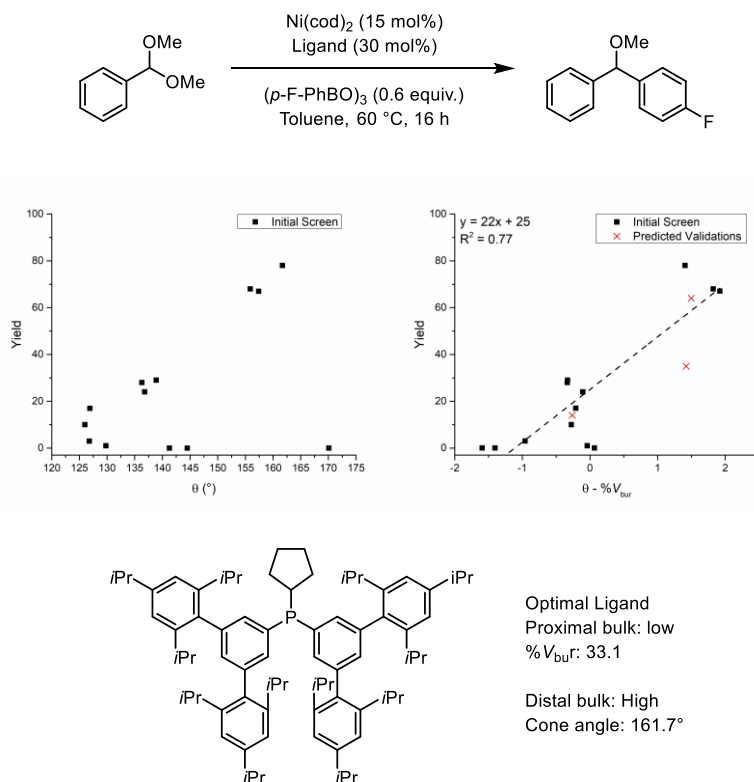


Figure 1.4. Suzuki reaction developed by Wu and Doyle in which differential proximal and remote steric hindrance from the ligand drastically influenced the yield.

relationships (QSAR),²² correlations between structural descriptors and reaction outputs have been developed. By combining classic and novel physical organic descriptors and integrating them into multivariate relationships with the desired reaction outcomes, the relative importance of individual effects can be quantified.²³ This approach has provided access to the simultaneous interrogation of steric and electronic interactions,²⁴ electrostatic interactions,²⁵ and phase transfer reactions.²⁶ Each of these is a classically difficult challenge, and adequate answers have only been identified recently using this method. The following section focuses on the evolution of two projects that constituted major contributions to the overall program goals of uniting reaction optimization with mechanistic interrogation. Finally, the techniques necessary for building a multivariate correlation are discussed.

Multidimensional Modeling

The catalytic asymmetric addition of allyl fragments to ketones is a useful method for the synthesis of enantio-enriched homoallylic alcohols, and the development of conditions for a Nozaki-Hiyama-Kishi (NHK) allylation of ketone derivatives was underway in the Sigman group in 2007 (Figure 1.5).²⁷ Promising initial results had been noted for addition to acetophenone using conditions optimized for the allylation of benzaldehyde using oxazoline peptide ligands.²⁸ The carbamate protecting group structure was modulated and LFERs were used to guide optimization.²⁹ Specifically, Taft/Charton steric parameters, derived from the relative rate of acid catalyzed hydrolysis of the appropriate methyl ester,³⁰ were used to quantify the size of the carbamate substituent. Unfortunately, two correlations were observed: first, for five alkyl groups

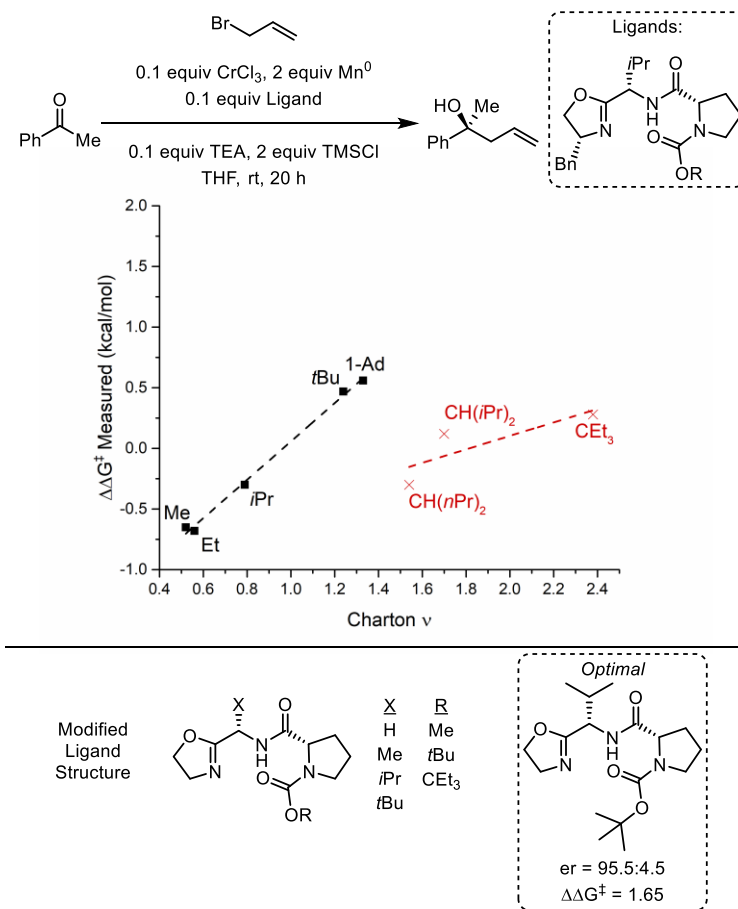


Figure 1.5. A Nozaki-Hiyama-Kishi allylation reaction was analyzed and the enantioselectivity correlated to the Charton value of the R groups.

varying in size between methyl and 1-adamantyl, a slope of 1.51 was identified, indicating a strong steric interaction. When utilizing larger alkyl carbamate substituents (Charton value >1.5), the enantioselectivity was distinctly lower than would be expected according to the first relationship. Thus, the second correlation included these three larger substituents. To account for this outcome, the Sigman group hypothesized that two distinct scenarios could be occurring. First, the mechanism could be changing due to the very large substituents, causing a break from the trend, similar to the common interpretation of a break in a Hammett plot.^{2, 31} Second, the Charton parameters may not accurately reflect the carbamate size.²³ These possibilities were investigated in follow-up work.

To probe the origin of the break in the LFER, a ligand library containing systematic changes to both the backbone and the carbamate group was synthesized and tested (Figure 1.5).³² The resultant enantioselectivity outcomes were then correlated with a multivariate regression using Charton descriptors for each of the two diversification points. Importantly, analysis of changes to solely the backbone or the carbamate did not lead to identification of the ligand that results in the highest enantioselectivity. Instead, the interactions of the two variable structures had to be considered to identify the optimal ligand. The nonadditive combination of such variables highlighted an important conclusion from this project: synergistic interactions can simultaneously be accounted for using this methodology.

Having established that multiple effects could concurrently be modeled, the group endeavored to interrogate a related propargylation of acetophenone that had not yielded a satisfactory result through typical ligand screening (Figure 1.6).³³ Testing and analysis

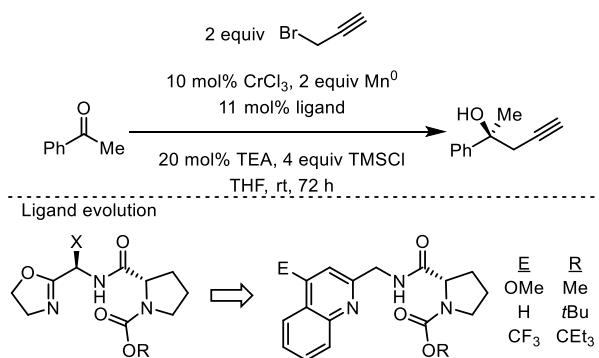


Figure 1.6. Propargylation of acetophenone was shown to be poorly selective with oxazoline peptide ligands. Driven by molecular modeling, the group moved to quinoline peptide derivatives and modeled electronic and steric effects simultaneously.

using multivariate regression of the same ligand library revealed a shallow energy surface in which the best predicted ligand would only produce 50% enantiomeric excess (ee).³³ Thus, different ligand structures were necessary to reach sufficient selectivity, forcing a consideration of quinoline-proline ligands that permit electronic changes about the quinoline. This shift enabled synchronous evaluation of electronic and steric changes to the ligand. Three quinoline variations were tested with the substitutions being quantified with the Hammett parameter.^{1a} Charton parameters were again used to quantify the size of the carbamate protecting group. Fortunately, the identified regression correctly identified that a 4-OMe substituent in combination with a tert-butyl carbamate protecting group would be the best performing ligand. Thus, the ability to evaluate synergistic steric and electronic trends was confirmed.

Selecting Parameters

Returning to the “break” in the Charton plot in the previous section, the group reconsidered how the descriptor was measured and how this related to the proposed mechanism. The Charton parameter was derived from a specific mechanism, the hydrolysis of methyl esters, which assumes free rotation about the substituent-ester C–C bond. Thus, generalization to other mechanistic manifolds is likely unreasonable. The lack of the ability to describe reaction outcomes was again apparent when the group analyzed a desymmetrization of bisphenols catalyzed by a peptide catalyst as reported by the Miller group (Figure 1.7).³⁴ In this instance, attempts to correlate variations of the R group of the substrate to the Charton parameters were unsuccessful. As an example, -CH₂*t*Bu and -1-adamantyl have similar measured Charton values (1.34 versus 1.33), and

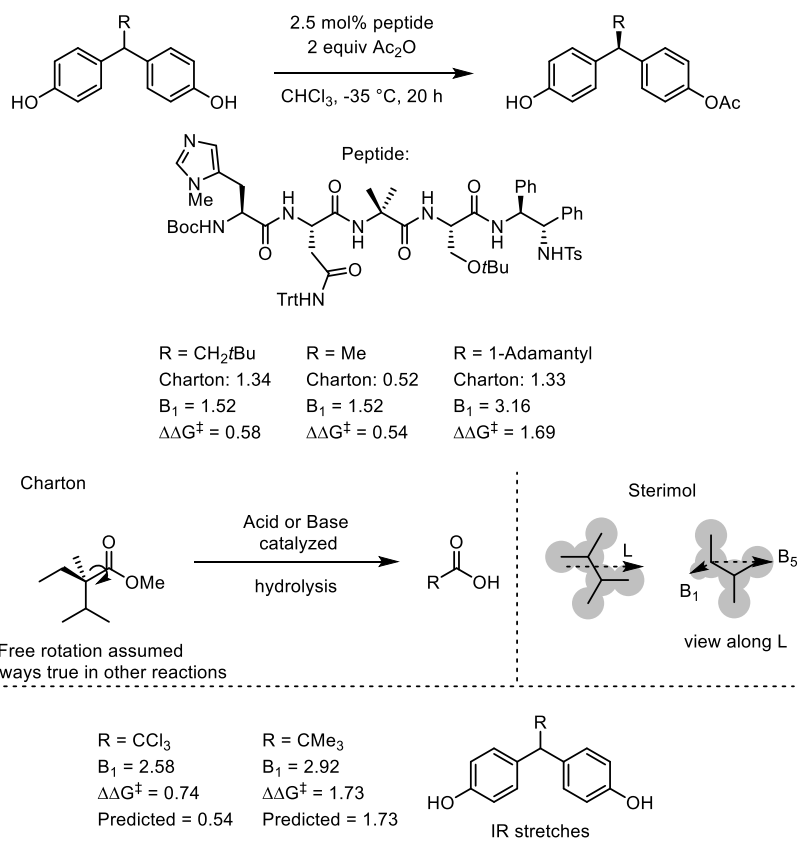


Figure 1.7. Desymmetrization of biaryl substrates was first described using Sterimol parameters. Refinement of this model using IR stretches allowed for stereo-electronic effects to be predicted simultaneously.

thus would be predicted to react accordingly. However, the substrate including $-\text{CH}_2t\text{Bu}$ yielded an enantioselectivity much more similar to the $-\text{Me}$ containing substrate. In order to account for this effect, Sterimol parameters were explored. This measures the three dimensional substituent footprint by first measuring the length (L) of the group along the desired bond. Orthogonal to L is the minimum (B_1) and maximum (B_5) radius. Thus, these measurements can account for nonsymmetric substituents, and in the desymmetrization reaction, a linear relationship was identified with B_1 . Importantly, this trend accounts for many of the previous outliers, including $-\text{CH}_2t\text{Bu}$ which has the same B_1 value as Me (1.52).

Further work with this same system noted that differential electronic substituents remained outliers and were not accurately described by the simple steric model. For example, a $-\text{CCl}_3$ group according to Sterimol B_1 is comparable in size as a $t\text{Bu}$ ($-\text{CMe}_3$) group ($B_1 = 2.58$ vs 2.92). Therefore, the substrates containing these groups should have reacted in the same manner if only steric interactions influenced the selectivity. This was not the case, as $-\text{CCl}_3$ resulted in a significantly lower enantioselectivity. Again, the development of new parameters was necessary to accurately describe the reaction outcomes. In order to account for stereo-electronic effects, the Sigman group utilized calculated infrared (IR) frequencies. Using three stretches of the biaryl substrates, the group was able to predict the enantioselectivities of ten substrates including five that did not fit the steric only model. Furthermore, the Sigman group demonstrated that the use of IR frequencies could generally be applied to correlate selectivity outcomes by analyzing two other reactions. In summary, the Sigman group has developed novel parameters to correlate reaction outcomes.

Model Development

Having demonstrated that multifaceted effects can simultaneously be correlated, the Sigman group has returned to studying reaction mechanisms and has sought to apply the multivariate analysis to understanding underlying mechanistic phenomena. This challenge has required that an iterative workflow²³ be applied based on classic multivariate modeling approaches (Figure 1.8).³⁵

First, preliminary data are collected that encompasses a desired outcome to be improved, designated as a training set. Concurrently, parameters are collected including known descriptors, such as those described above or elsewhere, as well as designer parameters specific to the question at hand. In general, the parameter selection is dictated by an initial mechanistic hypothesis. For example, stereo-electronic effects were likely present in the desymmetrization reaction displayed previously (Figure 1.7). Therefore, parameters influenced by stereo-electronic factors were simulated and identified, eventually resulting in the use of IR measures. Generally, we have preferred that these descriptors be computationally based, as computed parameters are significantly easier to collect than experimental and can facilitate future virtual screens. To facilitate comparisons across parameter sets, the values are normalized by subtracting the mean and dividing by the standard deviation. This results in all parameter sets having uniform value distributions, a crucial step for multivariate model identification.

Following the collection of both reaction outcomes and parameters, correlations between data sets are searched for. Mathematical models are identified using a mixture of statistical techniques (such as stepwise linear regression) and manual substitutions. The outcomes from this step dictate whether to move forward or to return to the previous step.

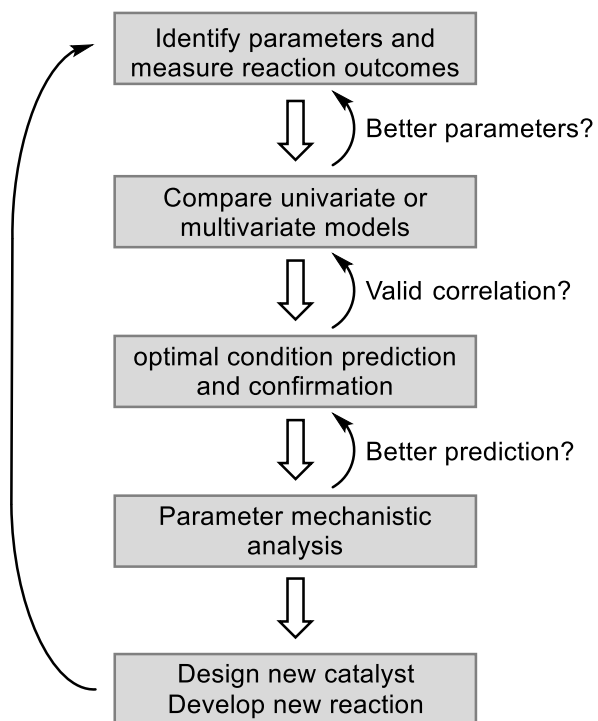


Figure 1.8. Multivariate model prediction workflow centered on mechanistically relevant parameters.

For instance, the lack of predictive models may indicate that the parameters are inadequate for describing the process. Therefore, other descriptors may be needed, similar to the progression of correlations within the desymmetrization reaction (Figure 1.7). If, however, a promising trend is found, the validity of the optimal model is tested through prediction and evaluation of synthetically reasonable catalysts or substrates (validation set).

Following the successful prediction of external reagent structures, the parameters used to build the equation are related back to mechanistic hypotheses of steric and electronic effects. Analysis of these descriptors is used to inform ideas of the reaction sequence, building a holistic picture of how reactants interact. This process may reveal nonintuitive outcomes that can be further exploited in novel reactivity.

Conclusions

Having multivariate tools and parameter sets readily available, we have turned our attention to mechanistic interrogation. Can the parameters used in a model teach us about the role ligands play in influencing reaction pathways? Furthermore, can this tool be used within a larger context to build a more nuanced mechanistic picture? These two questions served as beacons during my graduate work. Linear free energy relationships are staples within mechanistic investigations and most of my time has focused on identifying and interpreting uni- and multivariate free energy relationships, to provide actionable hypotheses. These projects have interrogated numerous parameters that have evaluated specific electronic interactions, hydrogen bonding effects, and attractive π interactions. Through this work, our group has become proficient at collecting and analyzing

parameter sets and applying these to mathematical modeling of reaction outcomes keyed toward mechanistic interrogation.

References

1. (a) Hammett, L. P., Some Relations between Reaction Rates and Equilibrium Constants. *Chem. Rev.* **1935**, *17* (1), 125-136; (b) Hammett, L. P., The Effect of Structure upon the Reactions of Organic Compounds. Benzene Derivatives. *J. Am. Chem. Soc.* **1937**, *59* (1), 96-103.
2. Anslyn, E. V.; Dougherty, D. A., *Modern Physical Organic Chemistry*. University Science: Sausalito, CA, 2006.
3. Henderson, W. A.; Streuli, C. A., The Basicity of Phosphines. *J. Am. Chem. Soc.* **1960**, *82* (22), 5791-5794.
4. (a) Henderson, W. A.; Buckler, S. A., The Nucleophilicity of Phosphines. *J. Am. Chem. Soc.* **1960**, *82* (22), 5794-5800; (b) Kempf, B.; Mayr, H., Rates and Equilibria of the Reactions of Tertiary Phosphanes and Phosphites with Benzhydrylium Ions. *Chemistry – A European Journal* **2005**, *11* (3), 917-927; (c) Follet, E.; Mayer, P.; Stephenson, D. S.; Ofial, A. R.; Berionni, G., Reactivity-Tuning in Frustrated Lewis Pairs: Nucleophilicity and Lewis Basicity of Sterically Hindered Phosphines. *Chemistry - A European Journal* **2017**, *23* (31), 7422-7427; (d) Maji, B.; Breugst, M.; Mayr, H., N-Heterocyclic Carbenes: Organocatalysts with Moderate Nucleophilicity but Extraordinarily High Lewis Basicity. *Angew. Chem. Int. Ed.* **2011**, *50* (30), 6915-6919.
5. Tolman, C. A., Phosphorus Ligand Exchange Equilibria on Zerovalent Nickel. Dominant Role for Steric Effects. *J. Am. Chem. Soc.* **1970**, *92* (10), 2956-2965.
6. Taft, R. W., Linear Steric Energy Relationships. *J. Am. Chem. Soc.* **1953**, *75* (18), 4538-4539.
7. Streuli, C. A., Determination of Basicity of Substituted Phosphines by Nonaqueous Titrimetry. *Anal. Chem.* **1960**, *32* (8), 985-987.
8. Strohmeier, W.; Müller, F.-J., Klassifizierung Phosphorhaltiger Liganden in Metallcarbonyl-Derivaten nach der π -Acceptorstärke. *Chem. Ber.* **1967**, *100* (9), 2812-2821.
9. Hershberger, J. W.; Klingler, R. J.; Kochi, J. K., Kinetics, Thermodynamics, and Mechanism of the Radical-Chain Process for Ligand Substitution of Metal Carbonyls. *J. Am. Chem. Soc.* **1983**, *105* (1), 61-73.

10. Golovin, M. N.; Rahman, M. M.; Belmonte, J. E.; Giering, W. P., Quantitative Separation of σ - and π -Components of Transition Metal-Phosphorus Bonding and the Application of Ligand Effects in Organometallic Chemistry. *Organometallics* **1985**, *4* (11), 1981-1991.
11. Zizelman, P. M.; Amatore, C.; Kochi, J. K., Steric and Electronic Effects in Ligand Substitution of Metal Carbonyls. Rapid Kinetics of Labile Carbonylmanganese Complexes by Transient Electrochemical Techniques. *J. Am. Chem. Soc.* **1984**, *106* (13), 3771-3784.
12. Rahman, M. M.; Liu, H. Y.; Prock, A.; Giering, W. P., Quantitative Analysis of Ligand Effects. 2. Steric and Electronic Factors Influencing Transition-Metal-Phosphorus(III) Bonding. *Organometallics* **1987**, *6* (3), 650-658.
13. Suresh, C. H.; Koga, N., Quantifying the Electronic Effect of Substituted Phosphine Ligands via Molecular Electrostatic Potential. *Inorg. Chem.* **2002**, *41* (6), 1573-1578.
14. Setiawan, D.; Kalescky, R.; Kraka, E.; Cremer, D., Direct Measure of Metal–Ligand Bonding Replacing the Tolman Electronic Parameter. *Inorg. Chem.* **2016**, *55* (5), 2332-2344.
15. (a) McFarlane, W.; Rycroft, D. S., Studies of Organophosphorus Selenides by Heteronuclear Magnetic Triple Resonance. *J. Chem. Soc., Dalton Trans.* **1973**, (20), 2162-2166; (b) Pinnell, R. P.; Megerle, C. A.; Manatt, S. L.; Kroon, P. A., Nuclear Magnetic Resonance of Phosphorus Compounds. VII. Evidence for Steric Effects on the ^{31}P - ^{77}Se Coupling and ^{31}P chemical Shifts. *J. Am. Chem. Soc.* **1973**, *95* (3), 977-978; (c) Allen, D. W.; Taylor, B. F., The Chemistry of Heteroarylphosphorus Compounds. Part 15. Phosphorus-31 Nuclear Magnetic Resonance Studies of the Donor Properties of Heteroarylphosphines Towards Selenium and Platinum(II). *J. Chem. Soc., Dalton Trans.* **1982**, (1), 51-54; (d) Allen, D. W.; Nowell, I. W.; Taylor, B. F., The Chemistry of Heteroarylphosphorus Compounds. Part 16. Unusual Substituent Effects on Selenium-77 Nuclear Magnetic Resonance Chemical Shifts of Heteroaryl- and Aryl-Phosphine Selenides. X-Ray Crystal Structure of Tri(2-furyl)phosphine Selenide. *J. Chem. Soc., Dalton Trans.* **1985**, (12), 2505-2508; (e) Tebby, J. C., *CRC Handbook of Phosphorus-31 Nuclear Magnetic Resonance Data*. CRC Press: Boca Raton, 1991.
16. Halpern, J.; Phelan, P. F., Reactions of Bis(dioximato)cobalt(II) Complexes with Organic Halides. Influence of Electronic and Steric Factors upon Re-activity. *J. Am. Chem. Soc.* **1972**, *94* (6), 1881-1886.
17. Tolman, C. A., Steric Effects of Phosphorus Ligands in Organometallic Chemistry and Homogeneous Catalysis. *Chem. Rev.* **1977**, *77* (3), 313-348.
18. Immirzi, A.; Musco, A., A Method to Measure the Size of Phosphorus Ligands in Coordination Complexes. *Inorg. Chim. Acta* **1977**, *25*, L41-L42.

19. Komatsuzaki, T.; Sakakibara, K.; Hirota, M., A New Method for Evaluating the Steric Hindrance by Substituent. *Tetrahedron Lett.* **1989**, *30* (25), 3309-3312.
20. (a) White, D.; Taverner, B. C.; Leach, P. G. L.; Coville, N. J., Quantification of Substituent and Ligand Size by the Use of Solid Angles. *J. Comput. Chem.* **1993**, *14* (9), 1042-1049; (b) White, D. P.; Anthony, J. C.; Oyefeso, A. O., Computational Measurement of Steric Effects: the Size of Organic Substituents Computed by Ligand Repulsive Energies. *J. Org. Chem.* **1999**, *64* (21), 7707-7716.
21. Hillier, A. C.; Sommer, W. J.; Yong, B. S.; Petersen, J. L.; Cavallo, L.; Nolan, S. P., A Combined Experimental and Theoretical Study Examining the Binding of N-Heterocyclic Carbenes (NHC) to the Cp**RuCl* (Cp* = η^5 -C₅Me₅) Moiety: Insight into Stereoelectronic Differences between Unsaturated and Saturated NHC Ligands. *Organometallics* **2003**, *22* (21), 4322-4326.
22. Hansch, C. L., Albert, *Exploring QSAR: Fundamentals and Applications in Chemistry and Biology*. American Chemical Society: Washington, DC, 1995.
23. Sigman, M. S.; Harper, K. C.; Bess, E. N.; Milo, A., The Development of Multidimensional Analysis Tools for Asymmetric Catalysis and Beyond. *Acc. Chem. Res.* **2016**, *49* (6), 1292-1301.
24. Santiago, C. B.; Milo, A.; Sigman, M. S., Developing a Modern Approach To Account for Steric Effects in Hammett-Type Correlations. *J. Am. Chem. Soc.* **2016**, *138* (40), 13424-13430.
25. (a) Neel, A. J.; Hilton, M. J.; Sigman, M. S.; Toste, F. D., Exploiting Non-Covalent π Interactions for Catalyst Design. *Nature* **2017**, *543* (7647), 637-646; (b) Orlandi, M.; Coelho, J. A. S.; Hilton, M. J.; Toste, F. D.; Sigman, M. S., Parametrization of Non-covalent Interactions for Transition State Interrogation Applied to Asymmetric Catalysis. *J. Am. Chem. Soc.* **2017**, *139* (20), 6803-6806.
26. Milo, A.; Neel, A. J.; Toste, F. D.; Sigman, M. S., A Data-Intensive Approach to Mechanistic Elucidation Applied to Chiral Anion Catalysis. *Science* **2015**, *347* (6223), 737-743.
27. Miller, J. J.; Sigman, M. S., Design and Synthesis of Modular Oxazoline Ligands for the Enantioselective Chromium-Catalyzed Addition of Allyl Bromide to Ketones. *J. Am. Chem. Soc.* **2007**, *129* (10), 2752-2753.
28. Lee, J.-Y.; Miller, J. J.; Hamilton, S. S.; Sigman, M. S., Stereochemical Diversity in Chiral Ligand Design: Discovery and Optimization of Catalysts for the Enantioselective Addition of Allylic Halides to Aldehydes. *Org. Lett.* **2005**, *7* (9), 1837-1839.

29. (a) Sigman, M. S.; Jensen, D. R., Ligand-Modulated Palladium-Catalyzed Aerobic Alcohol Oxidations. *Acc. Chem. Res.* **2006**, *39* (3), 221-229; (b) Jensen, K. H.; Sigman, M. S., Systematically Probing the Effect of Catalyst Acidity in a Hydrogen-Bond-Catalyzed Enantioselective Reaction. *Angew. Chem. Int. Ed.* **2007**, *46* (25), 4748-4750.
30. Charton, M., Steric effects. I. Esterification and Acid-Catalyzed Hydrolysis of Esters. *J. Am. Chem. Soc.* **1975**, *97* (6), 1552-1556.
31. (a) Schreck, J. O., Nonlinear Hammett relationships. *J. Chem. Educ.* **1971**, *48* (2), 103; (b) Jaffé, H. H., A Reëxamination of the Hammett Equation. *Chem. Rev.* **1953**, *53* (2), 191-261; (c) Richard, J. P.; Jencks, W. P., A Simple Relationship Between Carbocation Lifetime and Reactivity-Selectivity Relationships for the Solvolysis of Ring-Substituted 1-Phenylethyl Derivatives. *J. Am. Chem. Soc.* **1982**, *104* (17), 4689-4691.
32. Harper, K. C.; Sigman, M. S., Predicting and Optimizing Asymmetric Catalyst Performance Using the Principles of Experimental Design and Steric Parameters. *Proc. Natl. Acad. Sci.* **2011**, *108* (6), 2179-2183.
33. Harper, K. C.; Sigman, M. S., Three-Dimensional Correlation of Steric and Electronic Free Energy Relationships Guides Asymmetric Propargylation. *Science* **2011**, *333* (6051), 1875-1878.
34. Harper, K. C.; Bess, E. N.; Sigman, M. S., Multidimensional Steric Parameters in the Analysis of Asymmetric Catalytic Reactions. *Nat. Chem.* **2012**, *4* (5), 366-374.
35. Kuhn, M.; Johnson, K., *Applied Predictive Modeling*. Springer: 2013.

CHAPTER 2

DEVELOPMENT OF PHOSPHINE PARAMETERS AND APPLICATION TO AN ARYL-ARYL SUZUKI COUPLING REACTION

Introduction

Phosphine ligands are ubiquitous in organometallic chemistry, and have thus been the focus of numerous mechanistic studies. One common feature of these studies is the utilization of the extensive parameters within LFERs to correlate reaction outcomes. Two notable long-term projects from different groups have sought to develop nuanced novel descriptors. The first, from Warren Giering and coworkers,¹ attempted to deconstruct phosphine electronic effects into σ -donor and π -donor/acceptor ability. This method was termed quantitative analysis of ligand effects (QALE). First published in 1985, the group used multiple correlations to determine three classes of phosphine ligands. The primary correlation for this separation was the relationship between the pK_a of the phosphines and the standard oxidation potential of $\text{MeCpMn}(\text{CO})_2\text{L}_i$ complexes (Figure 2.1). As protons cannot participate in π -backbonding, the pK_a is a reflection of pure σ -donation from the phosphine. For many phosphines (termed class II), the measured pK_a linearly correlates with the oxidation potential. However, numerous complexes were distinct outliers in this relationship. Those phosphine complexes that were significantly more difficult to oxidize than expected were termed class III. This class was thought to participate in significant

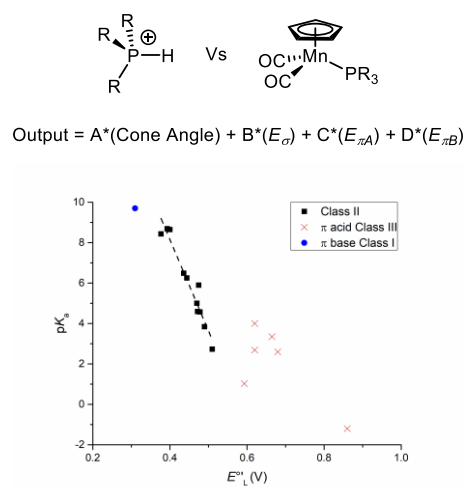


Figure 2.1. Giering and coworkers studied the type of ligand binding with phosphines, defining which types were π -acceptors and donors.

π -backbonding from the metal to the phosphorus, resulting in a less electron rich metal. Examples include phosphites (P(OR)_3), which are electron-poor. The converse effect defined class I, wherein the phosphine is both a σ - and π -donor, resulting in a more electron rich metal. These complexes thus were easier to oxidize than expected based on the $\text{p}K_a$. The π -acceptor or -donor ability was quantified as the difference between the $\text{p}K_a$ predicted oxidation potential and the measured oxidation potential. The only phosphine measured in this class at the time was PCy_3 , a strongly donating ligand. Therefore, Giering and coworkers used these parameters, along with Tolman's cone angle, to determine the relative importance of these effects on chemical reactivity. Similar to Tolman's original work, they found that steric interactions sometimes played an outsized role, termed the steric threshold. Using these tools, the group analyzed the relative rates of substitution reactions and oxidative additions. Extensive follow-up work used these retrospective analysis tools to interrogate the role of phosphine ligands.²

In a significant study from Fey, Harvey, Orpen, and coworkers, a "ligand knowledge base" was constructed.³ In order to enable the extensive collection of ligand parameters, the group only utilized calculated structures, and all measurements were related to energetics. This approach allows extensive and rapid collection of parameters, a key advantage over Giering's approach. Structures for the free ligand (\mathbf{L}_i), protonated ligand ($\mathbf{L}_i\text{H}^+$), $\mathbf{L}_i\text{AuCl}$, $[\text{PdCl}_3\mathbf{L}_i]^-$, $\text{Pt}(\text{PH}_3)_3\mathbf{L}_i$, and $\text{BH}_3\mathbf{L}_i$ complexes were optimized (Figure 2.2).⁴ Parameters were collected from these structures, including the relative energies, bond distances and angles, HOMO-LUMO energies, and partial charges. Additionally, a seventh structure was optimized using the free ligand and eight helium atoms, termed He_8 , to energetically measure the ligand size. The collected parameters

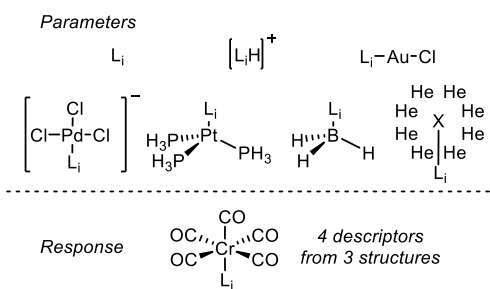


Figure 2.2. Parameters from Fey and coworkers utilized seven computed structures. These descriptors were used to predict the *trans* Cr-CO binding energy.

were used in a QSAR type approach to model two different response variables. However, the published models suffer from numerous drawbacks. First, a Buchwald-Hartwig coupling reaction was probed, wherein the amine contained a dye that was used to quantify the reaction product yield in fluorescence resonance energy transfer. The models obtained by the group were overly complicated and could neither be interpreted nor used in a predictive manner. The second case study used the *trans* CO bond dissociation energy (BDE) from the computed $[\text{Cr}(\text{CO})_5\text{L}_4]$ complexes as the response variable. In this example, the models identified were relatively simple; however, four parameters from three different computed complexes were necessary to predict this energy, again limiting interpretation or extrapolation. These two examples highlight the continued need for predictive descriptors that can be broadly applied to understand the role of ligands in diverse organometallic reactions.

In light of these studies, three goals were of paramount importance. First, computational parameters should be used whenever possible to minimize the effort necessary to expand the ligand set and to facilitate future virtual screening. Second, all parameters must measure an intrinsic property that relates to the mechanism of action. And finally, the structures and parameters should be broadly applicable rather than specific to a single binding mode. With these goals in mind, Anat Milo, a postdoctoral scholar in the Sigman group, had initially investigated a small set of phosphines. Following previous work⁵ within the group, she envisioned that infrared stretching frequencies could be used to accurately describe phosphine ligands (Figure 2.3) and had chosen to focus on PR_3 ligands. Hypothesizing that the ligands may be forced into a different orientation upon binding the metal compared to the unbound state, she elected to

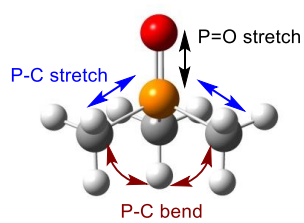


Figure 2.3. Infrared stretching parameters collected.

calculate the phosphine oxide compounds. Thus, the oxygen would serve two purposes: first, the oxygen could act as a surrogate for the metal and restrict the possible conformations. Secondly, as the stretching frequencies were to be identified manually from a list of all calculated motions, the P=O stretch would be visually distinct and thus easily recognized. Additionally, the symmetric stretching and bending motions of the three P–C bonds were selected. These frequencies and intensities were collected along with the Tolman cone angles and the Tolman electronic parameter values.⁶

In searching for a viable reaction to study, we sought two characteristics. First, the reaction product ratios needed to be affected by the ligand choice. Importantly, this ligand choice had to affect the selectivity in a single reaction step, resulting in a constant product ratio over time. Second, the reaction would preferably be simple to set up and perform and the product ratios needed to be readily and accurately measured. Therefore, we turned to a well-known Suzuki reaction between *o*-tolyl boronic acid and 4-chlorophenyltriflate (**1**, Figure 2.4).

The palladium-catalyzed Suzuki reaction between 4-chloro-phenyltriflate and *o*-tolyl boronic acid was originally published by Fu and coworkers⁷ wherein the chemoselectivity was defined by the choice of phosphine ligands. When utilizing tricyclohexyl phosphine (PCy₃), the group was able to isolate 83% of product **3** resulting from oxidative addition of the triflate electrophile. Surprisingly, when the Fu group utilized tri-*tert*-butyl phosphine (PtBu₃), **2** was the predominant product. The selective activation of an aryl chloride in the presence of an aryl triflate had not been previously reported.

Schoenebeck and Houk subsequently computationally probed the origin of the

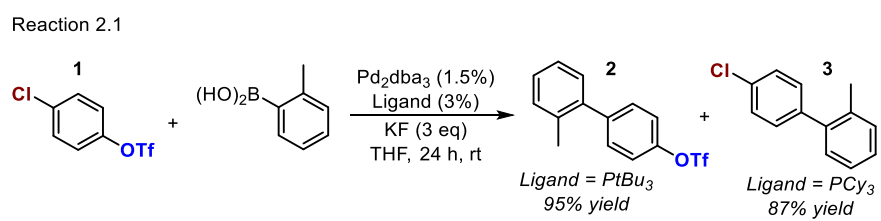


Figure 2.4. Suzuki coupling reaction conditions between Aryl group **1** and *o*-TolB(OH)₂.

observed ligand dependent selectivity switch.⁸ Computations of the oxidative addition of the bis- and mono-ligated palladium complexes (PdL_{i2} and PdL_i) were computed with four phosphines: PH_3 , PMe_3 , PCy_3 , and PtBu_3 . The relative energies of the transition states were compared to reveal the likely reaction pathways. The energetic preference for $\text{Pd}(\text{PtBu}_3)$ was computed to be 5.8 kcal/mol, favoring oxidative insertion at the C–Cl bond, in agreement with the experimental isolation of solely the product that contains the triflate. However, when the transition states of the monoligated complex $\text{Pd}(\text{PCy}_3)$ were compared, the oxidative addition to the C–Cl bond was still found to be preferred (3.6 kcal/mol), in contrast with the experimental results. This caused a reanalysis of the mechanism, allowing the authors to uncover the importance of the loss of a ligand from PdL_{i2} . Previous experimental work from Hartwig had demonstrated that the rate of oxidative addition of $\text{Pd}(\text{PCy}_3)_n$ to aryl chlorides was inversely correlated to phosphine concentration.⁹ Therefore, Schoenebeck and Houk calculated the bis-ligated pathway, which, for PCy_3 , was found to have an energetic preference of 4.3 kcal/mol toward triflate insertion. This selectivity trend is in agreement with experiment, and the computations with PH_3 and PMe_3 showed this switch in selectivity preference was general. However, the PdL_i reaction pathway was still lower in energy. The authors concluded that the primary driver of site selectivity within this system was the higher population of $\text{Pd}(\text{PCy}_3)_2$ whereas use of PtBu_3 enables access to the monoligated complex. Support for this hypothesis comes from the relative energy of the PdL_{i2} and PdL_i complexes. With PCy_3 as a ligand, the PdL_{i2} complex is 20.5 kcal/mol lower in energy than the PdL_i complex. The authors hypothesize that the very low population of this complex limits any productive PdL_i reaction pathways. Unfortunately, the energy

difference between these two complexes for $PtBu_3$ was not reported.

Further analysis of the origin of these selectivities was performed with PMe_3 using the activation/strain model developed by Bickelhaupt¹⁰ and Houk (Figure 2.5).¹¹ The distortion of the C–Cl bond is significantly lower in energy than the distortion of the C–O bond, in agreement with the bond dissociation energies. However, when the C–O bond is distorted, the LUMO is drastically lowered. Therefore, when the nucleophilic PdL_{i2} complex approaches, its high lying HOMO interacts with the LUMO to lower the overall energy enough to prefer the insertion to the triflate. This interaction is smaller in the PdL_i complex, thus, the BDE preference overrides the interaction energy. Overall, the oxidative addition of the PdL_i complexes are lower in energy due to the very small distortion energies from this complex, whereas the PdL_{i2} incurs a significant penalty to attain the necessary geometry.

Through these studies, many questions had been addressed as to the origin of the selectivity switch. A remaining quandary was the role the ligands play in selectivity other than in the PdL_{i2} or PdL_i pathways. Schoenebeck, in a more recent report, published in 2014 had shown that both pathways are viable for $PtBu_2iPr$, and the selectivity could be augmented based on the amount of phosphine added.¹² This conclusion provided further evidence for the hypothesis that the populations of the mono- versus bis-ligated complexes were primary drivers of selectivity. These selectivities were more accurately predicted in 2015 in a followup paper from the same group in which they showed the importance of computational dispersion corrections.¹³ However, both of these papers were published after most of the work detailed in this chapter had been performed.

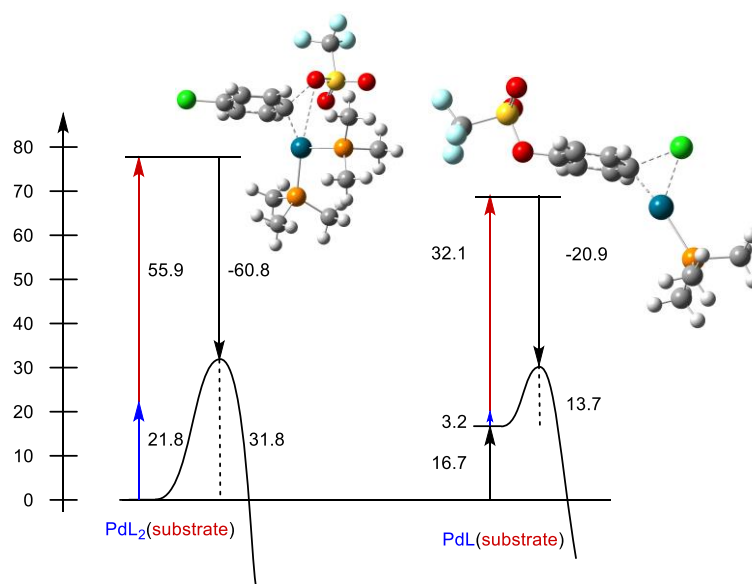


Figure 2.5. Interaction/distortion analysis from Schoenebeck and Houk of $\text{Pd}(\text{PMe}_3)_n$ oxidative addition to **1** in reaction 2.1.

Experimental Analysis and Multivariate Modeling of

Observed Ligand Effects

To begin our work, 27 monodentate phosphines were selected to represent the diversity of structures possible (Figure 2.6). This group included many commonly used phosphines, such as triphenyl phosphine (PPh₃), tri-*o*-tolyl phosphine (P*o*-Tol₃), P*t*Bu₃, and PCy₃. Nonsymmetric ligands were also examined, such as P*t*Bu₂Ph and PEtPh₂. Additionally, we selected five “Buchwald” type ligands that include a biaryl substituent. The development of these ligands was crucial in expanding the reaction scope in Buchwald-Hartwig couplings, allowing for significantly less activated bonds to engage in oxidative additions under milder conditions.¹⁴ Each ligand was utilized in the aforementioned Suzuki coupling reaction, and the product ratios **2:3** were measured (Figure 2.7). The reaction selectivity did not change over time, but the selectivity was highly sensitive to the ligand. Conversion of these reaction selectivities to energetic preferences according to the Curtin-Hammett principle revealed the large spread of energy outputs from -2.72 kcal/mol (P*t*Bu₃) to 4.77 kcal/mol (P(*o*-OMePh)₃). This upper bound was at the absolute limit of the detection range, further underscoring the drastic switch in selectivity.

Concurrent to testing and measuring the reaction selectivities, parameter identification was performed (Figure 2.8). One of the key challenges in systematically identifying parameters for phosphine ligands is represented by the conformational freedom that many phosphines possess. Therefore, we performed a computational conformational search using the phosphine oxide structures. Geometries within 3 kcal/mol of the global minimum were identified. This threshold was thought to provide a

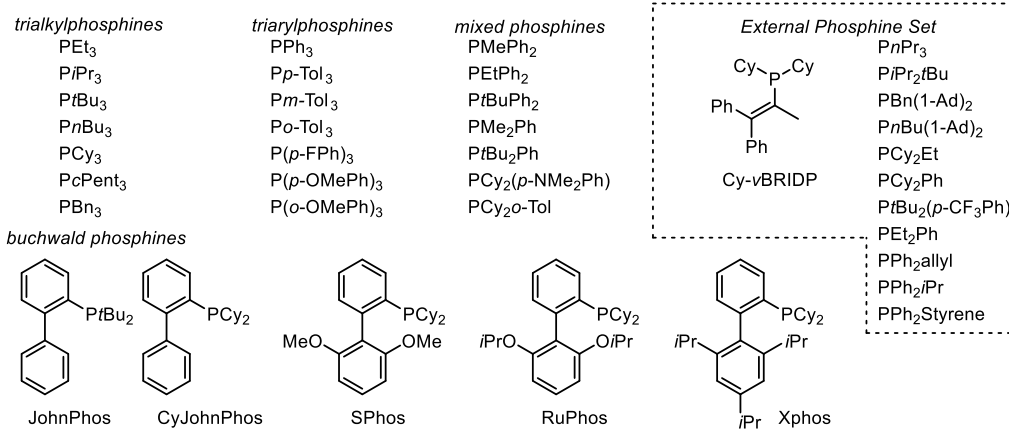


Figure 2.6. Phosphine ligands included in this study.

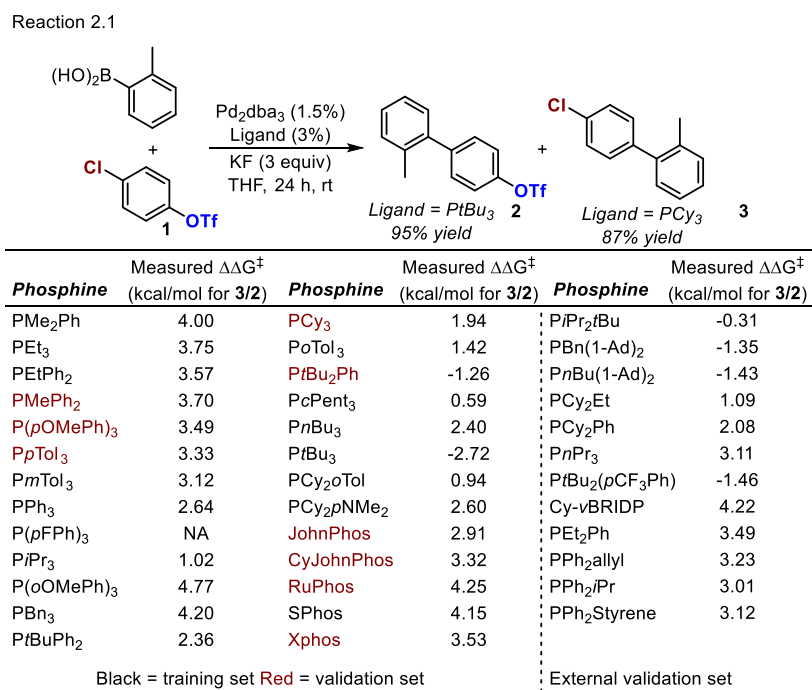


Figure 2.7. All phosphine ligands tested in this study, as well as measured $\Delta\Delta G^\ddagger$ and predicted $\Delta\Delta G^\ddagger$ in three models presented.

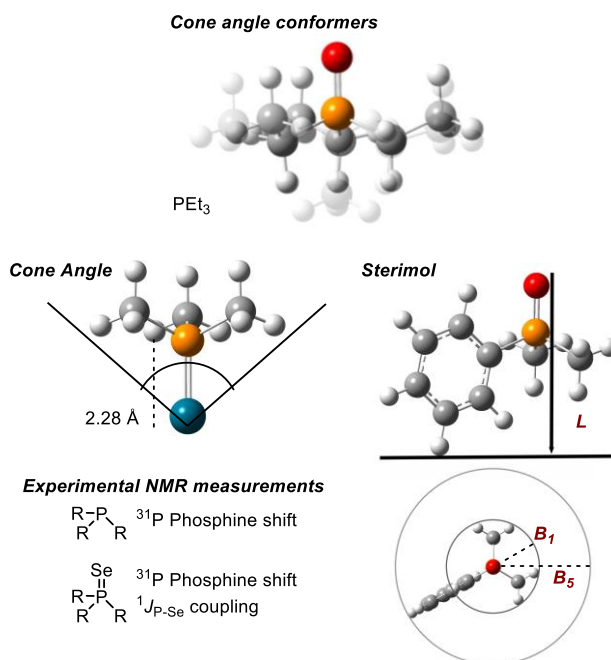


Figure 2.8. Differences in conformer geometry for PEt₃ as well as parameters collected and utilized in this study.

reasonable window of geometries for which the ligand could readily access. From the identified structures, the oxygen atom was converted to a palladium atom, and the bond distance was set to 2.28 Å. A solid cone angle was measured using these complexes.¹⁵ The distance was chosen to replicate the distance used by Tolman.¹⁶ Shorter and longer distances were considered; however, this only resulted in a uniform change to the measured cone angle and thus did not affect the relative measured angles. We hypothesized that the largest and smallest cone angle conformers may be preferred in different reaction sequences, and these conformers were collected. Examples of the conformers identified from triethyl phosphine (PEt₃) are shown, where one ethyl group rotates away from the oxygen center (dark grey maximum cone angle, light grey minimum cone angle). This lowers the cone angle measurement with only a small energetic penalty. These two geometries were selected for further parameter identification.

Extensive parameters were collected from the selected optimized phosphine oxide geometries. As mentioned previously, calculated IR stretching frequencies and intensities were collected. The HOMO and LUMO energies and dipole moments were easily extracted. In addition to the cone angles, we also pursued other geometry based parameters. Having success previously using Sterimol values,¹⁷ we measured the L, B₁, and B₅ values. These values are three-dimensional representations of the size of the structure. Starting from the oxygen atom, in the direction of the phosphorus atom, the ligand length is measured (L). Orthogonal to this bond, the minimum (B₁) and maximum (B₅) radii of the molecule are calculated. We also experimentally measured ³¹P NMR shifts from the phosphines and phosphine selenides, as well as the P–Se coupling

constant. These parameters are relatively easily measured and were previously found to be useful in correlating reactivity.¹⁸

Parameters were first compared to better understand their meaning. Following Fey and coworker's example, principle component analysis was performed, revealing complex relationships between parameters. However, univariate correlations between descriptors were found that facilitated our understanding (Figure 2.9). Unsurprisingly, the ³¹P NMR shifts of the phosphine and phosphine selenide correlated to each other. Additionally, these parameters correlated to the P=O stretching frequency. Linear trends were not identified for the P-C bending and stretching motions. However, when interrogating subsets of phosphines, these vibrational modes revealed trends. For example, using only trialkyl or triaryl phosphines established that cone angle measurements were positively correlated to the P-C bending frequency. The P-C stretching frequency linearly correlated with the Ni(CO)₃L_i CO stretching frequency for the alkyl phosphines. However, the P-C stretching frequency did not vary for the aryl phosphines. Intriguingly, the P=O stretching frequency compared to the calculated proton affinity from Fey and coworkers revealed a relationship that could not be understood. Finally, the parameters from the minimum and maximum cone angle conformers were compared. Many parameters from the two sets showed linear trends. However, other parameters also show large differences in their values. Hence, we decided to include parameters from each set in the full parameters collection.

Following parameter investigations, we turned to modeling the observed outcomes for the reaction in Figure 2.7. Parameters were first normalized by subtracting the mean and dividing by the standard deviation. This results in the parameter sets having

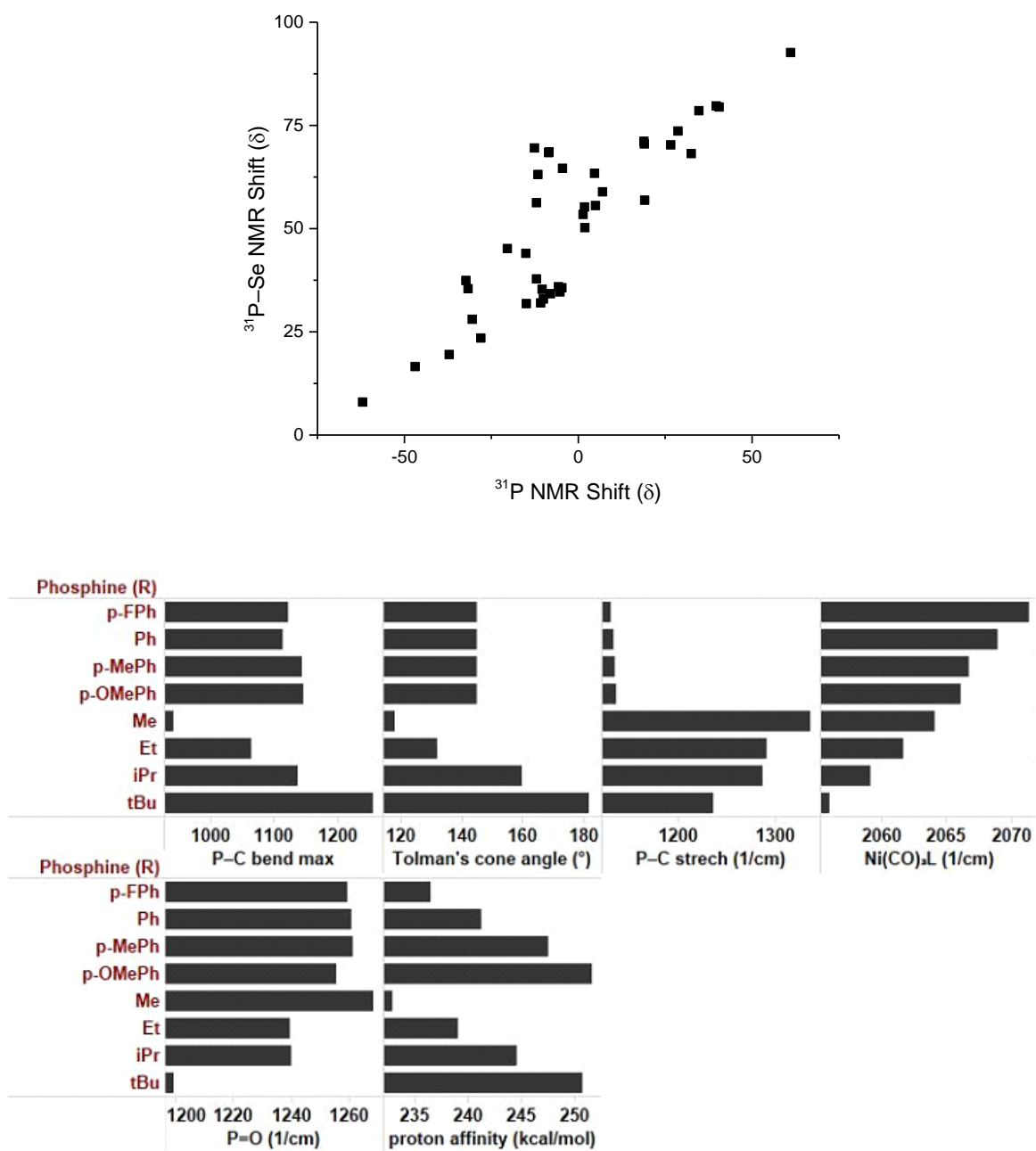


Figure 2.9. Multiple visualization methods revealed complex trends between calculated infrared parameters.

an average of 0, and a standard deviation of 1, allowing for direct comparisons between different parameters. To facilitate model identification, the ligand set was split into a training and a validation set.¹⁹ This split was performed intuitively rather than by a strict scientific process. For example, training set ligands were selected to contain examples from the triaryl-, trialkyl-, and mixed- phosphines, as well as one Buchwald class phosphine. Twelve additional ligands were also tested and designated an external validation set for confirmation of the model. From the training set, models were evaluated using several linear regression techniques. The method that proved fruitful was to identify a relatively simple equation with minimal descriptors and a modest correlation (R^2). Parameters were then manually added and removed from the equation, eventually resulting in a model with adequate predictability (Figure 2.10 and Figure 2.11). In total, the optimal model encompasses 41 ligands with a high correlation coefficient ($R^2 = 0.88$). Thus, this model successfully accomplishes one of the goals set out at the beginning of the project: we were able to develop new parameters that adequately predict chemical reactivity. However, since the model is composed of five parameters in six terms (including four crossterms), its mechanistic interpretation is not straightforward.

Mechanistic Interrogation and Reanalysis

Due to the complexity of the model, the proposed mechanism was revisited, centering on the idea that ligand binding primarily dictates chemoselectivity. Amatore, Jutand, and coworkers, measured the kinetic role of PPh_3 in oxidative addition using cyclic voltammetry.²⁰ They concluded that PdL_{i2} was the primary complex in solution and this species was able to directly add to phenyl iodide. However, Hartwig and Paul

Reaction 2.1

<i>Phosphine</i>	Measured $\Delta\Delta G^\ddagger$ (kcal/mol for 3/2)	Predicted $\Delta\Delta G^\ddagger$ (Full Model)	Predicted $\Delta\Delta G^\ddagger$ (Smaller Model)	Predicted $\Delta\Delta G^\ddagger$ (Larger Model)
PMe ₂ Ph	4.00	3.86	4.01	
PEt ₃	3.75	3.97	3.78	
PEtPh ₂	3.57	3.85	3.62	
PMePh ₂	3.70	3.83	3.66	
P(<i>p</i> -OMePh) ₃	3.49	2.89	3.50	
P <i>p</i> -Tol ₃	3.33	2.83	3.23	
P <i>m</i> -Tol ₃	3.12	2.51	3.01	
PPh ₃	2.64	2.60	2.77	
P(<i>p</i> -FPh) ₃	NA	ND		
P <i>i</i> Pr ₃	1.02	0.99		0.27
P(<i>o</i> -OMePh) ₃	4.77	4.97		5.19
PBn ₃	4.20	2.84		3.67
P <i>t</i> BuPh ₂	2.36	2.77		1.58
PCy ₃	1.94	1.88		1.39
P <i>o</i> -Tol ₃	1.42	1.90		4.37
P <i>t</i> Bu ₂ Ph	-1.26	-0.87		-0.59
P <i>o</i> Pent ₃	0.59	1.15		0.95
P <i>n</i> Bu ₃	2.40	2.02		3.46
P <i>t</i> Bu ₃	-2.72	-2.79		-1.87
PCy ₂ <i>o</i> -Tol	0.94	1.12		0.98
PCy ₂ (<i>p</i> NMe ₂ Ph)	2.60	2.99		1.92
JohnPhos	2.91	2.13	2.58	
CyJohnPhos	3.32	4.64	3.73	
RuPhos	4.25	4.33	4.06	
SPhos	4.15	4.06	4.14	
Xphos	3.53	3.22	3.61	
<hr style="border-top: 1px dashed black;"/>				
<u>External Set</u>				
P <i>i</i> Pr ₂ <i>t</i> Bu	-0.31	0.69		-0.51
PBn(1-Ad) ₂	-1.35	2.36		0.49
P <i>n</i> Bu(1-Ad) ₂	-1.43	1.69		0.29
PCy ₂ Et	1.09	1.90		1.74
PCy ₂ Ph	2.08	1.67		1.71
P <i>n</i> Pr ₃	3.11	2.61		3.65
P <i>t</i> Bu ₂ (<i>p</i> CF ₃ Ph)	-1.46	-1.26		-0.62
Cy- <i>v</i> BRIDP	4.22	3.59		0.84
PEt ₂ Ph	3.49	1.92	3.63	
PPh ₂ allyl	3.23	2.74	2.97	
PPh ₂ <i>i</i> Pr	3.01	2.67	2.52	
PPh ₂ Styrene	3.12	2.47	2.84	

Figure 2.10. Measured and predicted values for all ligands tested.

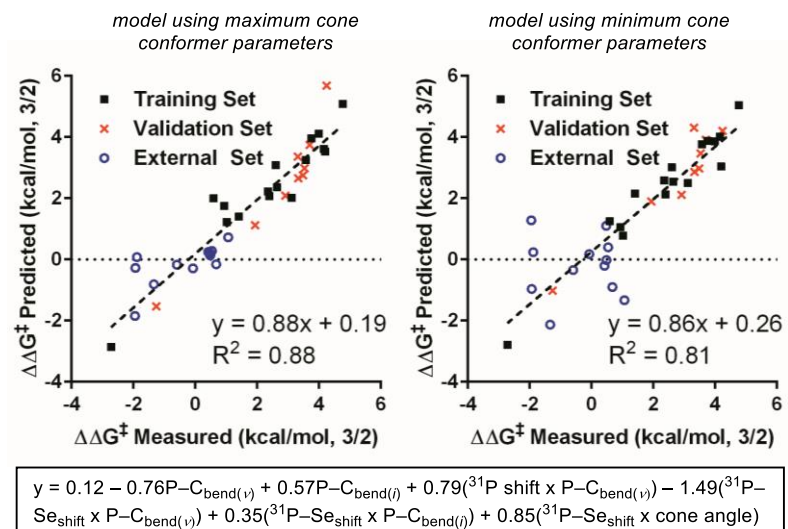


Figure 2.11. Models identified using the minimum and maximum cone angle conformers. The equation using the maximum cone angle conformers is displayed. Reoptimization of the parameter coefficients using the minimum cone angle conformer drastically reduces the ability of the model to predict external validations.

explored the use of *Po*-Tol₃ in the oxidative addition of 4-*tert*-butyl-bromo-benzene and concluded that PdL₂ first lost a ligand prior to oxidative addition.²¹ According to our measurements, PPh₃ and *Po*-Tol₃ differ in maximum cone angle by 15° (131° and 146°, respectively). Thus, hypothesizing that phosphine size could augment the mechanism, we elected to analyze the role of ligand:metal ratios in the selectivity outcome. Initial tests had been performed at a 1:1 ratio in accordance with Fu and coworkers original reaction conditions. To interrogate the proposed mechanism, the ligand:metal ratio was varied from 0.25:1 to 2.5:1. Additionally, we chose to characterize the complexes in solution using cyclic voltammetry according to the procedure outlined by Amatore, Jutand, and coworkers.

In agreement with Fu and coworkers report, high ligand:metal ratios (>2:1) inhibited the reaction when *Pt*Bu₃ was used as the ligand (Figure 2.12). However, when the reaction did occur (ligand:metal ratio 1:1 and lower), only product **2** was obtained. An opposite trend was observed with triethyl phosphine (PEt₃), wherein only product **3** was formed, and no reaction was observed with low ligand:metal ratios (<0.25:1). These two results were interpreted as being primarily an effect of steric interactions. Therefore, PCy₃ and *Pi*Pr₃, which present intermediate size within the ligands set, were similarly tested. These ligands provided moderate selectivity when a 1:1 ligand:metal ratio was used, however, when these ligands were tested with low ligand:metal ratios, the products ratio was found to significantly shift towards **2**. Conversely, high ligand:metal ratios drastically increased the selectivity for the formation of **3**. The selectivity dependence on the ligand:Pd ratio is higher for PCy₃ than *Pi*Pr₃. Low ligand:metal ratios yield approximately a 2:1 ratio, whereas high ligand:metal ratios resulted in greater than 99:1

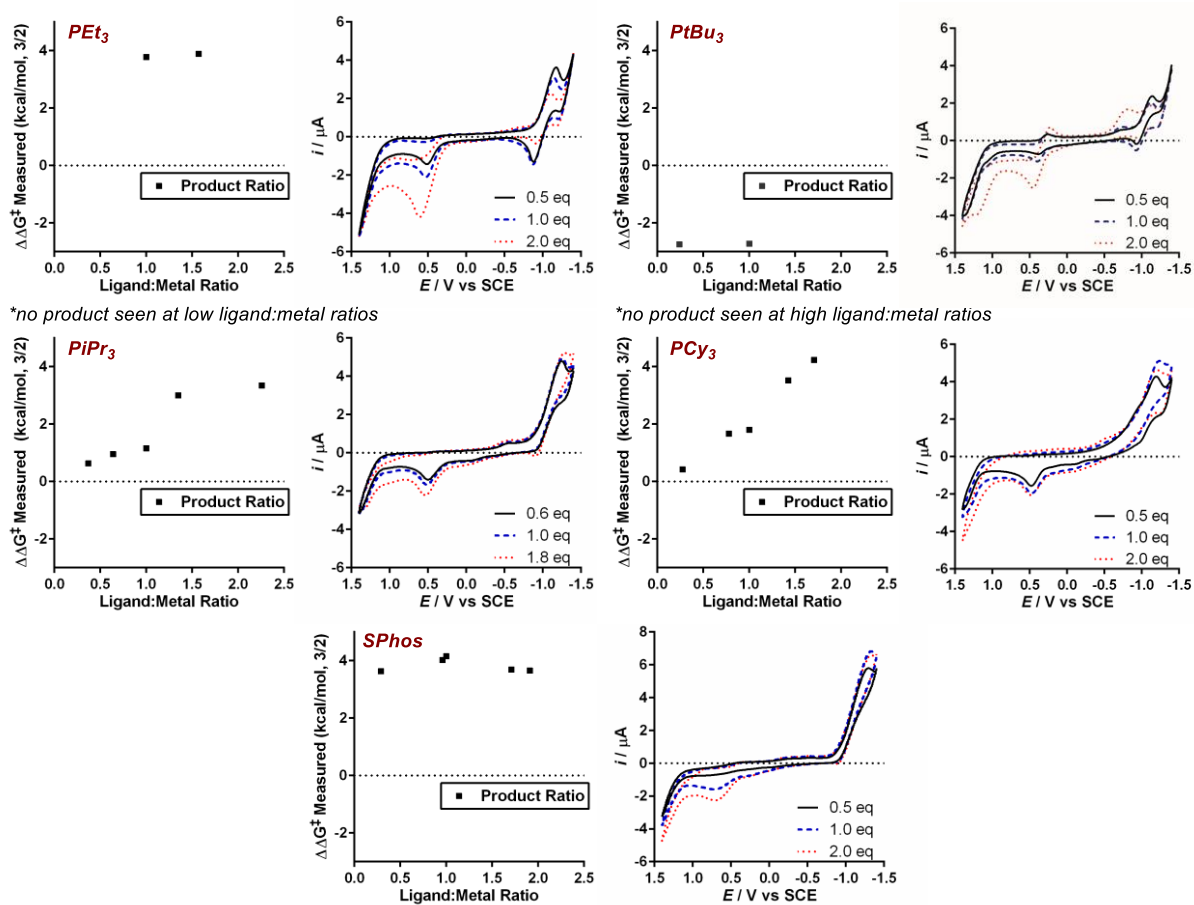


Figure 2.12. Comparative analysis of product ratios versus ligand:metal ratios as well as cyclic voltammetry measurements.

selectivity for **3**.

Finally, the unique nature of the Buchwald class of ligands was considered. These ligands likely occupy two metal binding sites despite only containing a single donor atom. The biaryl ring is hypothesized to orient itself so that a *cis*- coordination site on palladium is blocked.²² This feature has been important in facilitating normally challenging reductive eliminations and stabilization of the palladium(0) complex.²³ The product ratio **2:3** was found to be independent from the ligand:metal ratio for this class of ligands.

In agreement with literature precedent, we found via cyclic voltammetry that $\text{PdL}_{i2}(\text{dba})$ is the most abundant species in solution despite changes to the ligand:metal ratio.²⁰ This is also in agreement with Schoenebeck and Houk's calculations, which showed that the monoligated (Pd^{L}) complex is significantly higher in energy.

Overall, the study of the dependence of the product selectivity on the ligand:metal ratio is in agreement with Schoenebeck and Houk's mechanistic proposal. The increased ligand:metal ratios reduces the possibility of forming the PdL_i complex, thereby increasing the selectivity for formation of the product **3**. Lower ratios allowed for ligand dissociation, increasing the formation of product **2** via oxidative addition of the C-Cl bond to the PdL_i complex. Based on this mechanism, we chose to define our ligand data set into two subsets. The first contained "large" ligands (cone angle $> 130^\circ$ [PPh_3]) All phosphines with smaller measured cone angles were grouped together in the second group. As the Buchwald class of ligands reacted similarly to the small ligands, we added this subset to the second group.

Modeling of the overall selectivities upon separation of the ligands into the two

subsets provided much more satisfying relationships (Figure 2.13). The large phosphines, containing 10 training set ligands, 2 validations, and 7 external validations, are accurately predicted solely by the ^{31}P -Se shift. An R^2 equal to 0.86 suggests that this shift relates to the ability for the phosphine ligand to stabilize the PdL_i complex. In other words, more electron donating ligands (higher ^{31}P -Se NMR shift) allow dissociation of a ligand from PdL_{i2} , thus increasing the formation of the triflate containing product **2**. This effect is seen most clearly through comparison of two representative ligands. Strongly deshielded structures, such as PtBu_3 ($\delta = 92.7$ ppm) result in selective addition to the C-Cl bond ($\Delta\Delta G^\ddagger = -2.72$ kcal/mol). Minimally deshielded ligands, like $\text{P}n\text{Pr}_3$ ($\delta = 35.5$ ppm) result in selective addition to the triflate ($\Delta\Delta G^\ddagger = 3.11$ kcal/mol). In between these extremes, lower selectivity is observed. Intriguingly, $\text{P}o\text{-Tol}_3$ does not align with this trend, which may be due to an associative displacement in favor of a dissociative pathway;²¹ however, this possibility was not investigated. Instead, we turned our attention to the second subset of ligands, the small and Buchwald class.

Models for the small and Buchwald ligands were searched for using univariate and multivariate correlations. Unfortunately, linear trends were not encountered. However, the four-parameter model in Figure 2.13 was identified utilizing a training set of six ligands with seven validation points and five external validations ($R^2 = 0.84$). Importantly, the Buchwald class of ligands is well predicted despite only one ligand within this class being included in the training set. Parameters derived from the minimum cone angle conformer were determined to be significantly more accurate when considering the external validations, likely implicating the strained steric environment encountered by these complexes during the oxidative addition step with the PdL_2

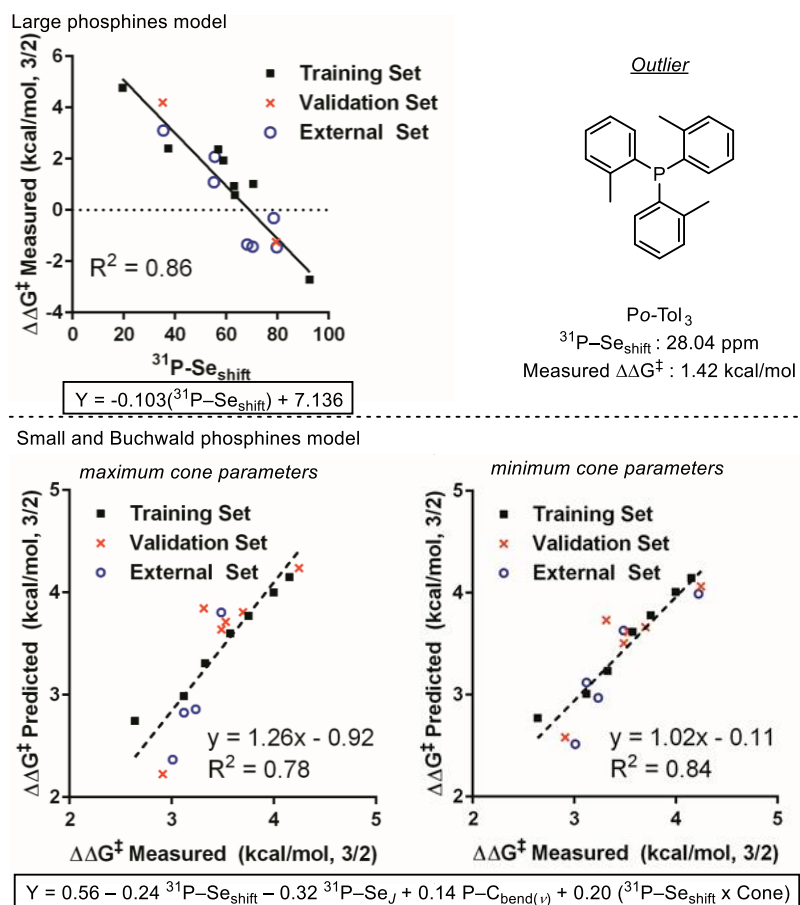


Figure 2.13. Models developed using the split subsets of ligands.

complex. One linear term, the P–Se coupling constant, has previously been related to the ligand nucleophilicity via an inverse correlation to the measured proton affinity.^{18a, 24} Therefore, we hypothesized that increased nucleophilicity yields increased selectivity for addition to the triflate. For example, P(*p*-OMePh)₃ is more nucleophilic than PPh₃ (714 Hz versus 730 Hz), and this change results in a large increase in selectivity ($\Delta\Delta G^\ddagger = 3.5$ kcal/mol versus 2.6 kcal/mol). The Buchwald ligands similarly follow this trend, wherein the most nucleophilic ligand in this class (RuPhos, 694 Hz) is the most selective ($\Delta\Delta G^\ddagger = 4.2$ kcal/mol). Similarly, the dependence of the selectivity on steric requirements is clear, as larger ligands (high cone angle) result in more selective reactions. For example, SPhos (minimum cone angle = 202°) is more selective than CyJohnPhos (minimum cone angle = 184°) by 0.9 kcal/mol ($\Delta\Delta G^\ddagger = 4.2$ kcal/mol versus 3.3 kcal/mol). This correlation may indicate that when two coordination sites are uniformly blocked, large complexes increase the distortion of the C–O bond at the oxidative addition transition state. This would further lower the LUMO energy, the primary cause of selectivity according to Schoenebeck and Houk.⁸ A decreased LUMO would result in higher selectivity for addition to the triflate bond to give product **2**.

In conclusion, we have successfully modeled phosphine ligands in complex mechanistic environments. The models obtained were utilized within a comprehensive investigation into the role of the ligand framework in influencing reaction pathways. First, the model in Figure 2.10 was found, which allowed us to predict the reaction selectivity for a large external validation set. However, as this model provided limited mechanistic insights into the reaction, previous knowledge of the reaction sequence by other groups was used in conjunction with electrochemical and ligand binding studies in

order to access a rational bifurcation of the ligand set. Such a split allowed us to obtain two simpler models that were found to be highly informative of the factors influencing the reaction outcome. Follow-up work utilizing these parameters focused on probing less well understood reaction mechanisms, as described in the next chapter.

Experimental

General Considerations

Phosphine **12** was purchased from Acros Organics, phosphine **14** was purchased from Oakwood Chemical, and phosphine **16** was purchased from Strem Chemicals. All others were purchased from Sigma-Aldrich. Upon receipt phosphines were stored under a N₂ atmosphere in a VAC glove box. Butyl vinyl ether (Sigma-Aldrich), bromobenzene (Sigma-Aldrich), Palladium(II) acetate (Combi-Blocks), and Dimethylacetamide (Sigma-Aldrich) were all used as received. Diisopropylethylamine was distilled over calcium hydride and stored under N₂. 4-chlorophenyl trifluoromethanesulfonyl (**1**) was prepared from 4-chlorophenol according to literature procedure.²⁵ *O*-tolyl boronic acid was bought from Frontier Scientific and used as received. Tris(dibenzylideneacetone)dipalladium(0) was synthesized according to a literature procedure.²⁶ Potassium fluoride (J. T. Baker Chemical Company) was used as received. THF was dried by passing through a column of activated alumina (Innovative Technology), deoxygenated and stored in a glove box. ¹H spectra were obtained at 500 MHz. ¹³C spectra were obtained at 125 MHz and referenced to CDCl₃ at 77 ppm. ³¹P spectra were obtained at 202 MHz with reference to an 85% phosphoric acid at 0 ppm. GC separations were performed on an Agilent 7890A GC with a flame ionization detector equipped with a DB-5 column using a 50:1 split. IR

spectra were recorded using a Thermo Nicolet FT-IR.

Phosphines

The phosphines used in this study are labeled in Figure 2.6 and are numbered in Table 2.1.

Conformational Search

A conformational search on the respective phosphine oxides was performed using the MacroModel suite from Schrödinger²⁷ using an OPLS_2005 force field without solvent corrections. A Monte-Carlo molecular mechanics method was employed with extended torsional sampling. The output was restricted to 20 structures within 3.11 kcal/mol (13 kJ/mol) of the lowest energy conformer, with a maximum atom deviation cutoff of 1 Å. All phosphines except **4** and **7** were found to have fewer than 20 stable conformers with these conditions. Due to their added torsional degrees of freedom, these two phosphines were found to have many more than 20 stable conformers. It was assumed that by restricting the possible output a representative sample of conformers would be identified. The Buchwald phosphines and Cy-vBRIDP were restricted to having the aryl ring (implicated in blocking a coordination site) in a similar direction as the P=O bond. This was thought to ensure similarity to how the phosphine would be bound. Conformers were submitted to a geometry optimization in Gaussian 09²⁸ using the 6-31+G(d,p) basis set and M06-2x functional. This basis set was chosen in order to match the conformational search basis set. The M06-2x functional was chosen because of its accuracy for a large number of main group systems.²⁹ Cone angle measurements were

Table 2.1. Phosphines in this study. Phosphines 27-38 comprise the “External Set.”

Phosphine Name	#	Phosphine Name	#
PEt ₃	1	PCy ₂ (<i>p</i> -NMe ₂ Ph)	21
P <i>i</i> Pr ₃	2	JohnPhos	22
P <i>t</i> Bu ₃	3	CyJohnPhos	23
P <i>n</i> Bu ₃	4	SPhos	24
PCy ₃	5	RuPhos	25
P <i>c</i> Pent ₃	6	XPhos	26
PBn ₃	7	P <i>i</i> Pr ₂ <i>t</i> Bu	27
PPh ₃	8	PBn(1-Ad) ₂	28
P(<i>o</i> -OMePh) ₃	9	P <i>n</i> Bu(1-Ad) ₂	29
P <i>o</i> -Tol ₃	10	PCy ₂ Et	30
P <i>m</i> -Tol ₃	11	PCy ₂ Ph	31
P(<i>p</i> -OMePh) ₃	12	P <i>n</i> Pr ₃	32
P <i>p</i> -Tol ₃	13	P <i>t</i> Bu ₂ (<i>p</i> -CF ₃ Ph)	33
P(<i>p</i> -FPh) ₃	14	Cy- <i>v</i> BRIDP	34
PMePh ₂	15	PEt ₂ Ph	35
PEtPh ₂	16	PPh ₂ allyl	36
P <i>t</i> BuPh ₂	17	PPh ₂ <i>i</i> Pr	37
PMe ₂ Ph	18	PPh ₂ Styrene	38
P <i>t</i> Bu ₂ Ph	19		
PCy ₂ <i>o</i> -Tol	20		

performed by changing the oxygen atom to palladium and setting the distance between palladium and phosphorus to 2.28 Å and then measuring angles with the program Solid-G.³⁰ Conformers with the largest and smallest cone angles were then submitted to an optimization and frequency calculation at the M06-2x/def2-TZVP level of theory to obtain IR vibration data. A triple zeta potential basis set was chosen along with the M06-2x functional, as these generally lead to quantitative correlations.^{29, 31} Linear scaling factors³² were not applied to the calculated vibrations because these are constants, and thus would not affect correlation. Cone angle measurements were then recalculated for consistency, and Sterimol measurements were performed with Molecular Modeling Pro.³³

Parameters

Calculated parameters are included in the following four tables. Table 2.2 contains three parameters from NMR spectra. Table 2.3 contains calculated parameters for the conformer with the minimum solid cone angle, followed by Table 2.4, which contains the parameters for the conformer with the maximum solid cone angle. Table 2.5 contains the average values from steric measurements.

Reaction 2.1 Procedure

Palladium (13.7 mg, 0.015 mmol, 0.015 equiv) was weighed into a 4 mL vial followed by the appropriate ligand (0.03 mmol, 0.03 equiv). Potassium fluoride (174 mg, 3 mmol, 3 eq) was added, followed by *o*-tolyl boronic acid (136 mg, 1 mmol, 1 equiv). 2-Methoxy naphthalene (1-2 mg) was added as an internal standard. THF (2 mL) was then added, followed by 4-Chloro-Phenyl trifluoromethane sulfonyl (260 mg, 1 mmol, 1

Table 2.2. NMR parameters.

#	Phosphine ^{31}P NMR shift (δ)	Phosphine selenide ^{31}P NMR shift (δ)	$^1J_{\text{P-Se}}$ coupling (Hz)	#	Phosphine ^{31}P NMR shift (δ)	Phosphine selenide ^{31}P NMR shift (δ)	$^1J_{\text{P-Se}}$ coupling (Hz)
1	-20.4	45.2	684	20	-11.6	63.1	687
2	19.0	70.5	686	21	1.4	53.2	687
3	61.1	92.9	687	22	18.9	71.2	739
4	-32.3	37.4	681	23	-12.6	69.5	703
5	7.0	58.9	675	24	-8.4	68.6	699
6	4.7	63.4	685	25	-8.5	68.4	694
7	-10.4	35.3	730	26	-12.0	56.2	721
8	-4.7	35.7	731	27	34.7	78.6	689
9	-37.1	20.2	723	28	32.5	68.2	693
10	-30.5	28.0	706	29	26.6	70.3	680
11	-5.7	35.9	723	30	1.8	55.2	672
12	-10.8	32.0	714	31	5.0	55.6	703
13	-8.0	34.2	720	32	-31.7	35.5	676
14	-10.0	32.9	743	33	39.7	79.7	720
15	-28.0	23.3	719	34	-4.5	64.6	687
16	-12.0	37.8	722	35	-15.1	44.0	709
17	19.1	57.0	717	36	-14.9	31.8	730
18	-46.9	16.6	705	37	1.9	50.2	722
19	40.5	79.7	708	38	-5.2	34.7	729

Table 2.3. Minimum cone angle conformer parameters.

#	Cone Min (°)	P=O Stretch Frequency Min (cm ⁻¹)	P=O Intensity Min	P-C Bend Frequency Min (cm ⁻¹)	P-C Bend Intensity	P-C stretch Frequency Min (cm ⁻¹)	P-C stretch Intensity	B ₁ min	B ₅ min	L min	L/B ₁ min	B ₁ *L min
1	121.5	1237.87	115.6594	1066.63	5.2089	1317.06	59.7259	3.03	4.85	5.30	1.75	16.07
2	136.4	1227.40	118.8375	1134.34	1.3320	1282.77	1.1349	3.63	4.90	5.46	1.50	19.84
3	153.2	1199.56	88.8838	1255.95	7.2231	1237.60	31.0499	4.11	4.90	5.42	1.32	22.26
4	152.5	1258.36	37.6873	1206.43	43.0472	1238.08	28.9350	4.43	6.51	4.61	1.04	20.43
5	144.7	1221.41	88.5239	1252.52	20.2350	1243.66	32.0046	3.91	6.84	6.43	1.64	25.14
6	151.2	1222.99	74.4246	1230.39	23.5757	1289.81	11.0221	3.65	6.05	6.34	1.73	23.15
7	139.5	1282.30	104.8169	1253.80	37.0667	1202.54	14.9968	3.45	7.38	8.52	2.47	29.42
8	131.4	1261.07	139.7130	1113.54	10.1234	1134.33	0.1587	4.09	6.28	5.86	1.43	23.98
9	136.6	1234.92	111.1535	1308.49	10.6744	1129.99	85.3356	4.53	6.47	7.14	1.58	32.31
10	146.7	1233.18	75.7177	1094.45	1.9478	1079.92	1.4911	4.23	6.45	6.69	1.58	28.27
11	131.3	1243.01	62.4941	1122.70	2.8605	1145.95	1.1457	4.75	6.27	7.07	1.49	33.55
12	130.4	1254.73	200.3020	1141.93	6.6700	1139.29	5.1911	5.00	8.16	6.80	1.36	33.99
13	131.1	1261.30	112.8954	1144.16	7.1692	1135.96	4.4867	5.03	7.51	5.86	1.17	29.46
14	131.5	1259.63	155.5339	1122.31	11.4407	1131.64	0.2370	4.26	6.97	5.85	1.37	24.96
15	126.4	1262.53	147.4326	1114.22	10.1021	1144.00	18.9401	3.25	6.33	6.03	1.86	19.61
16	122.0	1247.89	127.5210	1300.83	24.8563	1311.66	23.7568	3.30	6.45	5.97	1.81	19.67
17	142.4	1228.15	39.7156	1258.79	41.5703	1244.62	33.5062	3.93	6.44	5.88	1.50	23.08
18	118.3	1266.79	157.0018	913.81	37.8364	1330.78	55.1457	3.04	6.34	6.09	2.01	18.49
19	148.3	1214.63	48.9249	1260.22	20.1918	1241.56	17.2387	4.00	6.45	5.86	1.47	23.44

Table 2.3. continued.

#	Cone Min (°)	P=O Stretch Frequency Min (cm ⁻¹)	P=O Intensity Min	P-C Bend Frequency Min (cm ⁻¹)	P-C Bend Intensity	P-C stretch Frequency Min (cm ⁻¹)	P-C stretch Intensity	B ₁ min	B ₅ min	L min	L/B ₁ min	B ₁ *L min
20	167.0	1220.18	86.8561	1253.80	40.2333	1229.63	9.7721	3.92	6.25	6.57	1.68	25.75
21	169.6	1251.81	25.3442	1113.57	10.1844	1222.11	100.1940	4.45	8.87	6.59	1.48	29.37
22	181.1	1215.03	48.7180	1259.74	30.0869	1241.29	39.3911	3.97	6.11	7.69	1.94	30.58
23	183.6	1223.70	84.0109	1256.68	46.0350	1236.65	9.1758	4.03	6.50	7.14	1.77	28.79
24	201.9	1224.47	69.0783	1258.14	36.2487	1237.96	11.5267	4.08	7.01	7.78	1.91	31.74
25	187.5	1220.81	21.4533	1255.71	68.3069	1228.08	17.5406	4.59	8.31	7.73	1.68	35.45
26	209.8	1220.88	84.9711	1259.29	37.1985	1237.66	3.6326	4.08	7.81	9.35	2.29	38.14
27	143.3	1222.14	81.6724	1251.43	19.0937	1241.98	13.2144	3.69	4.90	5.46	1.48	20.14
28	156.9	1239.94	59.2340	1296.29	0.9613	1221.17	28.5915	3.77	7.49	6.30	1.67	23.75
29	152.2	1226.88	95.0274	1295.19	0.9084	1201.51	6.6054	4.72	6.85	6.25	1.33	29.48
30	137.7	1232.65	109.6675	1141.36	3.4763	1226.10	7.0568	3.57	6.81	5.41	1.52	19.28
31	139.7	1254.19	100.4733	1143.52	16.7418	1209.98	6.2531	4.50	6.79	6.37	1.42	28.69
32	139.9	1243.53	35.6645	1217.30	69.3565	1281.80	45.3706	3.16	5.39	6.81	2.15	21.54
33	148.3	1260.75	17.6870	1211.05	49.7760	1241.39	27.1819	3.99	8.16	5.83	1.46	23.24
34	189.5	1251.55	68.0050	1168.49	13.2797	1228.88	33.5848	4.93	8.49	8.14	1.65	40.16
35	124.6	1241.53	109.4800	1264.27	7.4887	1306.65	9.2429	3.24	6.34	5.98	1.84	19.37
36	127.5	1273.09	128.9369	1113.92	8.4844	1140.64	22.1946	3.37	6.33	6.70	1.99	22.58
37	129.1	1245.95	127.6977	1117.16	1.3407	1140.90	18.8888	3.45	6.33	5.96	1.73	20.56
38	131.1	1260.55	140.2790	1113.05	6.5072	1134.86	1.0050	4.12	8.84	5.87	1.42	24.21

Table 2.4. Maximum cone angle parameters.

#	Cone Max (°)	P=O Stretch Frequency Max (cm ⁻¹)	P=O Intensity Max	P-C Bend Frequency Max (cm ⁻¹)	P-C Bend Intensity	P-C stretch Frequency Max (cm ⁻¹)	P-C stretch Intensity	B ₁ max	B ₅ max	L max	L/B ₁ max	B ₁ *L max
1	129.7	1239.45	91.8126	1065.25	0.3568	1292.13	29.6284	3.47	4.88	4.46	1.28	15.49
2	142.1	1240.01	118.8737	1138.16	0.2757	1288.37	0.7078	3.58	4.91	5.42	1.52	19.38
3	153.2	1199.56	88.8838	1255.95	7.2231	1237.60	31.0499	4.11	4.90	5.42	1.32	22.26
4	179.2	1245.04	30.7557	1188.77	36.6596	1238.49	59.8627	4.28	5.38	5.40	1.26	23.09
5	171.8	1216.37	79.8276	1252.08	30.1615	1237.05	10.1394	4.47	6.49	6.34	1.42	28.36
6	178.6	1225.85	52.2649	1238.69	17.5932	1251.23	11.4806	4.39	5.55	4.78	1.09	20.97
7	152.4	1266.48	59.3206	1252.96	24.7647	1207.22	0.2912	4.40	7.24	5.02	1.14	22.08
8	131.4	1261.07	139.7130	1113.54	10.1234	1134.33	0.1587	4.09	6.28	5.86	1.43	23.98
9	142.7	1258.26	81.1309	1315.35	67.5850	1125.23	16.1051	4.35	6.39	7.37	1.69	32.09
10	156.6	1236.39	81.8515	1096.62	1.7403	1079.82	1.3043	4.57	6.23	5.61	1.23	25.65
11	134.9	1249.34	61.3331	1122.45	8.8714	1145.88	2.2974	4.85	7.22	6.65	1.37	32.22
12	131.5	1255.62	149.1985	1147.54	3.5378	1136.36	18.1880	5.24	8.65	6.04	1.15	31.67
13	131.1	1261.30	112.8954	1144.16	7.1692	1135.96	4.4867	5.03	7.51	5.86	1.17	29.46
14	131.5	1259.63	155.5339	1122.31	11.4407	1131.64	0.2370	4.26	6.97	5.85	1.37	24.96
15	126.4	1262.53	147.4326	1114.22	10.1021	1144.00	18.9401	3.25	6.33	6.03	1.86	19.61
16	132.7	1250.62	88.2520	1269.80	43.6616	1291.70	22.3041	3.23	6.34	6.03	1.86	19.49
17	142.5	1228.15	39.7156	1258.79	41.5703	1244.62	33.5062	3.93	6.44	5.88	1.50	23.08
18	118.3	1266.79	157.0018	913.81	37.8364	1330.78	55.1457	3.04	6.34	6.09	2.01	18.49
19	148.3	1214.63	48.9249	1260.22	20.1918	1241.56	17.2387	4.00	6.45	5.86	1.47	23.44
20	183.0	1223.79	72.9619	1254.76	30.4316	1233.35	9.3115	4.38	6.09	6.36	1.45	27.88

Table 2.4. continued.

#	Cone Max (°)	P=O Stretch Frequency Max (cm ⁻¹)	P=O Intensity Max	P-C Bend Frequency Max (cm ⁻¹)	P-C Bend Intensity	P-C stretch Frequency Max (cm ⁻¹)	P-C stretch Intensity	B ₁ max	B ₅ max	L max	L/B ₁ max	B ₁ *L max
21	169.6	1251.81	25.3442	1113.57	10.1844	1222.11	100.1940	4.45	8.87	6.59	1.48	29.37
22	181.1	1215.03	48.7180	1259.74	30.0869	1241.29	39.3911	3.97	6.11	7.69	1.94	30.58
23	203.0	1227.83	45.4314	1255.53	57.7637	1232.62	15.1624	4.37	6.04	7.76	1.78	33.86
24	214.8	1226.98	61.5668	1255.99	44.3317	1235.30	9.9534	4.61	7.16	7.74	1.68	35.66
25	209.7	1230.22	90.7899	1251.94	48.0333	1222.46	2.5508	5.04	7.96	7.53	1.49	37.95
26	234.2	1226.40	60.0447	1254.42	45.8524	1233.01	13.0255	4.56	7.84	9.65	2.12	44.00
27	147.7	1225.40	69.1903	1254.71	34.1659	1245.42	17.8383	3.95	4.90	5.41	1.37	21.35
28	156.9	1239.94	59.2340	1296.29	0.9613	1221.17	28.5915	3.77	7.49	6.30	1.67	23.75
29	166.6	1229.42	90.9588	1295.07	0.5268	1195.18	11.6189	4.73	6.85	6.28	1.33	29.72
30	144.3	1239.29	115.9502	1143.29	5.2631	1226.27	1.7639	3.79	6.80	5.09	1.34	19.27
31	144.8	1245.30	125.2118	1141.94	2.7931	1209.19	7.0553	4.68	6.81	6.05	1.29	28.29
32	155.5	1251.41	80.2126	1216.31	39.4691	1266.78	9.3112	3.51	5.34	4.59	1.31	16.12
33	148.3	1211.05	49.7760	1260.75	17.6870	1241.39	27.1819	3.99	8.16	5.83	1.46	23.24
34	203.3	1251.95	40.8703	1167.22	6.5350	1230.42	43.3206	4.45	8.57	7.62	1.71	33.90
35	131.9	1247.22	113.1423	1272.12	28.7351	1305.87	24.2715	3.25	6.29	6.10	1.88	19.83
36	136.3	1270.33	120.6109	1115.39	9.6464	1141.24	22.3802	3.24	6.34	6.02	1.86	19.47
37	137.7	1256.49	131.0494	1113.98	11.8877	1140.95	18.7288	3.98	6.33	6.03	1.52	24.03
38	131.3	1260.99	146.6413	1113.01	5.7150	1135.73	1.4900	4.10	8.32	6.84	1.67	28.02

Table 2.5. Average steric values.

#	cone ave	B ₁ ave	B ₅ ave	L ave	L/B ₁ ave	B ₁ *L ave	#	cone ave	B ₁ ave	B ₅ ave	L ave	L/B ₁ ave	B ₁ *L ave
1	125.62	3.25	4.87	4.88	1.50	15.87	20	175.00	4.15	6.17	6.47	1.56	26.84
2	139.24	3.61	4.90	5.44	1.51	19.61	21	169.55	4.45	8.87	6.59	1.48	29.37
3	153.19	4.11	4.90	5.42	1.32	22.26	22	181.12	3.97	6.11	7.69	1.94	30.58
4	165.86	4.36	5.94	5.00	1.15	21.79	23	193.28	4.20	6.27	7.45	1.78	31.27
5	158.22	4.19	6.67	6.39	1.52	26.76	24	208.31	4.34	7.08	7.76	1.79	33.70
6	164.88	4.02	5.80	5.56	1.38	22.34	25	198.62	4.82	8.13	7.63	1.58	36.72
7	145.97	3.93	7.31	6.77	1.72	26.58	26	221.97	4.32	7.83	9.50	2.20	41.04
8	131.38	4.09	6.28	5.86	1.43	23.98	27	145.50	3.82	4.90	5.44	1.43	20.75
9	139.65	4.44	6.43	7.25	1.63	32.21	28	156.90	3.77	7.49	6.30	1.67	23.75
10	151.63	4.40	6.34	6.15	1.40	27.05	29	159.40	4.73	6.85	6.27	1.33	29.60
11	133.10	4.80	6.75	6.86	1.43	32.89	30	141.00	3.68	6.81	5.25	1.43	19.28
12	130.95	5.12	8.41	6.42	1.25	32.88	31	142.25	4.59	6.80	6.21	1.36	28.49
13	131.07	5.03	7.51	5.86	1.17	29.46	32	147.70	3.34	5.37	5.70	1.73	18.83
14	131.50	4.26	6.97	5.85	1.37	24.96	33	148.30	3.99	8.16	5.83	1.46	23.24
15	126.41	3.25	6.33	6.03	1.86	19.61	34	196.40	4.69	8.53	7.88	1.68	37.03
16	127.36	3.26	6.39	6.00	1.84	19.58	35	128.25	3.25	6.32	6.04	1.86	19.60
17	142.44	3.93	6.44	5.88	1.50	23.08	36	131.90	3.31	6.34	6.36	1.93	21.03
18	118.33	3.04	6.34	6.09	2.01	18.49	37	133.40	3.72	6.33	6.00	1.63	22.30
19	148.27	4.00	6.45	5.86	1.47	23.44	38	131.20	4.11	8.58	6.36	1.55	26.12

equiv). A stir bar was added to the vial which was then capped and removed from the glove box. The reaction mixture was stirred for 24 h at room temperature. Vials were then diluted with ethyl acetate and an aliquot was passed through a short silica plug. GC measurements were performed on the crude reaction mixture. Comparison of NMR and GC product ratios showed that products **2** and **3** had similar responses, so crude ratios were used. Table 2.6 contains product ratios for each reaction. Reaction with phosphine 14 had low yield and thus was excluded from the training set. Similarly, one reaction using phosphine 16 resulted in low yield and was excluded. Phosphine 33 also resulted in low yield; however, as this was part of the validation set and was only predicted, this result was not removed. Table 2.7 contains the product ratios measured based on the ligand:metal ratio used in the reaction. Table 2.8 contains the normalized parameter values that were used in constructing the models presented in Figure 2.11 and Figure 2.13. Table 2.9 contains predicted values versus measured values for all models. Yellow indicates that these predictions are for the larger phosphines in models built for the smaller and Buchwald phosphines. Blue indicates that these predictions are for the smaller and Buchwald phosphines in models built for the larger phosphines.

Phosphine Selenide Preparation

Phosphine selenides were prepared using a modified literature procedure.^{18a} Approximately 20mg of selenium powder (Alfa Aesar) was placed in an NMR tube in a nitrogen filled glove box. A capillary tube of 85% phosphoric acid was added as reference (0 ppm). The phosphine was then added, along with CDCl₃ and the NMR tube was capped and removed from the glove box. The tube was then refluxed in an oil bath

Table 2.6. Product ratios for reaction 1.

#	Run 1		Run 2		Run 3		Average $\Delta\Delta G^\ddagger$
	Ratio	Yield	Ratio	Yield	Ratio	Yield	
1	3.668	48	3.814	47	3.780	49	3.780
2	0.942	12	0.962	16	1.184	17	1.029
3	-2.355	10	-3.009	59	-3.066	83	-2.810
4	2.416	54	2.426	48	2.361	49	2.401
5	1.627	71	3.301	Quant	1.799	85	2.242
6	0.570	51	0.631	41	0.573	33	0.592
7	4.294	87	4.084	88	4.227	74	4.202
8	2.682	5	2.643	5	2.601	5	2.642
9	4.853	Quant	4.596	Quant	4.910	Quant	4.786
10	1.376	9	1.453	9	1.420	10	1.416
11	3.183	12	3.116	11	3.065	11	3.121
12	3.516	27	3.593	29	3.372	25	3.493
13	3.881	15	3.116	11	3.232	12	3.409
14							
15	4.055	17	3.372	10	3.899	12	3.776
16		1	4.282	18	3.420	10	3.690
17	2.283	28	2.429	32	2.372	27	2.362
18	3.949	35	4.290	38	3.838	29	4.026
19	-1.162	5	-1.136	7	-1.536	10	-1.278
20	0.952	10	0.916	8	0.955	7	0.941
21	2.756	74	2.417	63	2.686	56	2.620
22	2.640	3	3.049	7	3.183	7	2.957
23	4.004	37	3.909	36	2.816	32	3.576
24	4.133	11	4.352	11	4.279	6	4.255
25	4.065	11	4.173	11	4.235	9	4.157
26	3.564	22	3.382	22	3.685	21	3.545
27	-0.312	17					
28	-1.346	15					
29	-1.428	41					
30	1.089	59					
31	2.083	47					
32	3.105	42					
33	-1.456	0.6					
34	4.222	42					
35	3.485	6					
36	3.233	9					
37	3.010	45					
38	3.120	4					

Table 2.7. Product ratios as a function of ligand to metal ratio.

Phosphine	MW	ratio ligand:metal	GC product ratio	Yield (%)
PEt ₃	118	0.70	N/D	<2
		1.00*	3.78*	48*
		1.57	3.89	12
P <i>i</i> Pr ₃	180	0.37	0.63	13
		0.64	0.95	21
		1.00*	1.16*	15*
		1.35	3.00	76
		2.26	3.35	3
P <i>t</i> Bu ₃	202	0.24	-2.75	49
		1.00*	-2.72*	51*
		2.54	N/D	<2
PCy ₃	280	0.28	0.42	7
		0.78	1.67	30
		1.00*	1.80*	93*
		1.43	3.52	77
		1.71	4.24	23
SPhos	410	0.29	3.63	4
		0.96	4.02	36
		1.00*	4.16*	9*
		1.71	3.69	9
		1.91	3.65	17
P <i>Bn</i> ₃	304	0.48	4.19	63
		1.00*	4.22*	83*
		2.19	4.40	41
P(<i>o</i> -OMePh) ₃	352	0.22	4.03	Quant
		1.00*	4.91*	Quant*
		2.02	4.42	48
P <i>t</i> BuPh ₂	242	0.25	1.55	10
		1.00*	2.37*	29*
		4.11	4.63	50

*Average of three runs

Table 2.8. Normalized values.

Phosphine	$\Delta\Delta G^\ddagger$ (kcal/mol)	^{31}P NMR Shift (δ)	^{31}PSe NMR Shift (δ)	$^1\text{J}_{\text{P-Se}}$ (Hz)	cone max ($^\circ$)	cone min ($^\circ$)	Max P-C bend Frequency (cm^{-1})	Max P-C bend intensity	Min P-C bend Frequency (cm^{-1})
PMe_3	1.340	-2.338	-2.097	-1.032	-1.581	-1.576	-2.623	-0.802	-2.618
PEt_3	3.751	-0.681	-0.256	-1.032	-0.880	-1.072	-1.299	-1.135	-1.279
PiPr_3	1.022	0.889	1.000	-0.930	-0.449	-0.442	-0.514	-1.139	-0.549
PtBu_3	-2.717	2.567	2.097	-0.879	-0.062	0.271	0.755	-0.757	0.761
PnBu_3	2.401	-1.155	-0.639	-1.186	0.844	0.243	0.031	0.865	0.227
PCy_3	1.937	0.411	0.425	-1.492	0.585	-0.090	0.713	0.507	0.724
PcPent_3	0.591	0.319	0.648	-0.981	0.821	0.187	0.569	-0.185	0.485
PBn_3	4.195	-0.282	-0.744	1.315	-0.090	-0.308	0.722	0.210	0.738
PPh_3	2.641	-0.055	-0.726	1.315	-0.822	-0.653	-0.779	-0.597	-0.773
Pp-Tol_3	3.328	-0.187	-0.797	0.805	-0.833	-0.666	-0.449	-0.760	-0.444
Pm-Tol_3	3.119	-0.095	-0.714	0.958	-0.699	-0.657	-0.683	-0.666	-0.675
Po-Tol_3	1.416	-1.083	-1.104	0.090	0.056	-0.005	-0.961	-1.059	-0.979
$\text{P}(p\text{-FPh})_3$	2.185	-0.266	-0.861	1.979	-0.817	-0.650	-0.685	-0.524	-0.679
$\text{P}(p\text{-OMePh})_3$	3.486	-0.298	-0.908	0.499	-0.818	-0.695	-0.413	-0.960	-0.468
$\text{P}(o\text{-OMePh})_3$	4.770	-1.346	-1.527	0.958	-0.429	-0.431	1.394	2.569	1.327
PMePh_2	3.700	-0.983	-1.330	0.754	-0.996	-0.863	-0.772	-0.598	-0.766
PEtPh_2	3.571	-0.346	-0.620	0.907	-0.775	-1.051	0.904	1.251	1.244
PtBuPh_2	2.359	0.893	0.325	0.345	-0.437	-0.185	0.785	1.136	0.791
PMe_2Ph	3.997	-1.736	-1.673	0.039	-1.277	-1.206	-2.930	0.930	-2.925
PtBu_2Ph	-1.257	1.746	1.444	0.192	-0.234	0.063	0.801	-0.042	0.807

Table 2.8. continued.

Phosphine	$\Delta\Delta G^\ddagger$ (kcal/mol)	^{31}P NMR Shift (δ)	^{31}PSe NMR Shift (δ)	$^1\text{J}_{\text{P-Se}}$ (Hz)	cone max ($^\circ$)	cone min ($^\circ$)	Max P-C bend Frequency (cm^{-1})	Max P-C bend intensity	Min P-C bend Frequency (cm^{-1})
PCy ₂ (<i>p</i> -NMe ₂ Ph)	2.601	0.188	0.154	-0.420	0.508	0.964	-0.779	-0.593	-0.773
PCy ₂ <i>o</i> -Tol	0.941	-0.330	0.633	-1.186	0.976	0.856	0.742	0.522	0.738
JohnPhos	2.911	0.885	1.032	1.774	0.911	1.454	0.796	0.503	0.802
CyJohnPhos	3.316	-0.370	0.952	-0.063	1.672	1.559	0.750	2.028	0.769
SPhos	4.153	-0.203	0.904	-0.267	2.083	2.333	0.755	1.288	0.784
RuPhos	4.247	-0.206	0.896	-0.522	1.907	1.725	0.712	1.492	0.758
XPhos	3.530	-0.346	0.295	0.141	2.759	2.668	0.738	1.372	0.797
Cy- ν BRIDP	4.222	-0.047	0.707	-0.879	1.685	1.809	-0.201	-0.795	-0.181
PnPr ₃	3.105	-1.130	-0.737	-1.441	0.019	-0.292	0.328	1.020	0.344
PiPr ₂ <i>t</i> Bu	-0.312	1.515	1.398	-0.777	-0.255	-0.150	0.741	0.728	0.712
PBn(1-Ad) ₂	-1.346	1.427	0.885	-0.573	0.068	0.429	1.189	-1.102	1.195
PnBu(1-Ad) ₂	-1.428	1.192	0.989	-1.237	0.405	0.227	1.176	-1.126	1.184
PCy ₂ Et	1.089	0.204	0.243	-1.645	-0.373	-0.386	-0.459	-0.865	-0.474
PCy ₂ Ph	2.083	0.331	0.260	-0.063	-0.355	-0.299	-0.473	-1.001	-0.450
PtBu ₂ (<i>p</i> -CF ₃ Ph)	-1.456	1.714	1.456	0.805	-0.234	0.062	0.806	-0.180	0.277
PEt ₂ Ph	3.485	-0.468	-0.313	0.243	-0.805	-0.942	0.929	0.429	0.850
PPh ₂ allyl	3.233	-0.462	-0.917	1.315	-0.650	-0.819	-0.759	-0.623	-0.769
PPh ₂ <i>i</i> Pr	3.010	0.209	-0.004	0.907	-0.603	-0.750	-0.774	-0.500	-0.734
PPh ₂ Styrene	3.120	-0.077	-0.776	1.264	-0.824	-0.663	-0.785	-0.840	-0.779

Table 2.9. Predicted versus measured values.

#	Measured	Figure 2.11 Max Predicted	Figure 2.11 Min Predicted	Figure 2.13 max Predicted	Figure 2.13 min Predicted	Figure 2.13 large phosphines Predicted
1	3.75	3.93	4.17	3.78	3.77	2.72
2	1.02	0.99	0.92	3.07	3.01	0.27
3	-2.72	-2.79	-2.48	3.35	3.02	-1.87
4	2.40	2.02	2.56	4.29	4.29	3.46
5	1.94	1.88	-0.10	4.20	4.54	1.39
6	0.59	1.15	0.69	3.78	4.12	0.95
7	4.20	2.84	3.55	3.10	3.12	3.67
8	2.64	2.60	2.25	2.77	2.75	3.63
9	4.77	4.97	5.07	4.01	4.34	5.19
10	1.42	1.90	1.60	3.44	3.46	4.37
11	3.12	2.51	2.04	3.01	2.99	3.61
12	3.49	2.89	2.62	3.50	3.64	3.99
13	3.33	2.83	2.46	3.23	3.31	3.77
15	3.70	3.83	3.59	3.66	3.81	4.81
16	3.57	3.85	3.18	3.62	3.60	3.43
17	2.36	2.77	2.21	3.12	3.14	1.58
18	4.00	3.86	3.93	4.01	4.00	5.48
19	-1.26	-0.87	-1.27	2.79	2.55	-0.59
20	0.94	1.12	1.49	4.16	4.38	0.98
21	2.60	2.99	3.41	3.31	3.25	1.92
22	2.91	2.13	3.18	2.58	2.23	0.21
23	3.32	4.64	3.31	3.73	3.85	0.36
24	4.15	4.06	4.22	4.14	4.15	0.46
25	4.25	4.33	5.93	4.06	4.24	0.47
26	3.53	3.22	2.81	3.61	3.71	1.64
27	-0.31	0.69	-1.80	3.25	3.23	-0.51
28	-1.35	2.36	2.66	3.51	3.41	0.49
29	-1.43	1.69	0.41	3.75	3.86	0.29
30	1.09	1.90	1.57	4.01	4.12	1.74
31	2.08	1.67	2.55	3.04	2.99	1.71
32	3.11	2.61	4.29	4.68	4.88	3.65
33	-1.46	-1.26	4.63	2.26	2.11	-0.62
34	4.22	3.59	-0.29	3.61	4.00	0.84
35	3.49	1.92	0.52	3.63	3.81	2.83
36	3.23	2.74	2.97	2.97	2.86	4.00
37	3.01	2.67	1.82	2.52	2.37	2.23
38	3.12	2.47	2.18	2.84	2.83	3.73

overnight. NMR characterization was then directly taken with an NMR spectrometer tuned to 202.245 MHz.

Phosphine Selenide Characterization

Triethylphosphine selenide

The general procedure for selenide formation was used to prepare this compound from triethylphosphine (1). ^{31}P NMR (CDCl_3 , 202.2 MHz) δ 45.2 ppm ($^1J_{\text{P-Se}} = 684$ Hz).

Triisopropyl-phosphine selenide

The general procedure for selenide formation was used to prepare this compound from triisopropyl-phosphine (2). ^{31}P NMR (CDCl_3 , 202.2 MHz) δ 70.5 ppm ($^1J_{\text{P-Se}} = 686$ Hz).

Tri-*tert*-butyl phosphine selenide

The general procedure for selenide formation was used to prepare this compound from tri-*tert*-butyl phosphine (3). ^{31}P NMR (CDCl_3 , 202.2 MHz) δ 92.9 ppm ($^1J_{\text{P-Se}} = 687$ Hz).

Tri-*n*-butyl phosphine selenide

The general procedure for selenide formation was used to prepare this compound from tri-*n*-butyl phosphine (4). ^{31}P NMR (CDCl_3 , 202.2 MHz) δ 37.4 ppm ($^1J_{\text{P-Se}} = 681$ Hz).

Tricyclohexyl phosphine selenide:

The general procedure for selenide formation was used to prepare this compound from tricyclohexyl phosphine (5). ^{31}P NMR (CDCl_3 , 202.2 MHz) δ 58.9 ppm ($^1J_{\text{P-Se}} = 675$ Hz).

Tricyclopentyl phosphine selenide

The general procedure for selenide formation was used to prepare this compound from tricyclopentyl phosphine (6). ^{31}P NMR (CDCl_3 , 202.2 MHz) δ 63.4 ppm ($^1J_{\text{P-Se}} = 685$ Hz).

Tribenzyl phosphine selenide

The general procedure for selenide formation was used to prepare this compound from tribenzyl phosphine (7). ^{31}P NMR (CDCl_3 , 202.2 MHz) δ 35.3 ppm ($^1J_{\text{P-Se}} = 730$ Hz).

Triphenyl phosphine selenide

The general procedure for selenide formation was used to prepare this compound from triphenyl phosphine (8). ^{31}P NMR (CDCl_3 , 202.2 MHz) δ 35.7 ppm ($^1J_{\text{P-Se}} = 731$ Hz).

Tris(*o*-methoxyphenyl) phosphine selenide

The general procedure for selenide formation was used to prepare this compound from tris (*o*-methoxyphenyl) phosphine (9). ^{31}P NMR (CDCl_3 , 202.2 MHz) δ 20.2 ppm

($^1J_{\text{P-Se}} = 723 \text{ Hz}$).

Tris(*o*-methylphenyl) phosphine selenide

The general procedure for selenide formation was used to prepare this compound from tris(*o*-methylphenyl) phosphine (10). ^{31}P NMR (CDCl_3 , 202.2 MHz) δ 28.0 ppm ($^1J_{\text{P-Se}} = 706 \text{ Hz}$).

Tris(*m*-methylphenyl) phosphine selenide

The general procedure for selenide formation was used to prepare this compound from tris(*m*-methylphenyl) phosphine (11). ^{31}P NMR (CDCl_3 , 202.2 MHz) δ 35.9 ppm ($^1J_{\text{P-Se}} = 723 \text{ Hz}$).

Tris(*p*-methoxyphenyl) phosphine selenide

The general procedure for selenide formation was used to prepare this compound from tris(*p*-methoxyphenyl) phosphine (12). ^{31}P NMR (CDCl_3 , 202.2 MHz) δ 32.0 ppm ($^1J_{\text{P-Se}} = 714 \text{ Hz}$).

Tris(*p*-methylphenyl) phosphine selenide

The general procedure for selenide formation was used to prepare this compound from tris(*p*-methylphenyl) phosphine (13). ^{31}P NMR (CDCl_3 , 202.2 MHz) δ 34.2 ppm ($^1J_{\text{P-Se}} = 720 \text{ Hz}$).

Tris(*p*-fluorophenyl) phosphine selenide

The general procedure for selenide formation was used to prepare this compound from tris(*p*-fluorophenyl) phosphine (14). ^{31}P NMR (CDCl_3 , 202.2 MHz) δ 32.9 ppm ($^1J_{\text{P-Se}} = 743$ Hz).

Methyldiphenylphosphine selenide

The general procedure for selenide formation was used to prepare this compound from methyldiphenyl phosphine (15). ^{31}P NMR (CDCl_3 , 202.2 MHz) δ 23.3 ppm ($^1J_{\text{P-Se}} = 719$ Hz).

Ethyldiphenylphosphine selenide

The general procedure for selenide formation was used to prepare this compound from ethyldiphenyl phosphine (16). ^{31}P NMR (CDCl_3 , 202.2 MHz) δ 37.8 ppm ($^1J_{\text{P-Se}} = 722$ Hz).

tert-Butyldiphenylphosphine selenide

The general procedure for selenide formation was used to prepare this compound from *tert*-butyldiphenyl phosphine (17). ^{31}P NMR (CDCl_3 , 202.2 MHz) δ 57.0 ppm ($^1J_{\text{P-Se}} = 717$ Hz)

Dimethylphenylphosphine selenide

The general procedure for selenide formation was used to prepare this compound from dimethylphenyl phosphine (18). ^{31}P NMR (CDCl_3 , 202.2 MHz) δ 16.6 ppm ($^1J_{\text{P-Se}}$

=705 Hz).

Di-*tert*-butylphenylphosphine selenide

The general procedure for selenide formation was used to prepare this compound from di-*tert*-butylphenyl phosphine (19). ^{31}P NMR (CDCl_3 , 202.2 MHz) δ 79.7 ppm ($^1J_{\text{P-Se}} = 708$ Hz).

Dicyclohexyl(*o*-methylphenyl) phosphine selenide

The general procedure for selenide formation was used to prepare this compound from dicyclohexyl(2-methylphenyl) phosphine (20). ^{31}P NMR (CDCl_3 , 202.2 MHz) δ 63.1 ppm ($^1J_{\text{P-Se}} = 687$ Hz).

Dicyclohexyl(*p*-(*N,N*-dimethylamino)phenyl) phosphine selenide

The general procedure for selenide formation was used to prepare this compound from dicyclohexyl(4-(*N,N*-dimethylamino)phenyl) phosphine (21). ^{31}P NMR (CDCl_3 , 202.2 MHz) δ 53.2 ppm ($^1J_{\text{P-Se}} = 687$ Hz).

(*o*-Biphenyl)di-*tert*-butylphosphine (JohnPhos) selenide

The general procedure for selenide formation was used to prepare this compound from (2-Biphenyl)di-*tert*-butylphosphine (22). ^{31}P NMR (CDCl_3 , 202.2 MHz) δ 71.2 ppm ($^1J_{\text{P-Se}} = 739$ Hz).

(*o*-Biphenyl)dicyclohexylphosphine (CyJohnPhos) selenide

The general procedure for selenide formation was used to prepare this compound from (2-Biphenyl)dicyclohexyl phosphine (23). ^{31}P NMR (CDCl_3 , 202.2 MHz) δ 69.5 ppm ($^1J_{\text{P-Se}} = 703$ Hz).

2-Dicyclohexylphosphino-2',6'-dimethoxybiphenyl (SPhos) selenide

The general procedure for selenide formation was used to prepare this compound from 2-Dicyclohexylphosphino-2',6'-dimethoxybiphenyl (24). ^{31}P NMR (CDCl_3 , 202.2 MHz) δ 68.6 ppm ($^1J_{\text{P-Se}} = 699$ Hz).

2-Dicyclohexylphosphino-2',6'-diisopropoxybiphenyl (RuPhos) selenide

The general procedure for selenide formation was used to prepare this compound from 2-Dicyclohexylphosphino-2',6'-diisopropoxybiphenyl (25). ^{31}P NMR (CDCl_3 , 202.2 MHz) δ 68.4 ppm ($^1J_{\text{P-Se}} = 694$ Hz).

2-Dicyclohexylphosphino-2',4',6'-isopropylbiphenyl (XPhos) selenide

The general procedure for selenide formation was used to prepare this compound from 2-Dicyclohexylphosphino-2',4',6'-isopropylbiphenyl (26). ^{31}P NMR (CDCl_3 , 202.2 MHz) δ 56.2 ppm ($^1J_{\text{P-Se}} = 721$ Hz).

Di-*iso*-propyl-*tert*-butyl phosphine selenide

The general procedure for selenide formation was used to prepare this compound from Di-*iso*-propyl-*tert*-butyl Phosphine (27). ^{31}P NMR (CDCl_3 , 202.2 MHz) δ 78.6 ppm

($^1J_{\text{P-Se}} = 689$ Hz).

Di-(1-Adamantyl)-Benzyl phosphine selenide

The general procedure for selenide formation was used to prepare this compound from Di-(1-Adamantyl)-Benzyl Phosphine (28). ^{31}P NMR (CDCl_3 , 202.2 MHz) δ 68.2 ppm ($^1J_{\text{P-Se}} = 693$ Hz).

Di-(1-Adamantyl)-*n*-Butyl phosphine selenide

The general procedure for selenide formation was used to prepare this compound from Di-(1-Adamantyl)-*n*-Butyl Phosphine (29). ^{31}P NMR (CDCl_3 , 202.2 MHz) δ 70.3 ppm ($^1J_{\text{P-Se}} = 680$ Hz).

Dicyclohexyl-ethyl phosphine selenide

The general procedure for selenide formation was used to prepare this compound from Dicyclohexyl-ethyl Phosphine (30). ^{31}P NMR (CDCl_3 , 202.2 MHz) δ 55.2 ppm ($^1J_{\text{P-Se}} = 672$ Hz).

Dicyclohexyl-phenyl phosphine selenide

The general procedure for selenide formation was used to prepare this compound from Dicyclohexyl-phenyl Phosphine (31). ^{31}P NMR (CDCl_3 , 202.2 MHz) δ 55.6 ppm ($^1J_{\text{P-Se}} = 703$ Hz).

Tri-*n*-propyl phosphine selenide

The general procedure for selenide formation was used to prepare this compound from Tri-*n*-propyl Phosphine (32). ^{31}P NMR (CDCl_3 , 202.2 MHz) δ 35.5 ppm ($^1J_{\text{P-Se}}$ =676 Hz).

Di-*tert*-butyl-(*p*-trifluoromethylphenyl) phosphine selenide

The general procedure for selenide formation was used to prepare this compound from Di-*tert*-butyl-(4-trifluoromethylphenyl) Phosphine (33). ^{31}P NMR (CDCl_3 , 202.2 MHz) δ 79.7 ppm ($^1J_{\text{P-Se}}$ =720 Hz).

Cy-*v*BRIDP Selenide

The general procedure for selenide formation was used to prepare this compound from Cy-*v*BRIDP (34). ^{31}P NMR (CDCl_3 , 202.2 MHz) δ 64.6 ppm ($^1J_{\text{P-Se}}$ =687 Hz).

Diethylphenyl phosphine selenide

The general procedure for selenide formation was used to prepare this compound from Diethylphenyl Phosphine (35). ^{31}P NMR (CDCl_3 , 202.2 MHz) δ 44.0 ppm ($^1J_{\text{P-Se}}$ =709 Hz).

Allyldiphenyl phosphine selenide

The general procedure for selenide formation was used to prepare this compound from Allyldiphenyl Phosphine (36). ^{31}P NMR (CDCl_3 , 202.2 MHz) δ 31.8 ppm ($^1J_{\text{P-Se}}$ =730 Hz).

iso-propyldiphenyl phosphine selenide

The general procedure for selenide formation was used to prepare this compound from *iso*-propyldiphenyl Phosphine (37). ^{31}P NMR (CDCl_3 , 202.2 MHz) δ 50.2 ppm ($^1J_{\text{P-se}} = 722$ Hz).

4-(Diphenylphosphino)styrene selenide

The general procedure for selenide formation was used to prepare this compound from 4-(Diphenylphosphino)styrene (38). ^{31}P NMR (CDCl_3 , 202.2 MHz) δ 34.7 ppm ($^1J_{\text{P-se}} = 729$ Hz).

Cyclic Voltammetry

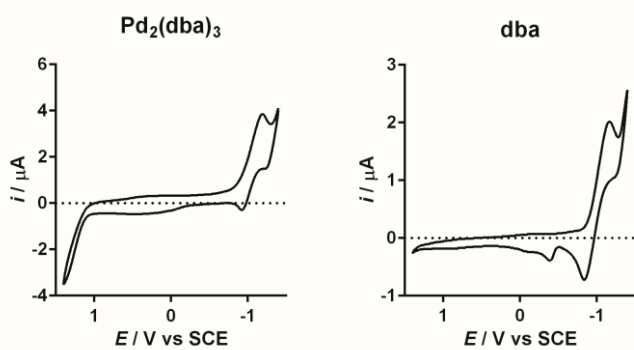
The procedure of Amatore, Jutand, and coworkers was followed with modifications.²⁰ A standard solution of Pd_2dba_3 ($[\text{Pd}] = 2$ mM) and tetrabutylammonium hexafluorophosphate (100 mM) in THF was prepared in a nitrogen purged glove box. Phosphines were weighed into 4 mL oven dried vials in the glove box, and 1 mL of THF was added ($[\text{Phosphine}] = 20$ mM). The Pd/salt standard solution was separated into 20 mL vials (10 mL in each vial) and capped with a rubber septum. Solutions were removed from the glove box and transferred to a 25 mL three necked flask using standard schlenk procedures. One neck was fitted with a rubber septum containing an SCE reference electrode and Pt mesh counter electrode. A second neck was fitted with a rubber septum containing a 2 mm gold working electrode. The final neck was fitted only with a septum. The phosphine solution was added in increments using a 500 μL syringe.

Cyclic voltammetry was performed using a CH Instruments DY2100B

potentiostat with a standard three-electrode cell. Cyclic voltammograms were measured at 50 mV sec^{-1} at $25 \text{ }^\circ\text{C}$. Pd_2dba_3 , dibenzylidene acetone, and the bis-ligated palladium species oxidation peaks were assigned based on a report by Amatore *et. al.*²⁰ and a pure Pd_2dba_3 solution. Table 2.10 includes the oxidation peak potentials for the cyclic voltammograms shown in Figure 2.12. Cyclic voltammograms of solutions of only $\text{Pd}_2(\text{dba})_3$ and only dba prepared under similar conditions are presented in Figure 2.14.

Table 2.10. Cyclic voltammetry studies.

Equiv Phosphine	E_{ipa} (V vs SCE)			
	PCy ₃	PEt ₃	PtBu ₃	SPhos
0.5	0.480	0.514	0.385	0.670
1	0.475	0.532	0.386	0.677
1.5	0.487	0.553	0.426	0.670
2	0.490	0.577	0.459	0.681
Equiv Phosphine	E_{ipa} (V vs SCE)			
	P <i>i</i> Pr ₃			
0.4	0.479			
1	0.514			
1.6	0.534			
2	0.546			

Figure 2.14. Cyclic voltammogram of Pd₂(dba)₃ and dba.

References

1. Golovin, M. N.; Rahman, M. M.; Belmonte, J. E.; Giering, W. P., Quantitative Separation of σ - and π -Components of Transition Metal-Phosphorus Bonding and the Application of Ligand Effects in Organometallic Chemistry. *Organometallics* **1985**, *4* (11), 1981-1991.
2. (a) Rahman, M. M.; Liu, H. Y.; Prock, A.; Giering, W. P., Quantitative Analysis of Ligand Effects. 2. Steric and Electronic Factors Influencing Transition-Metal-Phosphorus(III) Bonding. *Organometallics* **1987**, *6* (3), 650-658; (b) Woska, D.; Prock, A.; Giering, W. P., Determination of the Stereoelectronic Parameters of PF₃, PCl₃, PH₃, and P(CH₂CH₂CN)₃. The Quantitative Analysis of Ligand Effects (QALE). *Organometallics* **2000**, *19* (22), 4629-4638; (c) Wilson, M. R.; Woska, D. C.; Prock, A.; Giering, W. P., The Quantitative Analysis of Ligand Effects (QALE). The Aryl Effect. *Organometallics* **1993**, *12* (5), 1742-1752.
3. Fey, N.; Tsipis, A. C.; Harris, S. E.; Harvey, J. N.; Orpen, A. G.; Mansson, R. A., Development of a Ligand Knowledge Base, Part 1: Computational Descriptors for Phosphorus Donor Ligands. *Chem. Eur. J.* **2006**, *12* (1), 291-302.
4. Jover, J. s.; Fey, N.; Harvey, J. N.; Lloyd-Jones, G. C.; Orpen, A. G.; Owen-Smith, G. J. J.; Murray, P.; Hose, D. R. J.; Osborne, R.; Purdie, M., Expansion of the Ligand Knowledge Base for Monodentate P-Donor Ligands (LKB-P)†. *Organometallics* **2010**, *29* (23), 6245-6258.
5. Milo, A.; Bess, E. N.; Sigman, M. S., Interrogating Selectivity in Catalysis Using Molecular Vibrations. *Nature* **2014**, *507* (7491), 210-214.
6. Tolman, C. A., Steric Effects of Phosphorus Ligands in Organometallic Chemistry and Homogeneous Catalysis. *Chem. Rev.* **1977**, *77* (3), 313-348.
7. Littke, A. F.; Dai, C.; Fu, G. C., Versatile Catalysts for the Suzuki Cross-Coupling of Arylboronic Acids with Aryl and Vinyl Halides and Triflates under Mild Conditions. *J. Am. Chem. Soc.* **2000**, *122* (17), 4020-4028.
8. Schoenebeck, F.; Houk, K. N., Ligand-Controlled Regioselectivity in Palladium-Catalyzed Cross Coupling Reactions. *J. Am. Chem. Soc.* **2010**, *132* (8), 2496-2497.
9. Barrios-Landeros, F.; Carrow, B. P.; Hartwig, J. F., Effect of Ligand Steric Properties and Halide Identity on the Mechanism for Oxidative Addition of Haloarenes to Trialkylphosphine Pd(0) Complexes. *J. Am. Chem. Soc.* **2009**, *131* (23), 8141-8154.
10. Bickelhaupt, F. M., Understanding Reactivity with Kohn–Sham molecular Orbital Theory: E2–SN2 Mechanistic Spectrum and Other Concepts. *J. Comput. Chem.* **1999**, *20* (1), 114-128.

11. Bickelhaupt, F. M.; Houk, K. N., Analyzing Reaction Rates with the Distortion/Interaction-Activation Strain Model. *Angew. Chem. Int. Ed.* **2017**, *56* (34), 10070-10086.
12. Proutiere, F.; Lyngvi, E.; Aufiero, M.; Sanhueza, I. A.; Schoenebeck, F., Combining the Reactivity Properties of PCy₃ and PtBu₃ into a Single Ligand, P(iPr)(tBu)₂. Reaction via Mono- or Bisphosphine Palladium(0) Centers and Palladium(I) Dimer Formation. *Organometallics* **2014**, *33* (23), 6879-6884.
13. Lyngvi, E.; Sanhueza, I. A.; Schoenebeck, F., Dispersion Makes the Difference: Bisligated Transition States Found for the Oxidative Addition of Pd(PtBu₃)₂ to Ar-OSO₂R and Dispersion-Controlled Chemoselectivity in Reactions with Pd[P(iPr)(tBu)₂]₂. *Organometallics* **2015**, *34* (5), 805-812.
14. Barder, T. E.; Walker, S. D.; Martinelli, J. R.; Buchwald, S. L., Catalysts for Suzuki–Miyaura Coupling Processes: Scope and Studies of the Effect of Ligand Structure. *J. Am. Chem. Soc.* **2005**, *127* (13), 4685-4696.
15. Guzei, I. A.; Wendt, M., An Improved Method for the Computation of Ligand Steric Effects Based on Solid Angles. *Dalton Trans.* **2006**, (33), 3991-3999.
16. Tolman, C. A., Phosphorus Ligand Exchange Equilibria on Zerovalent Nickel. Dominant Role for Steric Effects. *J. Am. Chem. Soc.* **1970**, *92* (10), 2956-2965.
17. (a) Verloop, A., *Drug Design Vol. III*. Academic Press: 1976; p 133; (b) Harper, K. C.; Bess, E. N.; Sigman, M. S., Multidimensional Steric Parameters in the Analysis of Asymmetric Catalytic Reactions. *Nat. Chem.* **2012**, *4* (5), 366-374.
18. (a) Allen, D. W.; Taylor, B. F., The Chemistry of Heteroarylphosphorus Compounds. Part 15. Phosphorus-31 Nuclear Magnetic Resonance Studies of the Donor Properties of Heteroarylphosphines Towards Selenium and Platinum(II). *J. Chem. Soc., Dalton Trans.* **1982**, (1), 51-54; (b) McAtee, J. R.; Yap, G. P.; Watson, D. A., Rational Design of a Second Generation Catalyst for Preparation of Allylsilanes Using the Silyl-Heck Reaction. *J. Am. Chem. Soc.* **2014**, *136* (28), 10166-72.
19. Kuhn, M.; Johnson, K., *Applied Predictive Modeling*. Springer: 2013.
20. Amatore, C.; Jutand, A.; Khalil, F.; M'Barki, M. A.; Mottier, L., Rates and Mechanisms of Oxidative Addition to Zerovalent Palladium Complexes Generated in situ From Mixtures of Pd⁰(dba)₂ and Triphenylphosphine. *Organometallics* **1993**, *12* (8), 3168-3178.
21. Hartwig, J. F.; Paul, F., Oxidative Addition of Aryl Bromide after Dissociation of Phosphine from a Two-Coordinate Palladium(0) Complex, Bis(tri-*o*-tolylphosphine)Palladium(0). *J. Am. Chem. Soc.* **1995**, *117* (19), 5373-5374.

22. Surry, D. S.; Buchwald, S. L., Dialkylbiaryl Phosphines in Pd-Catalyzed Amination: A User's Guide. *Chem. Sci.* **2011**, *2* (1), 27-50.
23. Barder, T. E.; Buchwald, S. L., Insights into Amine Binding to Biaryl Phosphine Palladium Oxidative Addition Complexes and Reductive Elimination from Biaryl Phosphine Arylpalladium Amido Complexes via Density Functional Theory. *J. Am. Chem. Soc.* **2007**, *129* (39), 12003-12010.
24. (a) McFarlane, W.; Rycroft, D. S., Studies of Organophosphorus Selenides by Heteronuclear Magnetic Triple Resonance. *J. Chem. Soc., Dalton Trans.* **1973**, (20), 2162-2166; (b) Allen, D. W.; Nowell, I. W.; Taylor, B. F., The Chemistry of Heteroarylphosphorus Compounds. Part 16. Unusual Substituent Effects on Selenium-77 Nuclear Magnetic Resonance Chemical Shifts of Heteroaryl- and Aryl-Phosphine Selenides. X-Ray Crystal Structure of Tri(2-furyl)phosphine Selenide. *J. Chem. Soc., Dalton Trans.* **1985**, (12), 2505-2508.
25. Creary, X.; Benage, B.; Hilton, K., Reaction of Triflates with Potassium Diethyl Phosphite. Formation of Phosphate Esters. *J. Org. Chem.* **1983**, *48* (17), 2887-2891.
26. Zalesskiy, S. S.; Ananikov, V. P., Pd₂(dba)₃ as a Precursor of Soluble Metal Complexes and Nanoparticles: Determination of Palladium Active Species for Catalysis and Synthesis. *Organometallics* **2012**, *31* (6), 2302-2309.
27. *Schrödinger Release 2014-3: MacroModel*, version 10.5; Schrödinger, LLC: New York, NY, 2014.
28. Frisch, M. J.; Trucks, G. W.; Schlegel, H. B.; Scuseria, G. E.; Robb, M. A.; Cheeseman, J. R.; Scalmani, G.; Barone, V.; Mennucci, B.; Petersson, G. A.; Nakatsuji, H.; Caricato, M. L.; Hratchian, H. P.; Izmaylov, A. F.; Bloino, J.; Zheng, G.; Sonnenberg, J. L.; Hada, M.; Ehara, M.; Toyota, K.; Fukuda, R.; Hasegawa, J.; Ishida, M.; Nakajima, T.; Honda, Y.; Kitao, O.; Nakai, H.; Vreven, T.; Montgomery, J. A., Jr.; Peralta, J. E.; Ogliaro, F.; Bearpark, M.; Heyd, J. J.; Brothers, E.; Kudin, K. N.; Staroverov, V. N.; Kobayashi, R.; Normand, J.; Raghavachari, K.; Rendell, A.; Burant, J. C.; Iyengar, S. S.; Tomasi, J.; Cossi, M.; Rega, N.; Millam, N. J.; Klene, M.; Knox, J. E.; Cross, J. B.; Bakken, V.; Adamo, C.; Jaramillo, J.; Gomperts, R.; Stratmann, R. E.; Yazyev, O.; Austin, A. J.; Cammi, R.; Pomelli, C.; Ochterski, J. W.; Martin, R. L.; Morokuma, K.; Zakrzewski, V. G.; Voth, G. A.; Salvador, P.; Dannenberg, J. J.; Dapprich, S.; Daniels, A. D.; Farkas, Ö.; Foresman, J. B.; Ortiz, J. V.; Cioslowski, J.; Fox, D. J. *Gaussian 09, Revision D.01*, Gaussian, Inc.: Wallingford, CT, 2009.
29. Zhao, Y.; Truhlar, D., The M06 Suite of Density Functionals for Main Group Thermochemistry, Thermochemical Kinetics, Noncovalent Interactions, Excited States, and Transition Elements: Two New Functionals and Systematic Testing of Four M06-Class Functionals and 12 Other Functionals. *Theor. Chem. Acc.* **2008**, *120* (1-3), 215-241.

30. Guzei, I. A.; Wendt, M., An Improved Method for the Computation of Ligand Steric Effects Based on Solid Angles. *Dalton Trans.* **2006**, (33), 3991-9.
31. Weigend, F.; Ahlrichs, R., Balanced Basis sets of Split Valence, Triple Zeta Valence and Quadruple Zeta Valence Quality for H to Rn: Design and Assessment of Accuracy. *PCCP* **2005**, 7 (18), 3297-3305.
32. Merrick, J. P.; Moran, D.; Radom, L., An Evaluation of Harmonic Vibrational Frequency Scale Factors. *J. Phys. Chem. A* **2007**, 111 (45), 11683-11700.
33. Quinn, J. A. *Molecular Modeling Pro*, 6.36; Norgwyn Montgomery Software Inc.: North Wales, PA

CHAPTER 3

MECHANISTIC INTERROGATION OF THREE REACTIONS USING NEWLY DEVELOPED PHOSPHINE PARAMETERS

Following the successful application of our recently established phosphine parameters, we sought to apply these to a more challenging system. We initiated two collaborative projects directed at probing two distinct questions. The first, a study of two similar gold phosphine catalyzed reactions, asked if our new parameters could be applied to probe non-palladium organometallic reactions. The role of phosphines in these systems was distinctly different from the palladium system tested in Chapter 2, which tested our system. This study was completed in collaboration with Alec Christian of the Toste lab. The second case study returned to palladium catalysis in an alkyl Suzuki coupling. However, the mechanism was much less well understood, and the alkyl chain inherently induced additional challenges compared to the biaryl coupling presented in Chapter 2. All synthetic chemistry was performed by Shibin Zhao of the Biscoe lab. These two case studies are presented in this chapter.

Ligand Effects in Gold-Catalyzed Cycloisomerization Reactions

Introduction

Homogeneous gold catalysis has witnessed rapid growth over the previous fifteen years, spurred in part by the Toste group,¹ along with multiple other groups.² Conditions for numerous cyclization reactions³ and rearrangements⁴ have been described, including differential reactivity induced by ligand choice.⁵ Multiple mechanistic studies have expanded our knowledge of how gold(I) reactions proceed.⁶ Central to this expansion in synthesis and understanding has been the appropriate choice of ligand,⁷ built on the unique linear bonding geometry of gold(I) complexes (Figure 3.1).⁸ To further advance this field, we elected to study the role of phosphine ligands in two cyclization reactions. The necessity of this study is exemplified in a report from the Hammond and Xu groups.^{7b} They state that the Buchwald class of phosphine ligands engages in a possible weak interaction between the aryl ring and gold, stabilizing the gold complex. However, work from the Echavarren group contests this claim, as the “gold–arene distance is longer than the maximum estimated for a meaningful metal–arene interaction.”⁹ The continued confusion of the role the phosphine plays in gold catalysis provided ample impetus for our group to engage in a detailed mechanistic study with the Toste team.

Background

One reaction that shows particularly interesting ligand controlled reactivity is the cycloisomerization reaction depicted in Figure 3.2.¹⁰ Reported initially in 2009, this reaction was initially hypothesized to occur through a bifurcative concerted cyclization. This mechanism would furnish either a seven- or six-membered ring, followed by loss of

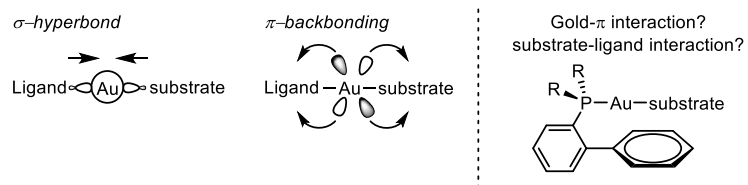


Figure 3.1. Bonding model developed by Goddard, Toste, and coworkers depicting a linear geometry about the gold atom. Buchwald class phosphines engender multiple possible influences on selective reactions.

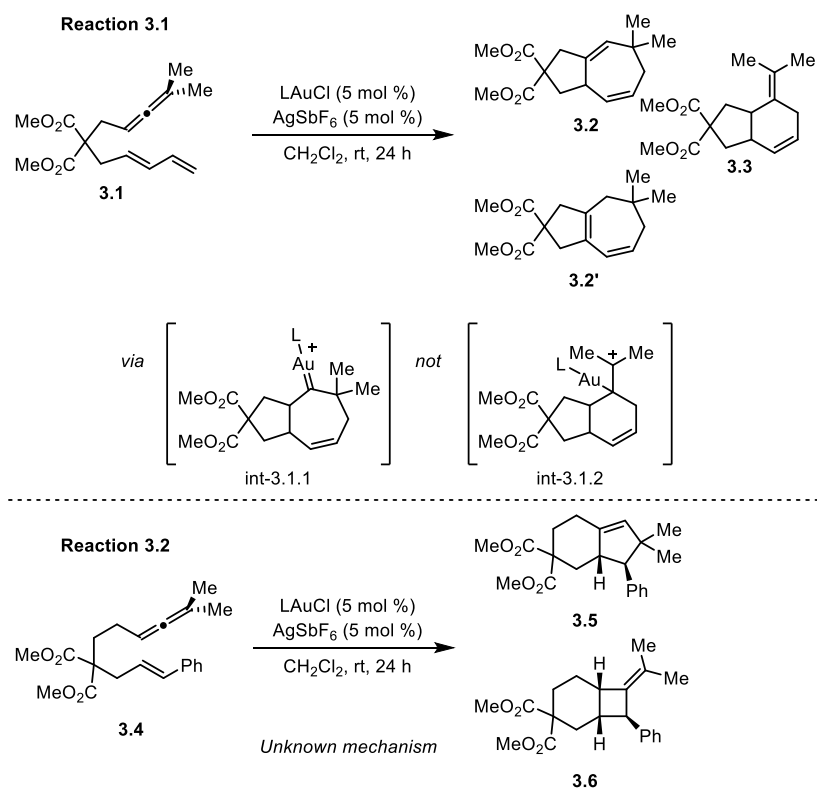


Figure 3.2. Two cycloisomerization reactions probed mechanistically.

gold. The Toste team hypothesized that the sequence to the seven-membered ring would be stabilized by more electron-rich ligands, and this was confirmed when the electron donating Johnphos ligand was used. Conversely, this pathway was hypothesized to be destabilized through the use of strongly π -accepting ligands. The use of phosphites yielded exclusive formation of the [4+2] product **3.3**, validating the authors' hypothesis. However, a rapid follow-up paper from the Toste and Goddard labs contested this analysis through the use of DFT calculations.¹¹ The transition state pathway containing a concerted [4+2] cyclization (**int-3.1.2**) was calculated to be prohibitively high using PMe_3 as the ligand, being 13.9 kcal/mol higher in energy than formation of the [4+3] gold intermediate (**int-3.1.1**). Instead, the authors suggested that either a 1,2 hydrogen or carbon shift would lead to the products from this same intermediate. Further calculations with JohnPhos and triphenylphosphite confirmed this likely bifurcation point. Using JohnPhos, the [4+3] cycloaddition pathway was again identified, and the alkyl or hydrogen shift pathways were probed. The carbon shift pathway was higher in energy (6.1 kcal/mol to product **3.3**) than the hydrogen shift (2.6 kcal/mol to product **3.2** and **3.2'**), in agreement with experiment, and this effect was attributed to the steric interactions between the ligand and substrate. Thus, the authors argue that larger ligands distort the organometallic gold intermediate geometry, resulting in poor back-donation from the gold to the carbon π -orbital and allowing the facile 1,2-hydrogen shift to occur. The 1,2-alkyl shift is calculated to be unaffected by this change. Overall, the argument that steric interactions control selectivity is generally in agreement with the outcomes from the limited reported ligand screen.

In comparison to reaction 3.1, the second reaction displays striking similarities

(Figure 3.2). For example, the two reactions occur under identical conditions. In the first reaction, both [4+3] and [4+2] products are isolated, and the second reaction yields the [2+2] (**3.6**) and [2+3] (**3.5**) products. However, drastically different ligand effects were identified, prompting us to question the role of the ligand in possibly altering the mechanism. In order to better understand the similarities and differences between these two reactions, a mechanistic study was initiated integrating classic physical organic tools with our newly developed parameters. Specifically, we sought to determine subtle ligand effects that influence reaction selectivity, and to leverage these effects into greater understanding of the role of phosphine ligands in gold(I) catalysis.

Results and Discussion: [4+3] versus [4+2] Cycloisomerization

To initiate our studies, we first sought to define a general mechanism for the [4+3]/[4+2] cycloisomerization reaction. Deutero **3.1** was submitted to the reaction conditions and compared to the proteo variant (Figure 3.3). A significant difference in product ratios was observed wherein deutero **3.1** resulted in a 4.4:1 product ratio whereas proteo **1** yielded a 6.2:1 ratio of (**3.2+3.2'**)/**3.3**, confirming that C–H(D) bond cleavage is involved in the selectivity determining step. These results are consistent with the previously proposed computational mechanism in which either a 1,2-hydride or alkyl shift occurs.

Having gained preliminary evidence for the previously proposed cycloisomerization mechanism, we turned our attention to the ligand effects. Product ratios were quantified for 15 ligands, revealing a number of interesting trends (Figure 3.4). A large range was observed including instances when either the 6 or 7-membered

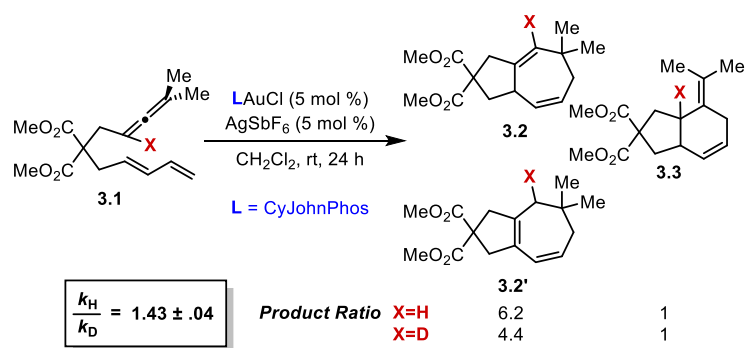


Figure 3.3. Isotope labeling revealed a significant change in reaction selectivity based on the choice of deuterio- or proteo-substrate **3.1**.

Entry	Ligand	Yield (%) ^a	Ratio (3.3:3.2+3.2')	$\Delta\Delta G^\ddagger$ (kcal/mol)	Au-Cl dist. (Å)
1	P(<i>p</i> -OMePh) ₃ ^b	79	1.9:1	-0.39	2.319
2	P(<i>o</i> -OMePh) ₃ ^b	54	1:2.2	0.48	2.329
3	P <i>p</i> -Tol ₃ ^b	82	1.9:1	-0.39	2.312
4	P <i>o</i> -Tol ₃ ^b	75	2.1:1	-0.44	2.320
5	P(<i>p</i> -FPh) ₃ ^b	87	3.3:1	-0.71	2.311
6	PMe ₃ ^b	50	1.8:1	-0.44	2.309
7	PEt ₃ ^b	64	1.3:1	-0.14	2.318
8	P(ArO) ₃ ^{c,e}	89	9.5:1	-1.33	2.300
9	cBRIDP	81	1:5.1	0.96	2.332
10	Cy-cBRIDP	88	1:4.2	0.85	2.330
11	JohnPhos	88	1:14	1.55	2.329
12	CyJohnPhos	89	1:6.2	1.08	2.327
13	SPhos	85	1:15	1.61	2.338
14	RuPhos	94 ^d	1:23	1.85	2.335
15	XPhos	62	1:9	1.30	2.331

^aYield determined by ¹H NMR using 1,4-dinitrobenzene as an internal standard. ^bReaction stopped at 1 h. ^cReaction stopped at 30 min.

^dIsolated yield ^eAr = 2,4-di-*t*Bu-Ph

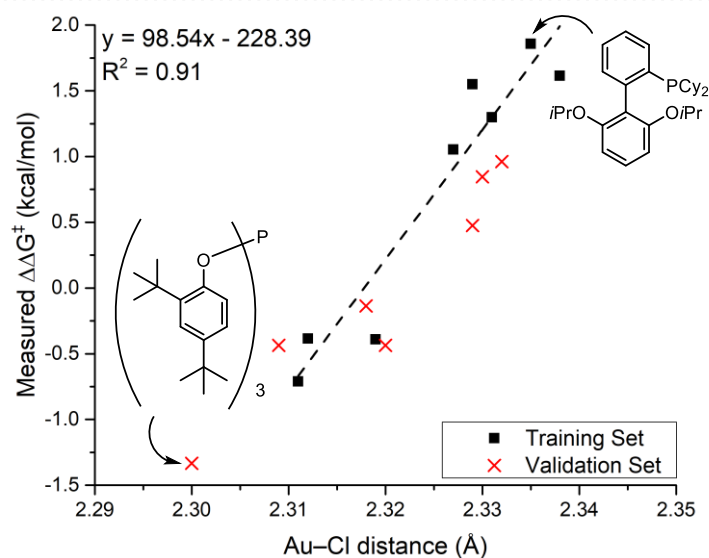
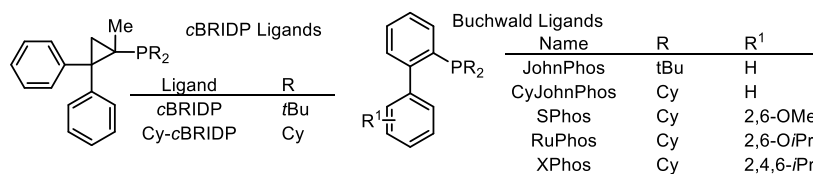


Figure 3.4. Reaction 1 selectivities correlated to the Au-Cl distance.

ring was preferred (-0.71 kcal/mol to 1.85 kcal/mol, more positive energies indicate increased formation of the seven membered ring products **3.2** or **3.2'**). Initial inspection of these results allows for the delineation of two classes of ligands: The Buchwald-type, BRIDP ligands, and P(*o*-OMePh)₃ each preferentially form products **3.2** or **3.2'** (entries 2, 9-15), whereas alkyl and other aryl phosphines result in the formation of product **3.3** (1, 3-8). As both the Buchwald and BRIDP class of ligands were developed to block two coordination sites in palladium chemistry,¹² this bifurcation could plausibly implicate a steric interaction; however, this analysis is complicated by the large, sterically bulky P*o*-Tol₃ (entry 1) which preferentially forms product **3.3**. This discrepancy prompted a deeper investigation into how the ancillary phosphine ligand interacts with the substrate to induce chemoselectivity.

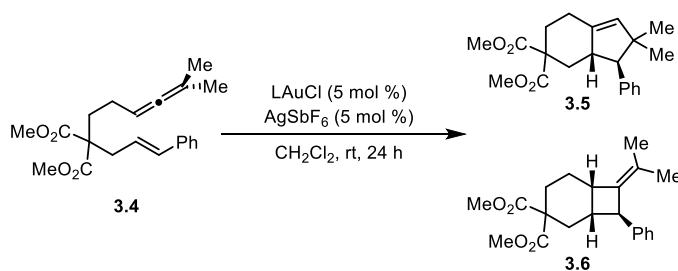
As the relationship between ligand and selectivity was not immediately apparent, we sought quantitative correlations between product selectivity and reported parameters. An optimal correlation was identified between the Au–Cl distance and the reaction selectivities ($R^2 = 0.91$). Fey and coworkers characterize this parameter as being related to both steric interactions and the phosphine σ -donor ability based on the relationships to other parameters within their set.¹³ Indeed, both of these considerations would affect the Au–Cl bond distance based on the bonding model presented above. Therefore, it is plausible that both steric and electronic trends are captured in this parameter, and these interact with the substrate to produce the reaction selectivity. Thus, this analysis supports the computationally proposed model in which the gold-carbenoid bond is altered via both steric and electronic influences from the ligand. This change induces selectivity determining 1,2-hydride or alkyl shift, wherein the overall selectivity is primarily dictated

by the ability of the intermediate to undergo the 1,2-hydride shift.¹¹

Results and Discussion: [2+3] versus [2+2] Cycloisomerization

The simplistic analysis of reaction 1 prompted us to consider the universality of the conclusions presented above to other gold-catalyzed cyclization reactions. Due to the similarities between reactions 1 and 2, we hypothesized that similar interactions would determine selectivity. The Toste lab had previously reported that this reaction, when performed with JohnPhosAuCl, resulted in products **3.5** and **3.6** being formed in a 6.8:1 ratio. This result indicated that ligand effects in this reaction could be isolated and examined under a similar protocol.

A similar data set was collected to examine the structure-selectivity relationships for the [2+3]/[2+2] cycloisomerization (Figure 3.5). All ligands tested resulted in the preferential formation of the larger ring product **3.5**, in contrast to reaction 1 (Figure 3.2) in which both ring sizes could be preferentially formed. If similar interactions were determining selectivity, we hypothesized that the Au-Cl bond distance would again correlate to the overall selectivity. However, this was not observed, resulting in a re-evaluation of which factors are inducing selectivity. Univariate correlations were again illuminating, wherein the average Sterimol L/B_1 correlated to overall selectivity (Figure 3.6). As this parameter describes the three-dimensional shape of the ligand, it likely describes the “depth” of the ligand compared to the steric hindrance proximal to the gold center. Specifically, B_1 quantifies the local steric bulk, and thus likely would influence how the substrate can approach the gold. Conversely, L measures the ligand length, possibly describing direct interactions between the ligand and substrate.



Entry	Ligand	Yield (%) ^a	Ratio (3.5:3.6)	$\Delta\Delta G^\ddagger$ (kcal/mol)	L/B ₁ average
1	P(<i>p</i> -OMePh) ₃ ^b	92	1.5:1	0.22	1.25
2	P <i>p</i> -Tol ₃ ^b	91	1.5:1	0.22	1.17
3	P(<i>p</i> -FPh) ₃ ^b	89	1.2:1	0.10	1.37
4	PMe ₃ ^c	67	1.5:1	0.25	1.47
5	<i>t</i> Bu ₃	89	2.4:1	0.51	1.32
6	cBRIDP	30	5.4:1	1.00	1.81
7	Cy-cBRIDP	56	3.3:1	0.75	1.48
8	JohnPhos	65	6.8:1	1.14	1.94
9	CyJohnPhos	59	2.4:1	0.53	1.78
10	SPhos	16	2.7:1	0.59	1.79
11	RuPhos	11	2.7:1	0.59	1.58
12	XPhos	15	13:1	1.54	2.20
13	<i>t</i> BuXPhos	24(71) ^d	26:1	1.93	2.47

^aYield determined by ¹H NMR using 1,4-dinitrobenzene as an internal standard. ^bReaction stopped at 1 h. ^cReaction stopped at 30 min.

^dIsolated yield after 96 h

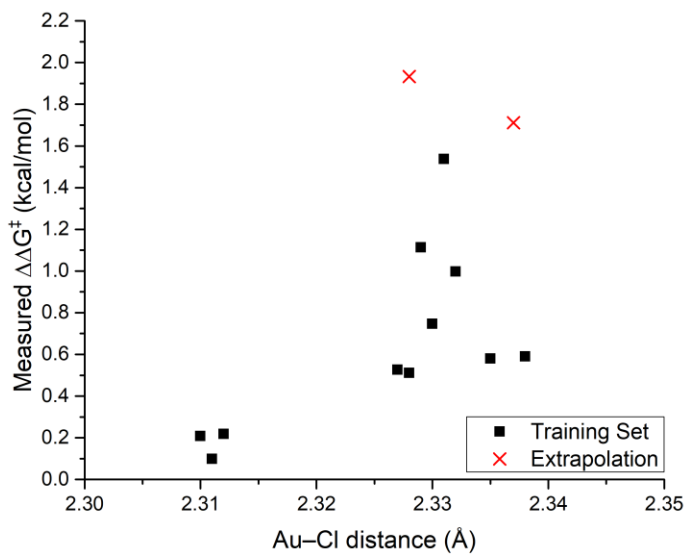


Figure 3.5. Results from reaction 2 screening and relationship to Au-Cl distance.

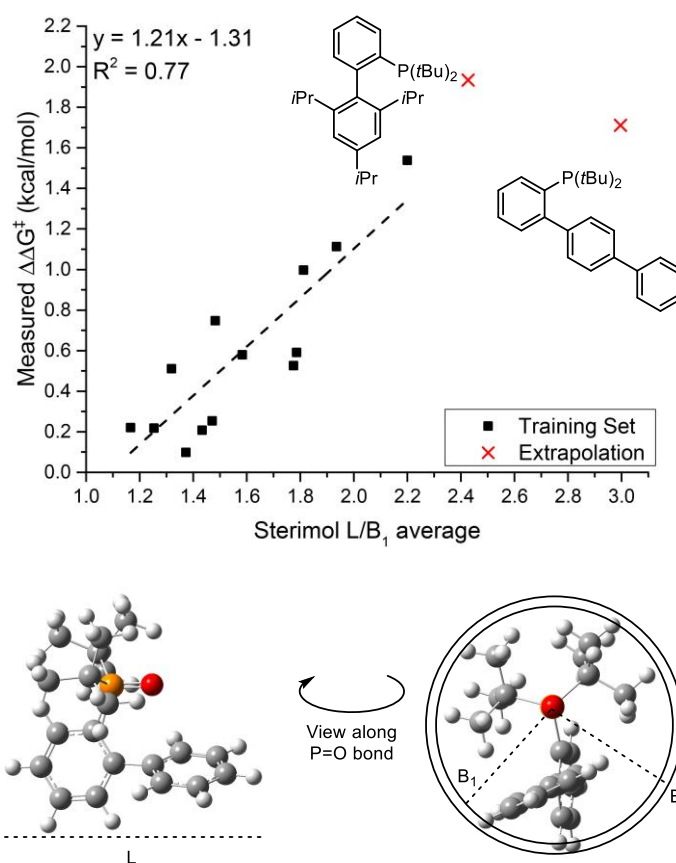


Figure 3.6. Reaction 2 selectivities correlated to the average Sterimol L/B_1 , including two extrapolation points.

On the basis of this correlation, we hypothesized that a change in mechanism may have occurred, and thus four plausible scenarios were considered (Figure 3.7). First, analogous to reaction 3.1, a concerted cyclization could be followed by a ligand induced 1,2-hydride or alkyl shift. Second, a direct concerted cyclization could result in either a 4- or 5-membered ring. Contrasting these two mechanisms, each cyclization could occur through a stepwise fashion, with a stabilized benzylic carbocation intermediate. From this intermediate, cyclization to a 5-membered ring could be followed by a selectivity determining hydride or alkyl shift. Finally, the same carbocation intermediate could directly cyclize to a 4- or 5-membered ring. To identify the likely mechanistic manifold, classic physical organic tools were employed.

Two experiments were used to differentiate between the proposed mechanisms (Figure 3.8). Similar to reaction 3.1, isotopic labeling was used to determine the role of C–H bond cleavage. In contrast, little to no kinetic isotope effect was observed, suggesting that 1,2-hydride shift does not play a role in the selectivity determining step and eliminating mechanisms 1 and 3 from consideration. Next, we turned our attention to differentiating between mechanisms 2 and 4. As the concerted versus stepwise mechanisms differ via the formation of a cationic intermediate, a Hammett analysis was employed. If a stepwise mechanism was operative, we hypothesized that a linear relationship would be identified between the relative rates and σ_{para}^+ . However, the relative rates correlated to σ_{para} with a slope of -3.65. These data suggest that a distinct carbocation intermediate is not formed, and that a concerted cyclization occurs with significant positive charge accumulating on the benzylic carbon. Thus, our data suggest that a selectivity determining cyclization occurs from a gold-coordinated substrate

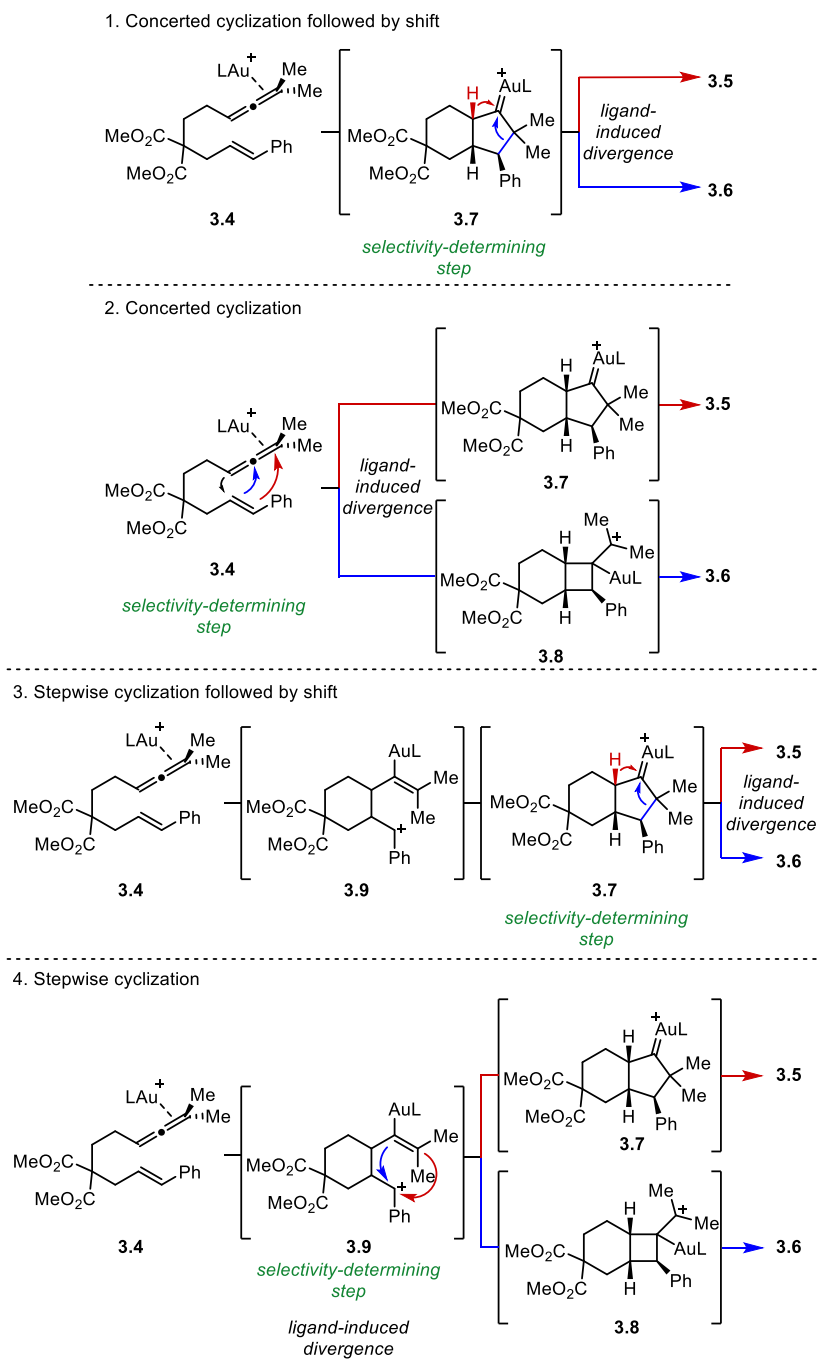


Figure 3.7. Plausible mechanistic proposals considered.

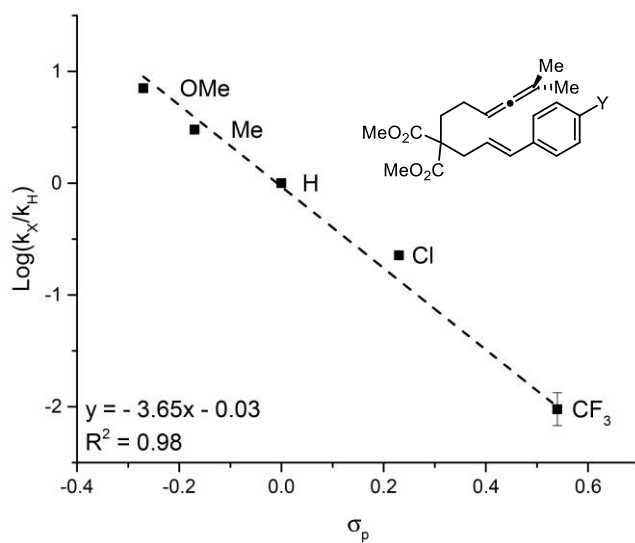
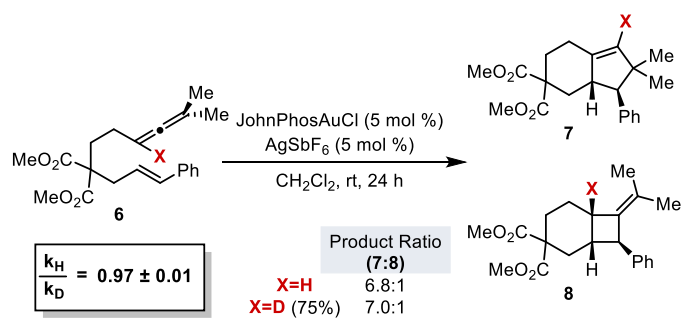


Figure 3.8. Deuterium labeling and Hammett study results.

(mechanism 2).

Having gained a better understanding of the mechanism of reaction 3.2, we returned to the identified correlation between reaction selectivity and Sterimol L/B1. Virtual screening of ligand scaffolds commenced to improve reaction selectivity. Two pathways were hypothesized to increase selectivity: B₁ could be decreased by exchanging the cyclohexyl rings for smaller groups within XPhos, or L could be increased via extension of the biaryl ring in JohnPhos. As an example of the former, tBuXPhos was examined and resulted in a product ratio of 26:1 ($\Delta\Delta G^\ddagger = 1.93$ kcal/mol), slightly higher than predicted (17:1, $\Delta\Delta G^\ddagger = 1.68$ kcal/mol) favoring product 5. To interrogate the latter possibility, a novel ligand containing a triphenyl group was synthesized and predicted to produce a 31:1 product ratio ($\Delta\Delta G^\ddagger = 1.68$ kcal/mol). The observed selectivity of 17:1 ($\Delta\Delta G^\ddagger = 1.68$ kcal/mol) is lower than expected; however, this ratio is within the expected range of predictions and higher than any ligand within the training set. These two extrapolations demonstrate the power of small data sets to yield non-intuitive results.

Conclusions

Overall, two gold(I) catalyzed reactions were interrogated using a combination of classical physical organic experiments and modern data analysis tools. These results provide detail insight into the relationship between ligand structure and reaction selectivity in gold(I)-phosphine catalyzed cycloisomerization reactions. Initial studies of a [4+3]/[4+2] cycloisomerization reaction resulted in the hypothesis that the ligand's effect on the gold-substrate bond length was a key factor in selectivity determining 1,2-hydride or alkyl shifts. In contrast, analysis of the [2+3]/[2+2] cyclization reaction

resulted in a correlation between the product ratio and the ligand size, as quantified by L/B_1 . The confounding role of these two highly similar reactions demonstrates the aptitude of utilizing this methodology in future gold(I) catalysis studies.

Interrogating Alkyl-Aryl Suzuki Reaction Pathways

Following the successful application of our phosphine parameters to interrogate gold(I) catalyzed cyclizations, we returned our attention to the palladium-catalyzed Suzuki reaction. Recent work from the Biscoe group had identified conditions to use configurationally stable alkyl boron reagents with aryl halides to yield the alkyl-aryl cross-coupling products with conservation of the stereochemical integrity. However, the mechanism by which the stereospecific process occurs and how to influence these pathways has been disputed, including the role of the phosphine ligand. Therefore, a collaborative study, performed with Shibin Zhao of the Biscoe lab sought to refine the governing features in order to enhance the utility of this reaction.

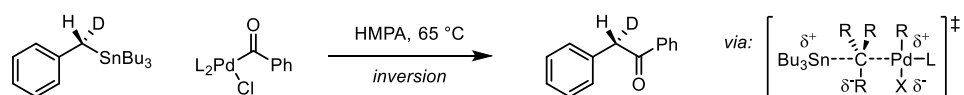
Introduction

Cross-coupling technology such as the Suzuki reaction has revolutionized how synthetic chemists construct complex molecules. Classic studies have focused on $C(sp^2)$ - $C(sp^2)$ methodologies, enabling the modular construction of planar bonds. However, the use of $C(sp^3)$ coupling partners remains a challenge as multiple transmetallation pathways are viable and β -hydride elimination can occur from the alkyl ligands.¹⁴ Thus, relatively few examples of stereospecific alkyl-aryl couplings have been reported.¹⁵ Recent work from the Biscoe group has focused on the use of enantio-enriched

orgaonometallic nucelophiles,^{15h, 16} including alkyl-boron reagents,¹⁵ⁱ as a promising route to yield the desired C(sp²)-C(sp³) coupling. To facilitate the further development of this desirable reaction class, mechanistic studies of the reaction manifold commenced. The goals of this project were to simultaneously identify and avoid possible deleterious pathways and to enhance the preferred catalytic process.

Key to the successful application of an alkyl-aryl Suzuki reaction is regulation of the transmetallation step; current mechanistic proposals have been informed by foundational studies of the Stille reaction.¹⁷ Two early publications display the divergent stereoselection due to the presumed bifurcative pathways (Figure 3.9). First, Labadie and Stille studied the palladium catalyzed coupling of acid chlorides with organotin reagents, including the enantio-enriched α -deuteriobenzyl tributyltin.¹⁸ The reaction of this substrate in the presence of palladium benzoyl chloride in hexamethylphosphoramide (HMPA) resulted in the formation of the desired cross coupling product with inversion of stereochemistry (reaction 3.3). This result was attributed to an open transition state, stabilized by the polar solvent, involving invertive transfer of the benzyl group from tin to palladium. Secondly, Falck and coworkers analyzed a similar Stille reaction using [α -benzoyloxy)octyl]tributylstannane with benzoyl chloride in the presence of palladium and copper in toluene (reaction 3.4).¹⁹ This coupling proceeded with retention of stereochemistry, contrary to Stille's original publication. Under nonpolar solvent conditions, the reaction is hypothesized to proceed through a cyclic 4-membered transition state that limits charge separation. These opposing stereochemical outcomes and mechanisms were further established by Espinet and coworkers,²⁰ and similar pathways are hypothesized to be operative with alkyl boron reagents. In sum, either an

Stille 1983 (Reaction 3.3)



Falck 1994 (Reaction 3.4)

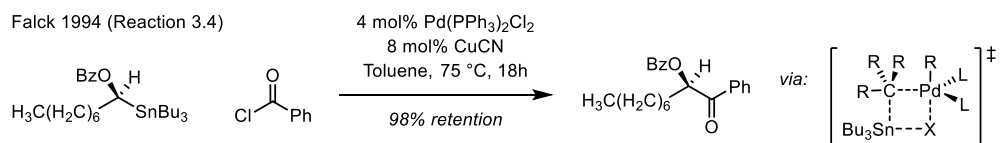


Figure 3.9. Open and cyclic transition states result in invertive and retentive transmetalation steps, respectively.

open or cyclic transition state can be favored based on the reaction conditions and regulation of the energetics of these processes is paramount to produce a synthetically valuable reaction.

To shed light on the regulatory interactions within the alkyl-aryl Suzuki reaction, we elected to build upon a recently developed chemical method from the Biscoe lab (Reaction 3.5, Figure 3.10). This reaction utilizes readily available aryl halides with configurationally stable alkyl trifluoroborate potassium salts. Activation of the borate salt occurs in the presence of water, resulting in the formation of a boronic acid.²¹ Additionally, the palladium(II) precatalyst can be reduced to palladium(0) in the presence of base.²² Following activation, the desired reaction pathway involves three fundamental organometallic steps. First, oxidative addition of the palladium to the aryl chloride has been shown to be facile with the appropriate ligand.²³ This intermediate can undergo stereo-retentive or invertive transmetallation with the alkyl boronic acid, followed by bond forming reductive elimination. However, if the reductive elimination is slow, β -hydride elimination can occur once the alkyl chain is bound to the palladium. Understanding how to avoid the β -hydride elimination pathway, while simultaneously controlling the transmetallation mechanism, served as the dual goals of this study.

Results and Discussion

To isolate the preferred transmetalation from substrate steric interactions, we initiated our study using enantio-enriched potassium *sec*-butyl trifluoroborate (99:1 enantiomeric ratio, er) as the nucleophile (Figure 3.11). An initial array of 22 phosphine ligands revealed both highly and poorly selective catalysis, including a range from

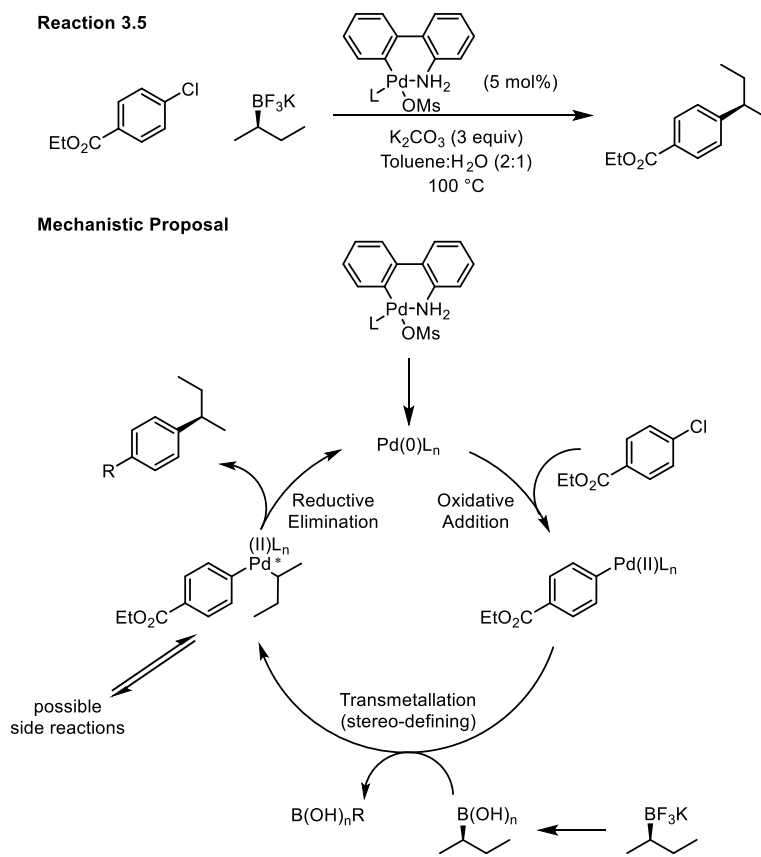


Figure 3.10. Alkyl-aryl Suzuki reaction developed by Biscoe and coworkers.

Entry	Ligand	ee (%)	$\Delta\Delta G^\ddagger$ (kcal/mol)	^{31}P (δ)	Min Cone ($^\circ$)
1	XPhos	11	0.13	-12.0	209.8
2*	CPhos	10	0.12	-8.6	206.4
3	SPhos	23	0.27	-8.4	201.9
4	RuPhos	14	0.17	-8.5	187.5
5	CyJohnPhos	7	0.08	-12.6	183.6
6	P(1-Ad) ₃	-93	-1.97	59.4	178.0
7	PhSPhos	56	0.76	-11.6	173.3
8	PtBu ₃	-80	-1.29	61.1	153.2
9	Po-Tol ₃	64	0.89	-30.5	146.7
10	PnBu(1-Ad) ₂	5	0.05	26.6	145.3
11	PCy ₃	4	0.05	7	144.7
12	PneoptBu ₂	-68	-0.98	19.8	144.6
13	PtBuPh ₂	23	0.28	19.1	142.4
14	PMe ₂ Bu ₂	2	0.02	11.0	138.4
15	P(o-OMePh) ₃	16	0.19	-37.1	136.6
16	P(p-CF ₃ Ph) ₃	13	0.15	-13.7	131.5
17	PPh ₃	11	0.13	-4.7	131.4
18	Pp-Tol ₃	12	0.14	-8.0	131.1
19	PPh ₂ Bn	10	0.12	-10.4	125.3
20	PnBu ₃	6	0.07	-32.3	124.6
21	PEt ₃	9	0.11	-20.4	121.5
22	PMe ₃	6	0.07	-62.0	109.6

*external validation

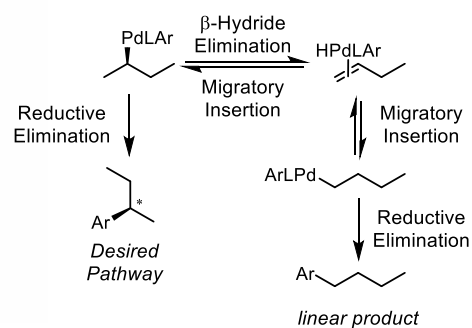
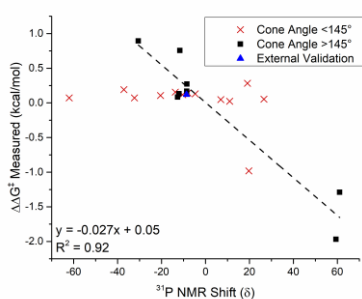


Figure 3.11. Reaction 3.5 ligand selectivity trends.

3.5:96.5 (-95% enantiospecificity, ee , calculated as $ee_{\text{product}}/ee_{\text{starting material}}*100$, triadamantylphosphine, $P(1\text{-Ad})_3$) to 83:17 (+66% ee , $Po\text{-Tol}_3$). Unfortunately, most ligands resulted in nearly racemic products, regardless of the subclass of phosphine utilized. This outcome was hypothesized to be a result of loss of stereochemical information due to β -hydride elimination to form 1-butene, followed by migratory insertion to the terminus (Figure 3.11). These steps are likely reversible, allowing for the branched product to still be formed with reduced enantiospecificity. However, if formation of a linear organometallic intermediate is a viable pathway, reductive elimination could additionally result in a linear product. Indeed, ethyl 4-*n*-butyl benzoate was often isolated, confirming the plausibility of this sequence. Inspection of the branched to linear product ratios revealed that larger phosphines suppressed the formation of the linear product, a result likely due to increased steric interactions that favor closer contact between the alkyl and aryl groups and enhancing the rate of reductive elimination. Inspection of the specificity versus the minimum solid cone angle revealed that 12 of 13 ligands with measured cone angles below 145° produced branched products with er values ranging from 52:48 to 56.5:43.5. Thus, it was hypothesized that phosphine ligands with minimum solid cone angles greater than 145° would favor reductive elimination, whereas those structures with solid cone angles less than 145° would favor β -hydride elimination.

To explore the role of ligand size in influencing the energetics of these two putative pathways, we turned to computing the transition states using the B3LYP functional (Figure 3.12).²⁴ Single point geometries were optimized and evaluated with 6-31G**/LACVP** basis set²⁵ and confirmed stationary points using Dunning's correlation

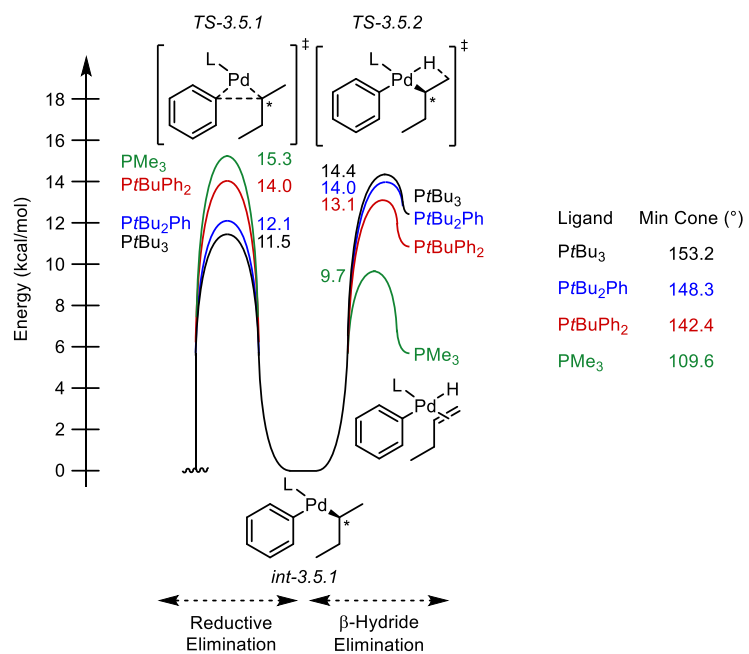


Figure 3.12. DFT calculated pathways with four ligands.

consistent triple- ζ basis set cc-pVTZ(-f).²⁶ Solvent correction was performed using $\epsilon = 2.38$ in an implicit solvent model.²⁷ Four ligands (PMe_3 , PtBuPh_2 , PtBu_2Ph , PtBu_3) were inspected that straddled the proposed 145° inflection point. First, the small ligand PMe_3 (solid cone angle = 109.6°) was examined, displaying a 5.6 kcal/mol preference for the undesired β -hydride elimination pathway. Conversely, the large ligand PtBu_3 (solid cone angle = 153.2°) resulted in a 2.9 kcal/mol preference toward the desired reductive elimination. These two outcomes are in agreement with the measured enantiospecificity, as PMe_3 resulted in a nearly racemic product ($ee = 6\%$) while PtBu_3 yielded a selective reaction ($ee = -80\%$). Turning our attention to PtBuPh_2 (solid cone angle = 142.4°), β -hydride elimination is expected to still be the lower energy pathway, and indeed, this step is calculated to be favored by 0.9 kcal/mol. Finally, PtBu_2Ph is above the threshold of 145° (solid cone angle = 148.3°), and thus expected to have a lower pathway toward reductive elimination. The calculated energy of the desired sequence is 1.9 kcal/mol lower in energy than β -hydride elimination. In total, the calculated reaction pathways confirm the role of ligand size in inducing reductive elimination.

As smaller ligands were expected to possibly undergo β -hydride elimination and subsequent loss of stereochemical information, these ligands were removed from consideration for examination of the retentive or invertive pathways. Outcomes from the remaining eight ligands (and one external validation) displayed a satisfying correlation to the ^{31}P NMR shift ($R^2 = 0.92$) in which more deshielded phosphorus atoms result in higher amounts of the inverted stereocenter product (Figure 3.11). Overall, more electron donating ligands must stabilize the open transition state or destabilize the cyclic transition state. As the former involves increasing positive charge at palladium, more electron rich

ligands likely stabilize this transition state, yielding higher enantiospecificity for the invertive pathway. Thus, the overall ligand effect with large ligands is primarily a result of electronic differences.

As electronic influences from the ligand augment the dominant transmetallation pathway, we hypothesized that similar effects would be present based on the aryl substrate. Five para substituted aryl chloride compounds were analyzed under the reaction conditions with $PtBu_3$ as the ligand and the enantiospecificity was measured (Figure 3.13). A Hammett plot was constructed using these reaction outcomes, and indeed a linear correlation was observed. As suspected, more electron rich aryl rings induced higher amounts of the invertive pathway, similar to the effect seen with more electron rich ligands. This result again indicates that more electron rich substituents bound to palladium stabilize the building positive charge in the open transition state.

Having confirmed the dominant role for electronic effects in the transmetallation pathway with the *sec*-butyl substrate, we questioned the generality of these conclusions with other boron nucleophiles. To test this possibility, a second substrate (4-phenyl-2-potassium-trifluoroborate-butane) was tested in the presence of an expanded ligand set containing primarily phosphines with solid cone angles larger than 145° (Figure 3.14). Astoundingly, the observed enantiospecificity ranged from 99:1 (retentive, PhSPhos, $\Delta\Delta G^\ddagger = 2.6$ kcal/mol) to 3:97 (invertive, P(1-Ad)₃, $\Delta\Delta G^\ddagger = -2.0$ kcal/mol). Reaction outcomes were compared to the same ^{31}P NMR shift, and a more modest trend was observed ($R^2 = 0.67$). This outcome remains under study; thus, a definitive explanation for the origin of the reduced correlation is as yet unknown.

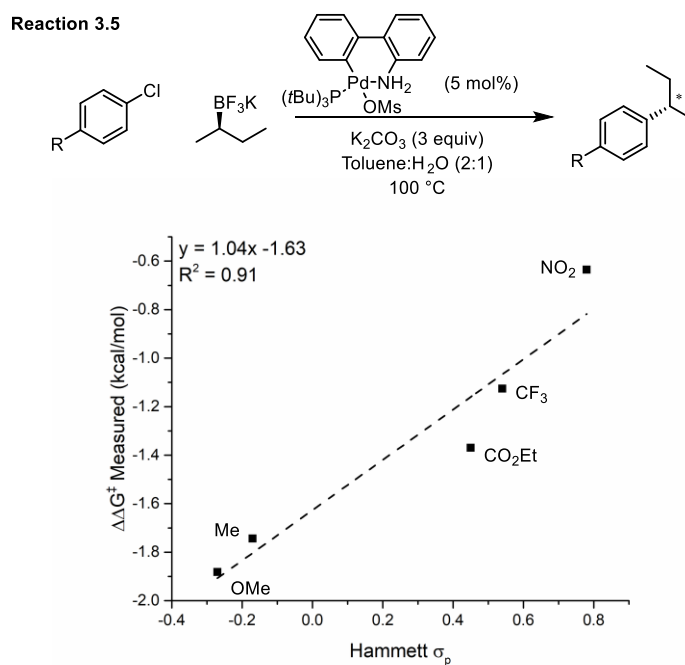
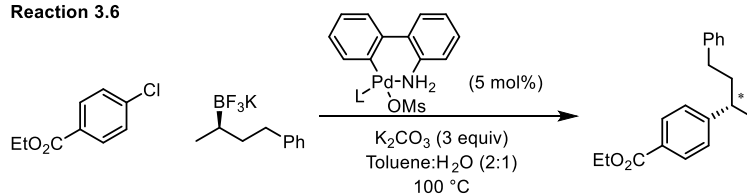


Figure 3.13. Hammett plot constructed using differentially substituted aryl chlorides.

Reaction 3.6



Entry	Ligand	es (%)	$\Delta\Delta G^\ddagger$ (kcal/mol)	^{31}P (δ)	Min Cone ($^\circ$)
1	PhSPhos	98	2.62	-11.6	173.3
2	P(<i>o</i> -Tol) ₃	95	2.13	-30.5	146.7
3	PPh ₃	92	1.86	-5.4	131.4
4	RuPhos	90	1.76	-8.8	187.5
5	CPhos	90	1.73	-8.6	206.4
6	SPhos	89	1.68	-8.0	201.9
7	XPhos	88	1.65	-11.5	209.8
8	PtBu ₂ Ph	77	1.21	39.0	148.3
9	PtBuCy ₂	72	1.07	27.0	144.6
10	PCy ₃	70	1.03	9.9	144.7
11	PMe _t Bu ₂	69	1.00	12.2	138.4
12	P <i>n</i> Bu(1-Ad) ₂	59	0.81	24.2	145.3
13	PtBu ₂ Cy	55	0.73	48	150.9
14	Pneop _t Bu ₂	-57	-0.76	19.8	144.6
15	PtBu ₃	-73	-1.10	61.1	153.2
16	P(1-Ad) ₃	-94	-2.03	59.4	156.2

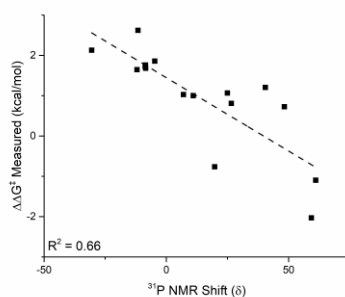


Figure 3.14. Reaction outcomes from ligand variation using a modified nucleophile and correlation to the ^{31}P NMR shift.

Conclusions

In summary, an alkyl-aryl Suzuki reaction has been studied to isolate the controlling mechanistic features. A steric threshold was identified, above which reductive elimination is favored over β -hydride elimination for a key intermediate. The stereo-defining transmetallation step was found to be primarily controlled by electronic interactions from both the ligand and aryl substrate. A combination of classic physical organic chemistry, computational reaction modeling, and univariate correlations were used to support these conclusions. Further work is needed to generalize the mechanistic hypotheses and to expand the reaction scope.

Experimental

Cycloisomerization Reactions

All synthetic chemistry with the cycloisomerization reactions was performed by Alec Christian. Therefore, only the raw data of the phosphines are presented here. Table 3.1 contains the data from Figure 3.4. Au–Cl bond distances were either taken from Fey and coworkers, or calculated using their method.¹³ Table 3.2 contains the data from Figure 3.5 and 3.6.

Suzuki Reactions

All synthetic chemistry was performed by Shibin Zhao; therefore only computational results are reported here. Table 3.3 contains the raw data for reaction 5. Table 3.4 contains the raw data for reaction 6.

Table 3.1. Phosphine data for [4+3]/[4+2] cycloisomerization.

Phosphine	[4+3]	[4+2]	$\Delta\Delta G^\ddagger$ kcal/mol	Au-Cl Å
XPhos	8.95	1.00	1.30	2.331
JohnPhos	13.70	1.00	1.55	2.329
CyJohnPhos	5.92	1.00	1.05	2.327
RuPhos	23.04	1.00	1.86	2.335
SPhos	15.24	1.00	1.61	2.338
<i>c</i> BRIDP	5.07	1.00	0.96	2.332
Cy- <i>c</i> BRIDP	4.18	1.00	0.85	2.330
<i>Pp</i> -Tol ₃	1.00	1.92	-0.39	2.312
P(<i>p</i> -OMePh) ₃	1.00	1.94	-0.39	2.319
P(<i>p</i> -FPh) ₃	1.00	3.32	-0.71	2.311
PMe ₃	1.00	2.09	-0.44	2.309
P(<i>o</i> -OMePh) ₃	2.23	1.00	0.48	2.329
<i>Po</i> -Tol ₃	1.00	2.09	-0.44	2.320
PEt ₃	1.00	1.26	-0.14	2.318
(2,4- <i>t</i> Bu ₂ Ph)Phosphite	1.00	9.50	-1.33	2.300

Table 3.2. Phosphine data for [2+3]/[2+2] cycloisomerization.

Phosphine	[2+3]	[2+2]	$\Delta\Delta G^\ddagger$ kcal/mol	L/B ₁ ave	Au-Cl Å
<i>Pp</i> -Tol ₃	1.45	1.00	0.22	1.17	2.312
PMe ₃	1.54	1.00	0.25	1.47	2.309
P(<i>p</i> -OMePh) ₃	1.45	1.00	0.22	1.25	2.319
P(<i>p</i> -FPh) ₃	1.18	1.00	0.10	1.37	2.311
<i>Pt</i> Bu ₃	2.37	1.00	0.51	1.32	2.328
Xphos	13.42	1.00	1.54	2.20	2.331
JohnPhos	6.55	1.00	1.11	1.94	2.329
CyJohnPhos	2.43	1.00	0.53	1.78	2.327
RuPhos	2.66	1.00	0.58	1.58	2.335
SPhos	2.71	1.00	0.59	1.79	2.338
<i>c</i> BRIDP	5.39	1.00	1.00	1.81	2.332
Cy- <i>c</i> BRIDP	3.53	1.00	0.75	1.48	2.330
PPh ₃	1.42	1.00	0.21	1.43	2.310
AZPhos	18.00	1.00	1.71	3.00	2.337
<i>t</i> BuXPhos	26.19	1.00	1.93	2.47	2.328

Table 3.3. Raw data for reaction 3.5.

Phosphine	Branched:linear Ratio	$\Delta\Delta G^\ddagger$ kcal/mol	ee	$\Delta\Delta G^\ddagger$ kcal/mol	^{31}P NMR (δ)	min cone
XPhos	1.05	0.029	11	0.131	-12.0	209.8
CPhos	0.87	-0.085	10	0.119	-8.6	206.4
SPhos	1.50	0.240	23	0.272	-8.4	201.9
RuPhos	1.40	0.199	14	0.167	-8.5	187.5
CyJohnPhos	0.80	-0.132	7	0.083	-12.6	183.6
P(1-Ad) ₃	190.00	3.107	-93	-1.968	59.4	178.0
Ph ₂ SPhos	2.40	0.518	56	0.755	-11.6	173.3
<i>Pr</i> Bu ₃	16.00	1.642	-80	-1.290	61.1	153.2
<i>Po</i> -Tol ₃	2.40	0.518	64	0.893	-30.5	146.7
<i>Pn</i> BuAd ₂	3.70	0.775	5	0.053	26.6	145.3
PCy ₃	0.25	-0.821	4	0.047	7.0	144.7
<i>Pr</i> Bu ₂ neop	2.30	0.493	-68	-0.982	19.8	144.6
<i>Pr</i> BuPh ₂	3.80	0.790	23	0.282	19.1	142.4
PMe <i>t</i> Bu ₂	0.10	-1.363	2	0.024	11.0	138.4
P(<i>o</i> -OMePh) ₃	2.20	0.467	16	0.191	-37.1	136.6
PPh ₃	1.10	0.056	11	0.131	-4.7	131.4
<i>Pp</i> -Tol ₃	1.10	0.056	12	0.143	-8.0	131.1
PPh ₂ Bn	0.80	-0.132	10	0.119	-10.4	125.3
<i>Pn</i> Bu ₃	0.10	-1.363	6	0.071	-32.3	124.6
PEt ₃	0.10	-1.363	9	0.107	-20.4	121.5
PMe ₃	0.08	-1.496	6	0.071	-62.0	109.6

Table 3.4. Raw data for reaction 3.6.

Phosphine	$\Delta\Delta G^\ddagger$ kcal/mol	^{31}P NMR (δ)	Au-P (\AA)
<i>Po</i> -Tol ₃	2.13	-30.5	2.294
PhSPhos	2.62	-11.6	2.273
XPhos	1.65	-11.5	2.289
Ruphos	1.76	-8.8	2.289
CPhos	1.73	-8.6	2.287
SPhos	1.68	-8.0	2.287
PPh ₃	1.86	-5.4	2.278
PCy ₃	1.03	9.9	2.289
P <i>Me</i> tBu ₂	1.00	12.2	2.288
P <i>neop</i> tBu ₂	-0.76	19.8	2.301
P <i>n</i> BuAd ₂	0.81	24.2	2.298
P <i>t</i> BuCy ₂	1.07	27.0	2.292
P <i>t</i> Bu ₂ Ph	1.21	39.0	2.291
P <i>t</i> Bu ₂ Cy	0.73	48.0	2.298
P(1-Ad) ₃	-2.03	59.4	2.306
P <i>t</i> Bu ₃	-1.10	61.1	2.300

DFT Computational Details

All calculations were performed using density functional theory^{24a} as implemented in the Jaguar 9.1 suite of ab initio quantum chemistry programs.²⁸ Geometry optimizations were performed with the B3LYP^{24b-e, 29} functional using the 6-31G** basis set.³⁰ Palladium was represented using the Los Alamos LACVP** basis set that includes relativistic core potentials.²⁵ Single point energies were computed from the optimized geometries using Dunning's correlation-consistent triple- ζ basis set (cc-pVTZ(-f)²⁶) that includes a double set of polarization functions. Vibrational frequencies were computed at the B3LYP/6-31G** level of theory were used to derive zero point energy and vibrational entropy corrections from unscaled frequencies. Solvation energies were evaluated by a self-consistent reaction field (SCRF) approach with the dielectric constant $\epsilon = 2.38$ (toluene) using the optimized gas phase structures.²⁷ Gibbs energy was calculated according to the formula $G = (E(\text{SCF}) * 23.0605423 + \text{ZPE}) - 373.15 * S + G(\text{solv})$. ΔG is compared to int-3.5.1. Table 3.5 includes the energies of these components for each ligand.

New Phosphines

Phosphines Cy-*c*BRIDP, *c*BRIDP, AZPhos, *t*BuXPhos, PhSPhos, CPhos, *Pt*BuCy₂ and *Pt*Bu₂Cy were not included in the study presented in Chapter 2. The structures were obtained using the same methods from Chapter 2 and these steps are repeated here.

Table 3.5. Calculated energy values.

Structure	E(SCF) (eV)	ZPE (kcal/mol)	S (gas) (cal/mol)	G (solv) (kcal/mol)	ΔG (kcal/mol)
PMe ₃ int-3.5.1	-26600.714	204.00	152.75	-2.27	0.00
PMe ₃ TS-3.5.1	-26600.072	204.31	153.25	-1.95	15.25
PMe ₃ RE prod	-26602.085	206.08	158.58	-2.34	-31.78
PMe ₃ TS-3.5.2	-26600.271	202.07	147.82	-2.75	9.65
PMe ₃ β HE prod	-26600.415	202.86	149.76	-3.48	5.66
PtBuPh ₂ int- 3.5.1	-40248.198	324.84	207.55	-3.44	0.00
PtBuPh ₂ TS- 3.5.1	-40247.699	324.99	202.36	-3.00	14.03
PtBuPh ₂ RE prod	-40249.716	326.59	207.49	-3.06	-32.86
PtBuPh ₂ TS- 3.5.2	-40247.689	322.66	197.34	-3.72	13.09
PtBuPh ₂ β HE prod	-40247.762	323.39	200.23	-3.91	10.87
PtBu ₂ Ph int- 3.5.1	-38239.471	344.41	203.56	-2.63	0.00
PtBu ₂ Ph TS- 3.5.1	-38238.948	344.69	204.37	-2.56	12.11
PtBu ₂ Ph RE prod	-38240.931	346.39	201.32	-2.34	-30.56
PtBu ₂ Ph TS- 3.5.2	-38238.896	342.62	195.72	-3.03	14.00
PtBu ₂ Ph β HE prod	-38238.972	343.49	197.47	-3.02	12.47
PtBu ₃ int-3.5.1	-36230.359	365.24	201.40	-2.12	0.00
PtBu ₃ TS-3.5.1	-36229.903	365.25	199.54	-1.85	11.49
PtBu ₃ RE prod	-36231.87	366.76	203.66	-1.47	-33.52
PtBu ₃ TS-3.5.2	-36229.76	363.29	194.05	-2.37	14.36
PtBu ₃ β HE prod	-36229.832	364.08	197.03	-2.33	12.41

Conformational Search

A conformational search on the respective phosphine oxides was performed using the MacroModel suite from Schrödinger³¹ using an OPLS_2005 force field without solvent corrections. A Monte-Carlo molecular mechanics method was employed with extended torsional sampling. The output was restricted to 20 structures within 3.11 kcal/mol (13 kJ/mol) of the lowest energy conformer, with a maximum atom deviation cutoff of 1 Å. Each of the eight new phosphines were restricted to having the aryl ring (implicated in blocking a coordination site) in a similar direction as the P=O bond. This was thought to ensure similarity to how the phosphine would be bound. Conformers were submitted to a geometry optimization in Gaussian 09³² using the 6-31+G(d,p) basis set and M06-2x functional. This basis set was chosen in order to match the conformational search basis set. The M06-2x functional was chosen because of its accuracy for a large number of main group systems.³³ Cone angle measurements were performed by changing the oxygen atom to palladium and setting the distance between palladium and phosphorus to 2.28 Å and then measuring angles with the program Solid-G.³⁴ Conformers with the largest and smallest cone angles were then submitted to an optimization and frequency calculation at the M06-2x/def2-TZVP level of theory to obtain IR vibration data. A triple zeta potential basis set was chosen along with the M06-2x functional, as these generally lead to quantitative correlations.^{33, 35} Linear scaling factors³⁶ were not applied to the calculated vibrations because these are constants, and thus would not affect correlation. Cone angle measurements were then recalculated for consistency, and Sterimol measurements were performed with Molecular Modeling Pro.³⁷

Parameters

Calculated parameters are included in the following four tables. Table 3.6 includes three parameters from NMR spectra, followed by the measured solid cone angles from the minimum and maximum cone angle conformer, and finally the average steric values.

Table 3.6. Parameters for eight new phosphines presented in this chapter.

Phosphine	Phosphine ^{31}P NMR (δ)	Phosphine Selenide ^{31}P NMR shift (δ)	$^1J_{\text{P-Se}}$ (Hz)	Cone Max	Cone Min
<i>c</i> BRIDP	37.8	86.0	721	184.90	181.59
Cy- <i>c</i> BRIDP	9.9	62.4	703	191.53	184.82
AZPhos	18.1	71.2	736	187.68	185.42
<i>t</i> BuXPhos	21.5	70.6	742	211.00	209.90
PhSPhos	-11.6			173.27	173.27
CPhos	-8.6			223.52	206.40
P <i>t</i> BuCy ₂	25.0			147.61	144.61
P <i>t</i> Bu ₂ Cy	48.3			150.91	150.91

Phosphine	Max P=O frequency	Min P=O intensity	Min P=O frequency	Min P=O intensity
<i>c</i> BRIDP	1203.31	39.3959	1201.42	50.1032
Cy- <i>c</i> BRIDP	1250.06	54.3259	1256.51	44.9595
AZPhos	1215.05	63.0468	1215.05	63.0468
<i>t</i> BuXPhos	1214.02	61.8358	1214.02	61.8358
PhSPhos	1259.52	130.6653	1259.52	130.6653
CPhos	1254.88	55.9633	1259.26	36.3339
P <i>t</i> BuCy ₂	1215.19	73.4128	1206.89	80.7930
P <i>t</i> Bu ₂ Cy	1215.61	41.2241	1215.61	41.2241

Phosphine	Max B ₁	Max B ₅	Max L	Max L/B ₁	Max B ₁ *L
<i>c</i> BRIDP	4.06	8.72	7.60	1.87	30.87
Cy- <i>c</i> BRIDP	4.88	8.34	7.06	1.45	34.43
AZPhos	4.01	6.32	12.16	3.03	48.72
<i>t</i> BuXPhos	4.00	7.74	10.04	2.51	40.18
PhSPhos	4.34	7.08	7.37	1.70	31.98
CPhos	4.11	7.28	7.81	1.90	32.06
P <i>t</i> BuCy ₂	4.19	6.82	6.15	1.47	25.77
P <i>t</i> Bu ₂ Cy	4.06	6.84	5.42	1.33	22.03

Phosphine	Min B ₁	Min B ₅	Min L	Min L/B ₁	Min B ₁ *L
<i>c</i> BRIDP	4.04	8.38	7.07	1.75	28.55
Cy- <i>c</i> BRIDP	4.59	8.40	6.99	1.52	32.06
AZPhos	3.96	6.41	11.72	2.96	46.45
<i>t</i> BuXPhos	4.00	7.73	9.71	2.43	38.85
PhSPhos	4.34	7.08	7.37	1.70	31.98
CPhos	4.43	0.69	7.36	1.66	32.63
P <i>t</i> BuCy ₂	3.99	6.63	6.15	1.54	24.56

Table 3.6. continued.

Phosphine	Min B ₁	Min B ₅	Min L	Min L/B ₁	Min B ₁ *L
<i>PtBu</i> ₂ Cy	4.06	6.84	5.42	1.33	22.03

Phosphine	Average cone	Average B ₁	Average B ₅	Average L	Average L/B ₁
<i>c</i> BRIDP	183.25	4.05	8.55	7.34	1.81
Cy- <i>c</i> BRIDP	188.18	4.73	8.37	7.02	1.48
AZPhos	186.55	3.99	6.37	11.94	3.00
<i>t</i> BuXPhos	210.45	4.00	7.74	9.88	2.47
PhSPhos	173.27	4.34	7.08	7.37	1.70
CPhos	206.40	4.27	3.98	7.59	1.78
<i>PtBu</i> Cy ₂	146.11	4.09	6.72	6.15	1.50
<i>PtBu</i> ₂ Cy	150.91	4.06	6.84	5.42	1.33

Phosphine	Average B ₁ *L
<i>c</i> BRIDP	29.71
Cy- <i>c</i> BRIDP	33.24
AZPhos	47.59
<i>t</i> BuXPhos	39.52
PhSPhos	31.98
CPhos	32.34
<i>PtBu</i> Cy ₂	25.16
<i>PtBu</i> ₂ Cy	22.03

References

1. (a) Shi, X.; Gorin, D. J.; Toste, F. D., Synthesis of 2-Cyclopentenones by Gold(I)-Catalyzed Rautenstrauch Rearrangement. *J. Am. Chem. Soc.* **2005**, *127* (16), 5802-5803; (b) Gorin, D. J.; Toste, F. D., Relativistic Effects in Homogeneous Gold Catalysis. *Nature* **2007**, *446* (7134), 395-403.
2. (a) BabaAhmadi, R.; Ghanbari, P.; Rajabi, N. A.; Hashmi, A. S. K.; Yates, B. F.; Ariaferd, A., A Theoretical Study on the Protodeauration Step of the Gold(I)-Catalyzed Organic Reactions. *Organometallics* **2015**, *34* (13), 3186-3195; (b) Ranieri, B.; Escofet, I.; Echavarren, A. M., Anatomy of Gold Catalysts: Facts and Myths. *Org. Biomol. Chem.* **2015**, *13* (26), 7103-7118.
3. (a) Kennedy-Smith, J. J.; Staben, S. T.; Toste, F. D., Gold(I)-Catalyzed Conia-Ene Reaction of β -Ketoesters with Alkynes. *J. Am. Chem. Soc.* **2004**, *126* (14), 4526-4527; (b) Luzung, M. R.; Markham, J. P.; Toste, F. D., Catalytic Isomerization of 1,5-Enynes to Bicyclo[3.1.0]hexenes. *J. Am. Chem. Soc.* **2004**, *126* (35), 10858-10859.
4. Sherry, B. D.; Toste, F. D., Gold(I)-Catalyzed Propargyl Claisen Rearrangement. *J. Am. Chem. Soc.* **2004**, *126* (49), 15978-15979.
5. (a) Johansson, M. J.; Gorin, D. J.; Staben, S. T.; Toste, F. D., Gold(I)-Catalyzed Stereoselective Olefin Cyclopropanation. *J. Am. Chem. Soc.* **2005**, *127* (51), 18002-18003; (b) LaLonde, R. L.; Sherry, B. D.; Kang, E. J.; Toste, F. D., Gold(I)-Catalyzed Enantioselective Intramolecular Hydroamination of Allenes. *J. Am. Chem. Soc.* **2007**, *129* (9), 2452-2453; (c) Muñoz, M. P.; Adrio, J.; Carretero, J. C.; Echavarren, A. M., Ligand Effects in Gold- and Platinum-Catalyzed Cyclization of Enynes: Chiral Gold Complexes for Enantioselective Alkoxy cyclization. *Organometallics* **2005**, *24* (6), 1293-1300.
6. (a) Mauleón, P.; Krinsky, J. L.; Toste, F. D., Mechanistic Studies on Au(I)-Catalyzed [3,3]-Sigmatropic Rearrangements using Cyclopropane Probes. *J. Am. Chem. Soc.* **2009**, *131* (12), 4513-4520; (b) Wang, Z. J.; Benitez, D.; Tkatchouk, E.; Goddard Iii, W. A.; Toste, F. D., Mechanistic Study of Gold(I)-Catalyzed Intermolecular Hydroamination of Allenes. *J. Am. Chem. Soc.* **2010**, *132* (37), 13064-13071.
7. (a) Gorin, D. J.; Sherry, B. D.; Toste, F. D., Ligand Effects in Homogeneous Au Catalysis. *Chem. Rev.* **2008**, *108* (8), 3351-3378; (b) Wang, W.; Hammond, G. B.; Xu, B., Ligand Effects and Ligand Design in Homogeneous Gold(I) Catalysis. *J. Am. Chem. Soc.* **2012**, *134* (12), 5697-5705.
8. Benitez, D.; Shapiro, N. D.; Tkatchouk, E.; Wang, Y.; Goddard, W. A.; Toste, F. D., A Bonding Model for Gold(I) Carbene Complexes. *Nat. Chem.* **2009**, *1* (6), 482-486.
9. Herrero-Gómez, E.; Nieto-Oberhuber, C.; López, S.; Benet-Buchholz, J.; Echavarren, A. M., Cationic η^1/η^2 -Gold(I) Complexes of Simple Arenes. *Angew. Chem. Int. Ed.* **2006**, *45* (33), 5455-5459.

10. Mauleón, P.; Zeldin, R. M.; González, A. Z.; Toste, F. D., Ligand-Controlled Access to [4 + 2] and [4 + 3] Cycloadditions in Gold-Catalyzed Reactions of Allene-Dienes. *J. Am. Chem. Soc.* **2009**, *131* (18), 6348-6349.
11. Benitez, D.; Tkatchouk, E.; Gonzalez, A. Z.; Goddard, W. A.; Toste, F. D., On the Impact of Steric and Electronic Properties of Ligands on Gold(I)-Catalyzed Cycloaddition Reactions. *Org. Lett.* **2009**, *11* (21), 4798-4801.
12. (a) Barder, T. E.; Walker, S. D.; Martinelli, J. R.; Buchwald, S. L., Catalysts for Suzuki–Miyaura Coupling Processes: Scope and Studies of the Effect of Ligand Structure. *J. Am. Chem. Soc.* **2005**, *127* (13), 4685-4696; (b) Suzuki, K.; Hori, Y.; Nishikawa, T.; Kobayashi, T., A Novel (2,2-Diarylviny)phosphine/Palladium Catalyst for Effective Aromatic Amination. *Adv. Synth. Catal.* **2007**, *349* (13), 2089-2091.
13. Jover, J. s.; Fey, N.; Harvey, J. N.; Lloyd-Jones, G. C.; Orpen, A. G.; Owen-Smith, G. J. J.; Murray, P.; Hose, D. R. J.; Osborne, R.; Purdie, M., Expansion of the Ligand Knowledge Base for Monodentate P-Donor Ligands (LKB-P)†. *Organometallics* **2010**, *29* (23), 6245-6258.
14. Chemler, S. R.; Trauner, D.; Danishefsky, S. J., The B-Alkyl Suzuki–Miyaura Cross-Coupling Reaction: Development, Mechanistic Study, and Applications in Natural Product Synthesis. *Angew. Chem. Int. Ed.* **2001**, *40* (24), 4544-4568.
15. (a) van den Hoogenband, A.; Lange, J. H. M.; Terpstra, J. W.; Koch, M.; Visser, G. M.; Visser, M.; Korstanje, T. J.; Jastrzebski, J. T. B. H., Ruphos-Mediated Suzuki Cross-Coupling of Secondary Alkyl Trifluoroborates. *Tetrahedron Lett.* **2008**, *49* (26), 4122-4124; (b) Imao, D.; Glasspoole, B. W.; Laberge, V. S.; Crudden, C. M., Cross Coupling Reactions of Chiral Secondary Organoboronic Esters With Retention of Configuration. *J. Am. Chem. Soc.* **2009**, *131* (14), 5024-5025; (c) Rudolph, A.; Lautens, M., Secondary Alkyl Halides in Transition-Metal-Catalyzed Cross-Coupling Reactions. *Angew. Chem. Int. Ed.* **2009**, *48* (15), 2656-2670; (d) Ohmura, T.; Awano, T.; Suginome, M., Stereospecific Suzuki–Miyaura Coupling of Chiral α -(Acylamino)benzylboronic Esters with Inversion of Configuration. *J. Am. Chem. Soc.* **2010**, *132* (38), 13191-13193; (e) Sandrock, D. L.; Jean-Gérard, L.; Chen, C.-y.; Dreher, S. D.; Molander, G. A., Stereospecific Cross-Coupling of Secondary Alkyl β -Trifluoroboratoamides. *J. Am. Chem. Soc.* **2010**, *132* (48), 17108-17110; (f) Awano, T.; Ohmura, T.; Suginome, M., Inversion or Retention? Effects of Acidic Additives on the Stereochemical Course in Enantiospecific Suzuki–Miyaura Coupling of α -(Acetylamino)benzylboronic Esters. *J. Am. Chem. Soc.* **2011**, *133* (51), 20738-20741; (g) Molander, G. A.; Wisniewski, S. R., Stereospecific Cross-Coupling of Secondary Organotrifluoroborates: Potassium 1-(Benzyloxy)alkyltrifluoroborates. *J. Am. Chem. Soc.* **2012**, *134* (40), 16856-16868; (h) Li, L.; Wang, C.-Y.; Huang, R.; Biscoe, M. R., Stereoretentive Pd-Catalysed Stille Cross-Coupling Reactions of Secondary Alkyl Azastannatranes and Aryl Halides. *Nat Chem* **2013**, *5* (7), 607-612; (i) Li, L.; Zhao, S.; Joshi-Pangu, A.; Diane, M.; Biscoe, M. R., Stereospecific Pd-Catalyzed Cross-Coupling Reactions of Secondary Alkylboron Nucleophiles and Aryl Chlorides. *J. Am. Chem. Soc.* **2014**, *136* (40), 14027-14030; (j)

Sun, C.; Potter, B.; Morken, J. P., A Catalytic Enantiotopic-Group-Selective Suzuki Reaction for the Construction of Chiral Organoboronates. *J. Am. Chem. Soc.* **2014**, *136* (18), 6534-6537; (k) Wang, C.-Y.; Derosa, J.; Biscoe, M. R., Configurationally Stable, Enantioenriched Organometallic Nucleophiles in Stereospecific Pd-Catalyzed Cross-Coupling Reactions: an Alternative Approach to Asymmetric Synthesis. *Chemical Science* **2015**, *6* (9), 5105-5113; (l) Liang, Y.; Fu, G. C., Stereoconvergent Negishi Arylations of Racemic Secondary Alkyl Electrophiles: Differentiating between a CF₃ and an Alkyl Group. *J. Am. Chem. Soc.* **2015**, *137* (30), 9523-9526; (m) Schley, N. D.; Fu, G. C., Nickel-Catalyzed Negishi Arylations of Propargylic Bromides: A Mechanistic Investigation. *J. Am. Chem. Soc.* **2014**, *136* (47), 16588-16593.

16. Wang, C. Y.; Ralph, G.; Derosa, J.; Biscoe, M. R., Stereospecific Palladium-Catalyzed Acylation of Enantioenriched Alkylcarbostannatranes: A General Alternative to Asymmetric Enolate Reactions. *Angew. Chem. Int. Ed.* **2017**, *56* (3), 856-860.

17. Espinet, P.; Echavarren, A. M., The Mechanisms of the Stille Reaction. *Angew. Chem. Int. Ed.* **2004**, *43* (36), 4704-4734.

18. Labadie, J. W.; Stille, J. K., Mechanisms of the Palladium-Catalyzed Couplings of Acid Chlorides with Organotin Reagents. *J. Am. Chem. Soc.* **1983**, *105* (19), 6129-6137.

19. Ye, J.; Bhatt, R. K.; Falck, J. R., Stereospecific Palladium/Copper Cocatalyzed Cross-Coupling of α -alkoxy- and α -Aminostannanes with Acyl Chlorides. *J. Am. Chem. Soc.* **1994**, *116* (1), 1-5.

20. Casado, A. L.; Espinet, P.; Gallego, A. M., Mechanism of the Stille Reaction. 2. Couplings of Aryl Triflates with Vinyltributyltin. Observation of Intermediates. A More Comprehensive Scheme. *J. Am. Chem. Soc.* **2000**, *122* (48), 11771-11782.

21. (a) Lennox, A. J. J.; Lloyd-Jones, G. C., Organotrifluoroborate Hydrolysis: Boronic Acid Release Mechanism and an Acid-Base Paradox in Cross-Coupling. *J. Am. Chem. Soc.* **2012**, *134* (17), 7431-7441; (b) Lennox, A. J. J.; Lloyd-Jones, G. C., Selection of boron reagents for Suzuki-Miyaura coupling. *Chem. Soc. Rev.* **2014**, *43* (1), 412-443.

22. Kinzel, T.; Zhang, Y.; Buchwald, S. L., A New Palladium Precatalyst Allows for the Fast Suzuki-Miyaura Coupling Reactions of Unstable Polyfluorophenyl and 2-Heteroaryl Boronic Acids. *J. Am. Chem. Soc.* **2010**, *132* (40), 14073-14075.

23. Hartwig, J. F.; Kawatsura, M.; Hauck, S. I.; Shaughnessy, K. H.; Alcazar-Roman, L. M., Room-Temperature Palladium-Catalyzed Amination of Aryl Bromides and Chlorides and Extended Scope of Aromatic C-N Bond Formation with a Commercial Ligand. *J. Org. Chem.* **1999**, *64* (15), 5575-5580.

24. (a) Parr, R. G.; Weitao, Y., *Density-Functional Theory of Atoms and Molecules*. Oxford University Press: 1994; (b) Slater, J. C., *Quantum Theory of Molecules and Solids*

: *v4: the Self-Consistent Field for Molecules and Solids*. Mc-Graw-Hill: New York, 1974; (c) Vosko, S. H.; Wilk, L.; Nusair, M., Accurate Spin-Dependent Electron Liquid Correlation Energies for Local Spin Density Calculations: A Critical Analysis. *Can. J. Phys.* **1980**, *58* (8), 1200-1211; (d) Becke, A. D., Density-Functional Exchange-Energy Approximation with Correct Asymptotic Behavior. *Phys. Rev. A* **1988**, *38* (6), 3098-3100; (e) Lee, C.; Yang, W.; Parr, R. G., Development of the Colle-Salvetti Correlation-Energy Formula into a Functional of the Electron Density. *Phys. Rev. B* **1988**, *37* (2), 785-789.

25. (a) Hay, P. J.; Wadt, W. R., Ab initio Effective Core Potentials for Molecular Calculations. Potentials for the Transition Metal Atoms Sc to Hg. *J. Chem. Phys.* **1985**, *82* (1), 270-283; (b) Wadt, W. R.; Hay, P. J., Ab initio Effective Core Potentials for Molecular Calculations. Potentials for Main Group Elements Na to Bi. *J. Chem. Phys.* **1985**, *82* (1), 284-298; (c) Hay, P. J.; Wadt, W. R., Ab initio Effective Core Potentials for Molecular Calculations. Potentials for K to Au Including the Outermost Core Orbitals. *J. Chem. Phys.* **1985**, *82* (1), 299-310.

26. Jr., T. H. D., Gaussian Basis Sets for Use in Correlated Molecular Calculations. I. The Atoms Boron Through Neon and Hydrogen. *J. Chem. Phys.* **1989**, *90* (2), 1007-1023.

27. (a) Marten, B.; Kim, K.; Cortis, C.; Friesner, R. A.; Murphy, R. B.; Ringnalda, M. N.; Sitkoff, D.; Honig, B., New Model for Calculation of Solvation Free Energies: Correction of Self-Consistent Reaction Field Continuum Dielectric Theory for Short-Range Hydrogen-Bonding Effects. *J. Phys. Chem.* **1996**, *100* (28), 11775-11788; (b) Friedrichs, M.; Zhou, R.; Edinger, S. R.; Friesner, R. A., Poisson-Boltzmann Analytical Gradients for Molecular Modeling Calculations. *J. Phys. Chem. B* **1999**, *103* (16), 3057-3061; (c) Edinger, S. R.; Cortis, C.; Shenkin, P. S.; Friesner, R. A., Solvation Free Energies of Peptides: Comparison of Approximate Continuum Solvation Models with Accurate Solution of the Poisson-Boltzmann Equation. *J. Phys. Chem. B* **1997**, *101* (7), 1190-1197.

28. Bochevarov, A. D.; Harder, E.; Hughes, T. F.; Greenwood, J. R.; Braden, D. A.; Philipp, D. M.; Rinaldo, D.; Halls, M. D.; Zhang, J.; Friesner, R. A., Jaguar: A High-Performance Quantum Chemistry Software Program with Strengths in Life and Materials Sciences. *Int. J. Quantum Chem* **2013**, *113* (18), 2110-2142.

29. Becke, A. D., Density-Functional Thermochemistry. III. The Role of Exact Exchange. *J. Chem. Phys.* **1993**, *98* (7), 5648-5652.

30. Ditchfield, R.; Hehre, W. J.; Pople, J. A., Self-Consistent Molecular-Orbital Methods. IX. An Extended Gaussian-Type Basis for Molecular-Orbital Studies of Organic Molecules. *J. Chem. Phys.* **1971**, *54* (2), 724-728.

31. *Schrödinger Release 2014-3: MacroModel*, version 10.5; Schrödinger, LLC: New York, NY, 2014.

32. Frisch, M. J.; Trucks, G. W.; Schlegel, H. B.; Scuseria, G. E.; Robb, M. A.; Cheeseman, J. R.; Scalmani, G.; Barone, V.; Mennucci, B.; Petersson, G. A.; Nakatsuji, H.; Caricato, M. L.; X.; Hratchian, H. P.; Izmaylov, A. F.; Bloino, J.; Zheng, G.; Sonnenberg, J. L.; Hada, M.; Ehara, M.; Toyota, K.; Fukuda, R.; Hasegawa, J.; Ishida, M.; Nakajima, T.; Honda, Y.; Kitao, O.; Nakai, H.; Vreven, T.; Montgomery, J. A., Jr.; Peralta, J. E.; Ogliaro, F.; Bearpark, M.; Heyd, J. J.; Brothers, E.; Kudin, K. N.; Staroverov, V. N.; Kobayashi, R.; Normand, J.; Raghavachari, K.; Rendell, A.; Burant, J. C.; Iyengar, S. S.; Tomasi, J.; Cossi, M.; Rega, N.; Millam, N. J.; Klene, M.; Knox, J. E.; Cross, J. B.; Bakken, V.; Adamo, C.; Jaramillo, J.; Gomperts, R.; Stratmann, R. E.; Yazyev, O.; Austin, A. J.; Cammi, R.; Pomelli, C.; Ochterski, J. W.; Martin, R. L.; Morokuma, K.; Zakrzewski, V. G.; Voth, G. A.; Salvador, P.; Dannenberg, J. J.; Dapprich, S.; Daniels, A. D.; Farkas, Ö.; Foresman, J. B.; Ortiz, J. V.; Cioslowski, J.; Fox, D. J. *Gaussian 09, Revision D.01*, Gaussian, Inc.: Wallingford, CT, 2009.
33. Zhao, Y.; Truhlar, D., The M06 Suite of Density Functionals for Main Group Thermochemistry, Thermochemical Kinetics, Noncovalent Interactions, Excited States, and Transition Elements: Two New Functionals and Systematic Testing of Four M06-Class Functionals and 12 Other Functionals. *Theor. Chem. Acc.* **2008**, *120* (1-3), 215-241.
34. Guzei, I. A.; Wendt, M., An Improved Method for the Computation of Ligand Steric Effects Based on Solid Angles. *Dalton Trans.* **2006**, (33), 3991-9.
35. Weigend, F.; Ahlrichs, R., Balanced Basis Sets of Split Valence, Triple Zeta Valence and Quadruple Zeta Valence Quality for H to Rn: Design and Assessment of Accuracy. *PCCP* **2005**, *7* (18), 3297-3305.
36. Merrick, J. P.; Moran, D.; Radom, L., An Evaluation of Harmonic Vibrational Frequency Scale Factors. *J. Phys. Chem. A* **2007**, *111* (45), 11683-11700.
37. Quinn, J. A. *Molecular Modeling Pro*, 6.36; Norgwyn Montgomery Software Inc.: North Wales, PA

CHAPTER 4

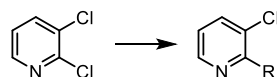
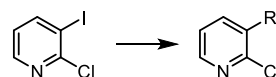
SELECTIVE AMINE ARYLATION WITH MULTIPLY HALOGENATED PYRIDINES

Introduction

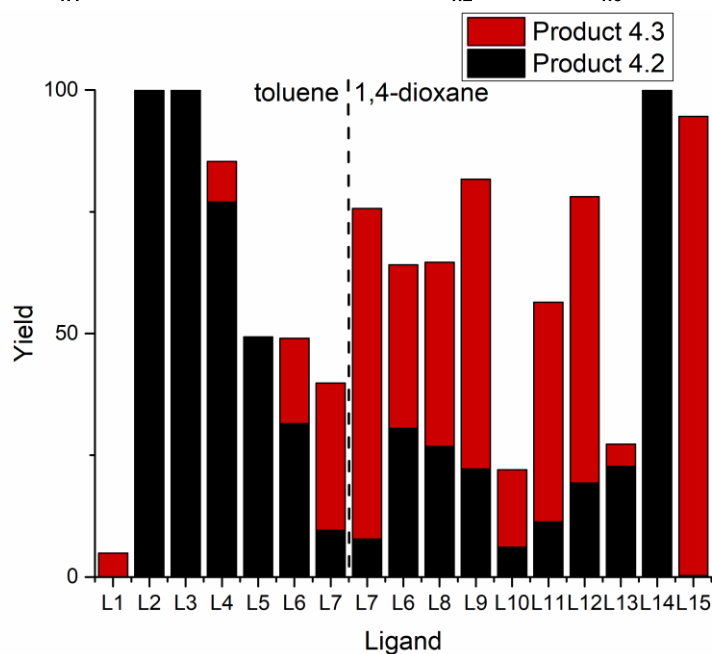
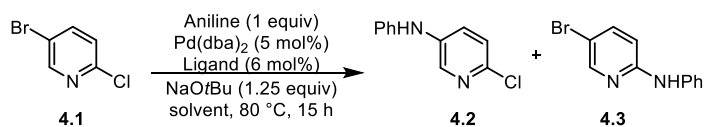
For synthetic chemists, novel site- and chemo-selective reactions can open exciting new routes to generate diverse architectures. Discriminatory synthesis involving differentially substituted pyridines are particularly interesting within drug discovery efforts, especially when conventional reactivity trends can be inverted. Heterocycles bearing identical leaving groups generally react at the more electrophilic position (Figure 4.1).¹ However, when different halogens are substituted on the ring, bond dissociation energies generally dominate the reactivity trends.² By selecting pyridines in which these two driving forces oppose, the expected BDE-based chemoselectivity may be overcome via the combination of intrinsic polarization and catalyst promotion.³ This chapter presents a study to identify conditions under which differentially substituted pyridines selectively react under Buchwald-Hartwig coupling conditions, a project performed in collaboration with Mitch Keylor and Kian Tan at Novartis. All synthetic chemistry was performed at Novartis.

To initiate our investigation, the reaction between 5-bromo-2-chloropyridine (**4.1**) and aniline was selected as a model (Figure 4.1). A large array of donor ligands was

Previous Trends

Selectivity Determined by
Partial Charge/LUMO coefficientSelectivity Determined by
Bond Dissociation Enthalpy (BDE)

Model Reaction



L1	$PtPr_3$	L6	DPPF (R = P(Ph) ₂)	L11	<i>R,R</i> -Et-Ferrocene
L2	$PtBu_3$	L7	DTBPF (R = <i>Pt</i> Bu ₂)	L12	<i>R,R</i> - <i>i</i> Pr-Ferrocene
L3	SPhos	L8	DCyPF (R = PCy ₂)	L13	HiersoPhos (R = P(5-Me-2-furanyl) ₂)
L4	DPEPhos	L9	DIPPF (R = <i>Pt</i> Pr ₂)	L14	FerroPtBu ₂
L5	XantPhos	L10	<i>R,R</i> -Me-Ferrocene	L15	DMAPF (R = P(NMe ₂) ₂)

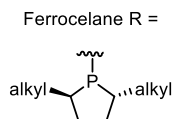
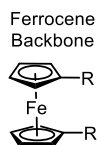


Figure 4.1. General reactivity trends with halogenated pyridines, model reaction and ligand screening outcomes.

evaluated, yielding primarily the conventional bromo-substitution product. The Buchwald class of phosphine ligands was particularly effective in previous Buchwald-Hartwig coupling reactions;⁴ however, only product **4.2** was formed under our conditions. Other monodentate phosphine ligands additionally resulted in the selective bromide addition product with a few exceptions (such as **L1**). Unfortunately, these exceptions resulted in less than 5% yield and could not be optimized further. Bidentate phosphines resulted in a greater diversity of outcomes, including a 3:1 yield of products **4.3:4.2** when 1,1'-bis[di-*tert*-butyl-phosphino]ferrocene (DTBPF, **L7**) was used as a ligand. This result was improved upon by switching the reaction solvent from toluene to 1,4-dioxane. An expanded bidentate ligand set containing ferrocene backbones was evaluated and selectivities for product **4.3** were measured. Interestingly, seven of eight ferrocene backbone ligands promoted the formation of the favored product with a wide range of selectivities (>2.5 kcal/mol difference). This result could possibly indicate an interaction between the ferrocene backbone and the reactive palladium center; however, use of di-*tert*-butyl-phosphino ferrocene (single coordination site, FerroPtBu_2) exclusively yielded product **2** indicating that bis-coordination is a likely cause for selectivity. Unfortunately, DTBPF remained the optimal ligand from the large empirical screen, with only modest selectivity observed (>8:1 ratio of **3:2**), prompting an examination of the observed selectivity trends using linear regression techniques and computational transition state modeling.

Bidentate Ligand Parameterization Background and Application

Fewer parameters have been described for bidentate phosphine ligands than monodentate phosphines (Figure 4.2). The most prominent descriptor is likely the bite angle, a measure of the angle between the two donating phosphorus atoms and the metal acceptor.⁵ This angle was often reported for solid state structures,⁶ and computational chemists continue to use and report this value.⁷ However, the interpretation of the bite angle can be complex due to the presence of both steric and electronic effects, as Freixa and van Leeuwen have demonstrated.⁸ The authors argue that as the bite angle of the phosphine can influence the preferred geometry of the metal, this measure can be viewed as an electronic effect.^{6c} However, the bite angle may also be a measure of steric interactions between the phosphine and the substrate, indicating a steric interaction.⁹ The complex elucidation of the mechanistic role established by a correlation with this parameter indicated that other descriptors may be better suited for our needs.

As parameters from the Fey group had previously been useful in interrogating ligand effects, we elected to explore the ligand knowledge base that had been expanded to include bisphosphines (Figure 4.2).¹⁰ Due to the size of the complexes, the authors chose to study only two organometallic complexes: the $\text{ZnCl}_2(\text{LL})$ and $\text{PdCl}_2(\text{LL})$ complexes, where LL is the bidentate ligand. The Pd complex enforces a fairly rigid square planar geometry, forcing the ligand into a small bite angle near 90° . In contrast, the Zn complex is relatively flexible, enabling much larger angles to be accommodated. Further organometallic complexes were considered but excluded for reasons including partial ligand dissociation and slow convergence times for the computation. Parameters from these complexes were combined with descriptors from the free ligand in two

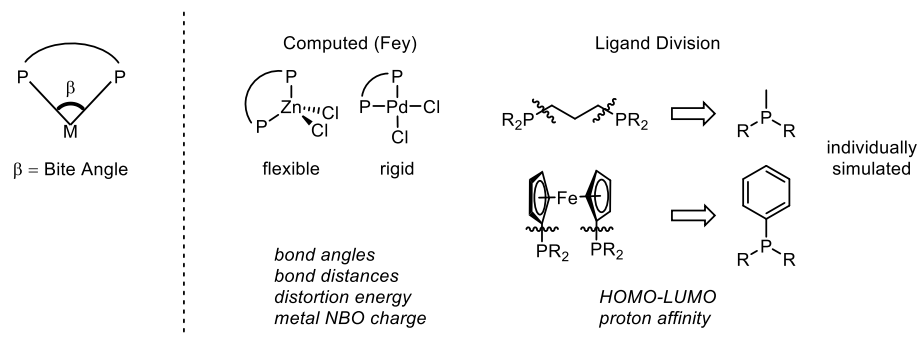


Figure 4.2. Parameters for bidentate phosphines.

geometries. Additionally, the authors chose to split the ligands from the backbone in order to more accurately measure the HOMO and LUMO energies. The structures used for this division were determined according to the backbone: if the atom attached to the phosphorus was an sp^3 carbon, a methyl group was used as a placeholder. If the atom was instead an sp^2 carbon, a phenyl group was instead chosen. This allowed the authors to closely interrogate the role of σ bond donation and π acceptor ability, even in non-symmetric ligands. As a first analysis, the descriptors collected were compared to the bite angles previously reported. The authors found that the P–Zn–P angle was better correlated to the reported bite angles, supporting the hypothesis that this species enables much more variation in structural geometry. However, extensive data sets of bite angles were not previously published, showing the utility of computational descriptors. Furthermore, a comparison within the ligands and descriptors was performed to classify each according to their properties. Follow-up work in 2012 from Fey and coworkers expanded the number of ligands contained in their ligand knowledge base,^{10b} as well as predicted values of possible ligands that may be synthesized (LKB-PP_{screen} 2013).^{10c}

The extensive database from Fey and coworkers enabled linear regression analysis with the outcomes from the model reaction (Figure 4.3). Many reactions resulted in either solely product **4.2** or less than 10% yield, both of which are intractable for our analysis. Therefore, ligands that fell into either category were discarded. A total of seven ligands remained that were represented in the LKB-PP_{screen} from Fey and coworkers. A positive correlation ($R^2 = 0.88$) between the Pd–Cl distance (from the L_2PdCl_2 complex) and the measured selectivities ($\Delta\Delta G^\ddagger$) was identified. This relationship indicated that a possible ligand *trans*-influence (σ -donating ability) may be prevalent in the selectivity

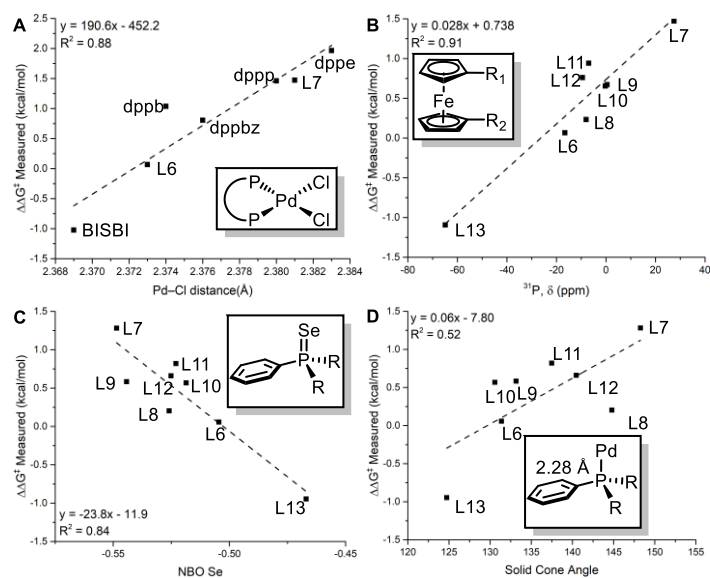


Figure 4.3. Univariate correlations suggest electronic rather than steric interactions dominate selectivity.

determining step. However, the small data set limited the confidence in our interpretation. Given that the 1,1'-ferrocene backbones resulted in a large range of selectivities, additional analyses focused on this ligand class. A second correlation was identified between the ^{31}P NMR shift (δ) and the reaction selectivity, again indicating that ligand electronics were likely important, though steric influences could not be ruled out. To delineate the relative importance of steric and electronic interactions, we initiated a parameterization effort grounded in the previous work we had done with monodentate phosphines and guided by the work from Fey and coworkers. Cleavage of the bisphosphine structures into three portions effectively renders a monodentate phosphine, allowing a single phosphorus donor to be interrogated. As the phosphorus is attached to the ferrocene backbone at $\text{C}(\text{sp}^2)$, the Fey group truncated the structures as phenylIPR_2 . We followed the same protocol followed by calculation of the phosphine oxide and phosphine selenide, due to our success with these structures. Univariate correlations seemed to confirm our hypotheses: the solid cone angle (from the Pd-complex) did not correlate to the measured selectivity ($R^2 = 0.52$) indicating ligand steric effects are not dominant. Conversely, the calculated natural bond orbital (NBO) charge of the Se atom of the phosphine selenides compared favorably to the selectivity ($R^2 = 0.84$). This outcome confirms our hypothesis that σ -donating effects primarily dictate the reaction outcome with more electron donating ligands resulting in higher ratios of the desired product **4.3**. Based on this trend, DTBPF is expected to be the best performing ligand among a virtual screen of dialkyl-ferrocene phosphine structures.

Following the preceding correlations, we considered di-heteroatom-ferrocene phosphine ligands as plausible extensions. Phosponites ($\text{P}(\text{OR})_2\text{R}'$) are considered

uniformly weak σ -donors and strong π -accepting ligands and therefore, we expected this ligand class to perform poorly in our reaction. Conversely, the electronic properties of diamminophosphines are highly tuneable. For example, the Tolman electronic parameter (ν_{CO}) measured for *trans*-L₂Rh(CO)Cl spans from 2007 cm⁻¹ for PhP(pyrrolyl)₂ to 1949 cm⁻¹ for PhP(pyrrolidinyl)₂.¹¹ Fortunately two dialkylamino phosphino ferrocene structures are commercially available: 1,1'-bis[di-(dimethylamino)phosphino]ferrocene (DMAPF) and 1,1'-bis[di-(diethylamino)phosphino]ferrocene (DEAPF). Analysis of the appropriate surrogate structures indicated a possible modest improvement in selectivity according to the Se NBO charge correlation as compared to DTBPF (-0.5505 versus -0.5486). Similarly, the ³¹P NMR shift of DMAPF (95.4 ppm) is significantly downfield compared to DTBPF (27.51 ppm); thus the best model predicts DMAPF would afford a DDG of 3.41 kcal/mol (compared to 1.47 kcal/mol for DTBPF, a >10 fold increase in selectivity). Gratifyingly, Fey and coworkers had computed DMAPF despite the lack of its use in catalysis, and the correlation to Pd-Cl bond distance further supported an increased selectivity of >100:1. Upon testing the DMAPF ligand, we were delighted to find an extremely selective reaction, with >315:1 selectivity ($\Delta\Delta G^\ddagger = 3.93$ kcal/mol) and 95% yield, a dramatic improvement compared to the results from the initial empirical screen.

The phenomenal reactivity observed with DMAPF was exciting synthetically; however, outliers remained, prompting a more detailed analysis. For example, using the simple ³¹P NMR trend above, DEAPF would be expected to be nearly as selective as DMAPF ($\delta = 90.5$ ppm). The isopropyl analog, 1,1'-bis[di-(di-*iso*-propylamino)phosphino]ferrocene (DIPAPF, $\delta = 49.9$) would be expected to result in a

reaction just as selective as DTBPF. Both of these ligands were tested, and neither satisfied expectations (DEAPF $\Delta\Delta G^\ddagger = 2.27$ kcal/mol, DIPAPF $\Delta\Delta G^\ddagger = -1.20$ kcal/mol). Furthermore, we were curious as to the origin of bifurcative outcomes from mono- versus bis-phosphines. To further investigate these questions we chose to pursue computational studies of the presumed selectivity determining step. This work was completed at KAIST under the direction of Mu-Hyun Baik during a research exchange.

Computational Studies of Ligand Promoted Selectivity

To interrogate the aforementioned questions, oxidative addition pathways utilizing four ligand structures were calculated using the B3LYP-D3¹² functional with 6-31G**/LACVP** basis set:¹³ DMAPF, DTBPF, DIPAPF, and the monodentate phosphine FerroPtBu₂. All structures were confirmed to be stationary points via vibrational calculations using cc-pVTZ(-f) basis set¹⁴ (0 imaginary frequencies for ground states, 1 vibrational frequency for transition states) and an implicit solvent correction was applied using $\epsilon = 2.25$ to represent 1,4-dioxane.¹⁵

An initial hypothesis of the loss of selectivity when utilizing the large diaminophosphines (DEAPF and DIPAPF) implicated a plausible hemi-lability of the ligand. Therefore, the energy differences between mono- and bis-ligated structures were measured using the substrate *N*-bound palladium complexes. For the three bisphosphine structures, a significant difference in binding energy was not present ($\Delta G_{\text{DTBPF}} = 9.6$ kcal/mol, $\Delta G_{\text{DMAPF}} = 11.4$ kcal/mol, $\Delta G_{\text{DIPAPF}} = 8.7$ kcal/mol), contradicting the initial hypothesis. Importantly, a PdL₂ complex with monodentate FerroPtBu₂ could not be identified; therefore, a binding energy could not be constructed, indicating the PdL₁

pathway is likely viable when monodentate phosphines are analyzed.

To compare the putative oxidative addition pathways to the C–Cl or C–Br bonds, transition state structures of the bisligated complexes with DMAPF, DTBPF, and DIPAPF were calculated and the monoligated complex with FerroPtBu_2 (Figure 4.4). Relative energies were compared to the measured product ratios via the Curtin-Hammett principle. A direct conversion of the monophosphine product ratio could not be performed as product **4.3** was not isolated. Instead, we expected to see a large barrier difference favoring addition to the C–Br bond. For DTBPF, the experimentally measured energy preference of 1.5 kcal/mol favoring addition to the C–Cl bond compared favorably to the computational difference (**4.6-TS** – **4.5-TS** = $\Delta\Delta G^\ddagger = 1.0$ kcal/mol). DMAPF was calculated to have a 1.9 kcal/mol barrier difference, again favoring **4.5-TS**, in agreement with the experimentally identified trend ($\Delta\Delta G^\ddagger = 3.9$ kcal/mol). Fortunately, DIPAPF was correctly calculated to have a small preference along the **4.6-TS** pathway ($\Delta\Delta G^\ddagger = 0.9$ kcal/mol). Additionally, monophosphine FerroPtBu_2 was correctly calculated to react with the C–Br bond with a large barrier difference of 5.0 kcal/mol (**4.5-TS** – **4.6-TS**).

Having established that the selectivity trends are correctly represented in the calculated reaction pathways, interrogation of the origin of selectivity commenced using the distortion/interaction analysis developed by the Houk and Bickelhaupt groups (Figure 4.5).¹⁶ The bisphosphine ligands compressed during the oxidative addition step as expected; for example, the P–Pd–P angle (bite angle) drops significantly for each ligand, regardless of the oxidative addition position. DTBPF goes from a measured ligand bite angle of 119° in the starting material (**4.4**) to 105° in both addition products (**4.5** and **4.6**).

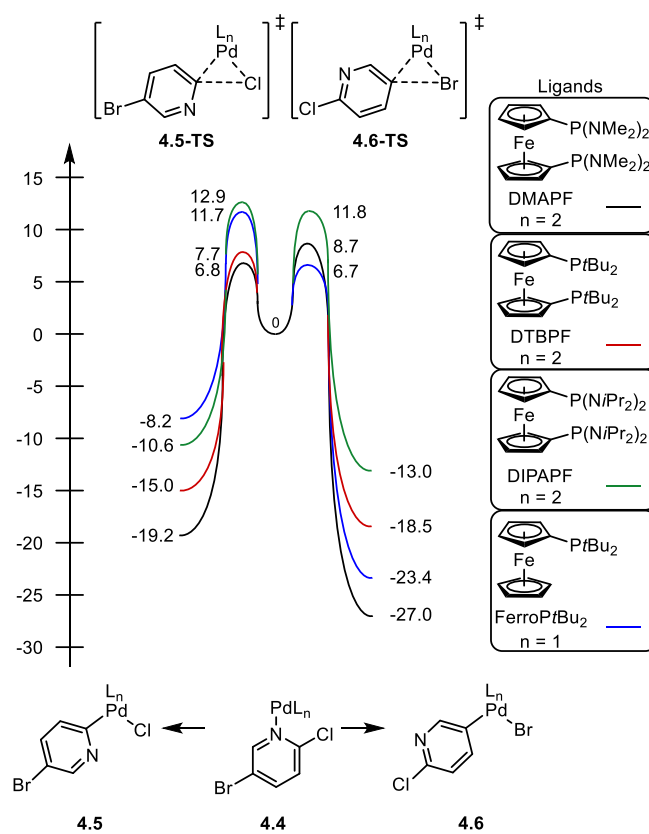


Figure 4.4. Oxidative addition energy profile with four ligands.

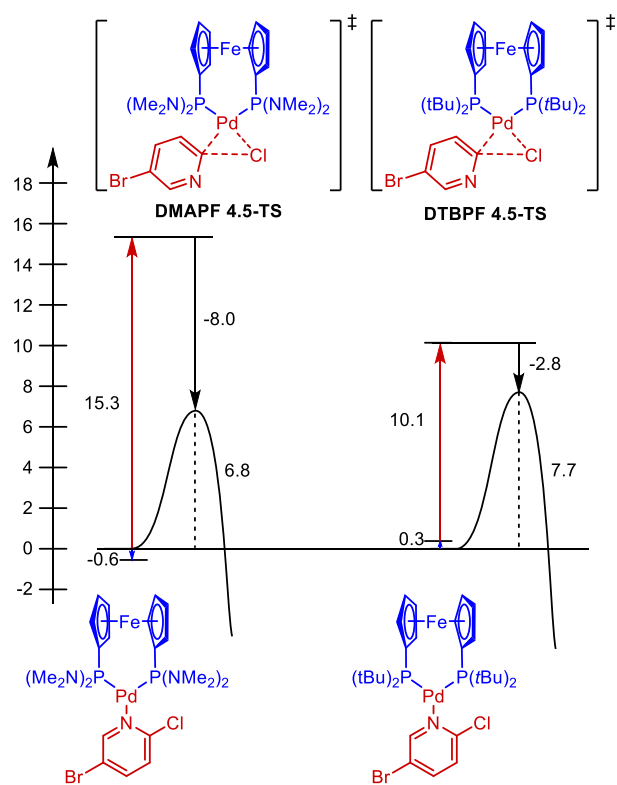


Figure 4.5. Distortion-interaction differences between DMAPF and DTBPF indicating a more strained Pd-aryl species.

DMAPF starts at a slightly smaller angle (116°) and compresses to 99° for addition to the C–Cl bond (**4.5**) or 106° for addition to the C–Br bond (**4.6**). However, neither of these ligands requires large amounts of energy to perform this compression as the two cyclopentadiene (cp) rings can rotate about the iron center. The strain energy of DTBPF is 0.3 kcal/mol in **4.5-TS** and 1.3 kcal/mol in **4.6-TS**. DMAPF has a 0.6 kcal/mol lower energy in **4.5-TS** and 1.3 kcal/mol higher energy in **4.6-TS**. These small energy differences highlight the utility of the flexible ferrocene ligand class in this reaction, and could be interpreted as the origin of the selectivity difference between DMAPF and DTBPF. However, much more drastic differences between ligands were identified when comparing the Pd-Aryl strain and interaction energies. In DMAPF **4.5-TS** a much more distorted Pd-Aryl species is present in comparison to DTBPF **4.5-TS** (15.3 kcal/mol versus 10.2 kcal/mol). This energy penalty is countered by a stronger interaction with DMAPF (-8.0 kcal/mol) versus DTBPF (-2.8 kcal/mol). Overall, these outcomes are consistent with DMAPF being more electron donating, resulting in a more nucleophilic palladium, in agreement with the univariate correlations identified previously.

Having confirmed the experimentally proposed trends with DMAPF and DTBPF, we turned our attention to FerroPtBu_2 and DIPAPF. Visual inspection of DMAPF **4.5-TS** and DTBPF **4.5-TS** suggested that the pyridine nitrogen may interact with the palladium in this transition state, lowering the barrier to oxidative addition at the adjacent C–Cl bond (Figure 4.6). In comparison, neither DIPAPF **4.5-TS** nor FerroPtBu_2 **4.5-TS** includes this proposed interaction, resulting in significantly higher energy pathways. In DIPAPF, the dramatically larger $\text{P}(\text{NiPr}_2)_2$ groups do not allow the pyridine substrate to approach the palladium close enough to engage with the nitrogen lone pair. The loss of

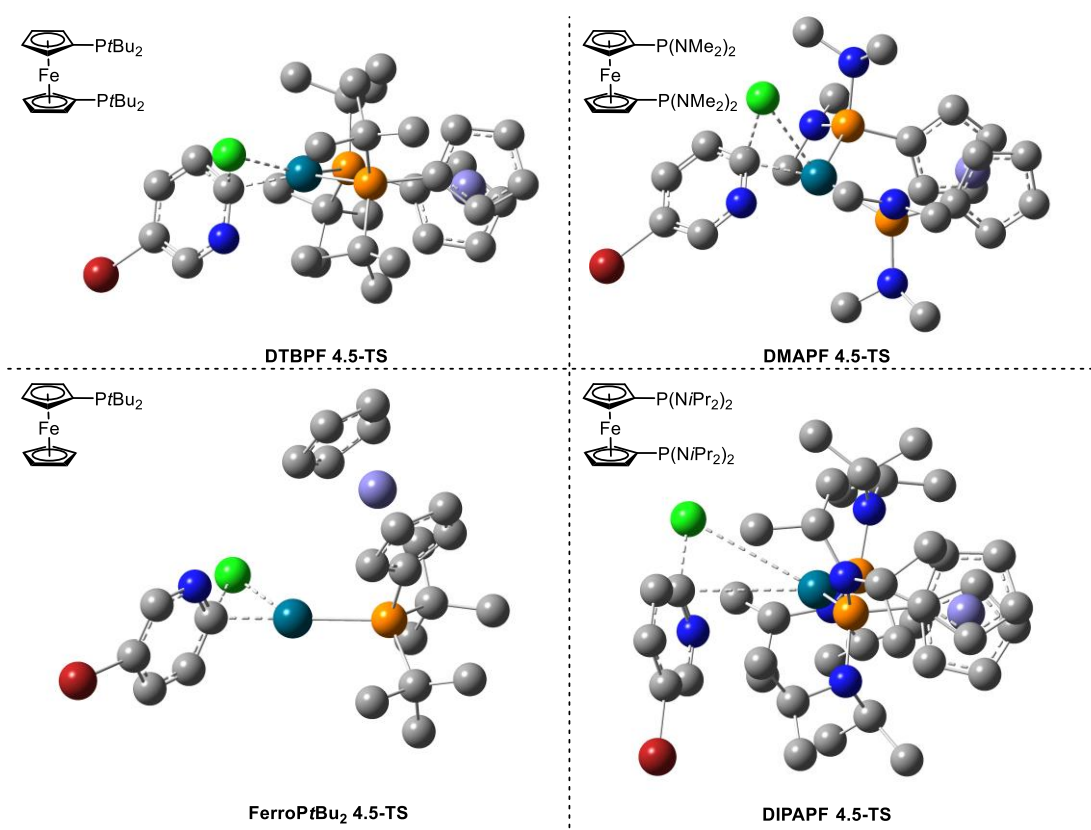


Figure 4.6. Transition state structures from the four ligands interrogated. Hydrogens removed for clarity. Atom colors: grey = C, red = Br, green = Cl, dark blue = N, orange = P, teal = Pd, purple = Fe.

this stabilizing interaction raises the energy of **4.5-TS**, resulting in addition to the C–Br bond being favored. With FerroPtBu_2 , the pyridine nitrogen again does not interact with the palladium as the forming bond is oriented orthogonal to the nitrogen lone pair. This outcome is likely due to mono- versus bis-ligation, which is hypothesized to affect the *d*-orbital orientations. Further work is ongoing to confirm this hypothesis.

Reaction Scope and Conclusions

Concurrent to the theoretical mechanistic investigations, the Novartis team pursued the exploration of the reaction scope (Figure 4.7). Using the highly selective catalyst system identified with DMAPF, a broad range of substrates were effectively reacted. Numerous pyridine heterocycles were tolerated, including substrates in which the 2-position was electronically deactivated (**4.7a**) or sterically encumbered (**4.7a-e**) compared to the bromide. Substitution at the 4 (**4.9**) and 6 (**4.10**) positions adjacent to the Br enhanced the coupling at the 2-Cl. The trihalogenated precursor to **4.10** coupled with complete selectivity at the 2-position, and the regioisomeric precursor to **4.11** coupled with moderate preference for the more hindered chloride. Pleasingly, 3-bromo-2-chloropyridine derivatives (**4.12a-e**) also coupled with moderate yields and selectivities under the optimized conditions. Most impressively, product **4.15** is formed with reasonable selectivity despite the presence of two bromides.

Various amine coupling partners were additionally evaluated, with broad tolerance displayed. Substituted anilines bearing steric and electronic perturbations performed well (**4.16a-e**, **4.17a-d**), and primary and secondary amines were generally high-yielding and selective. Intriguingly, potentially useful compounds such as **18** could

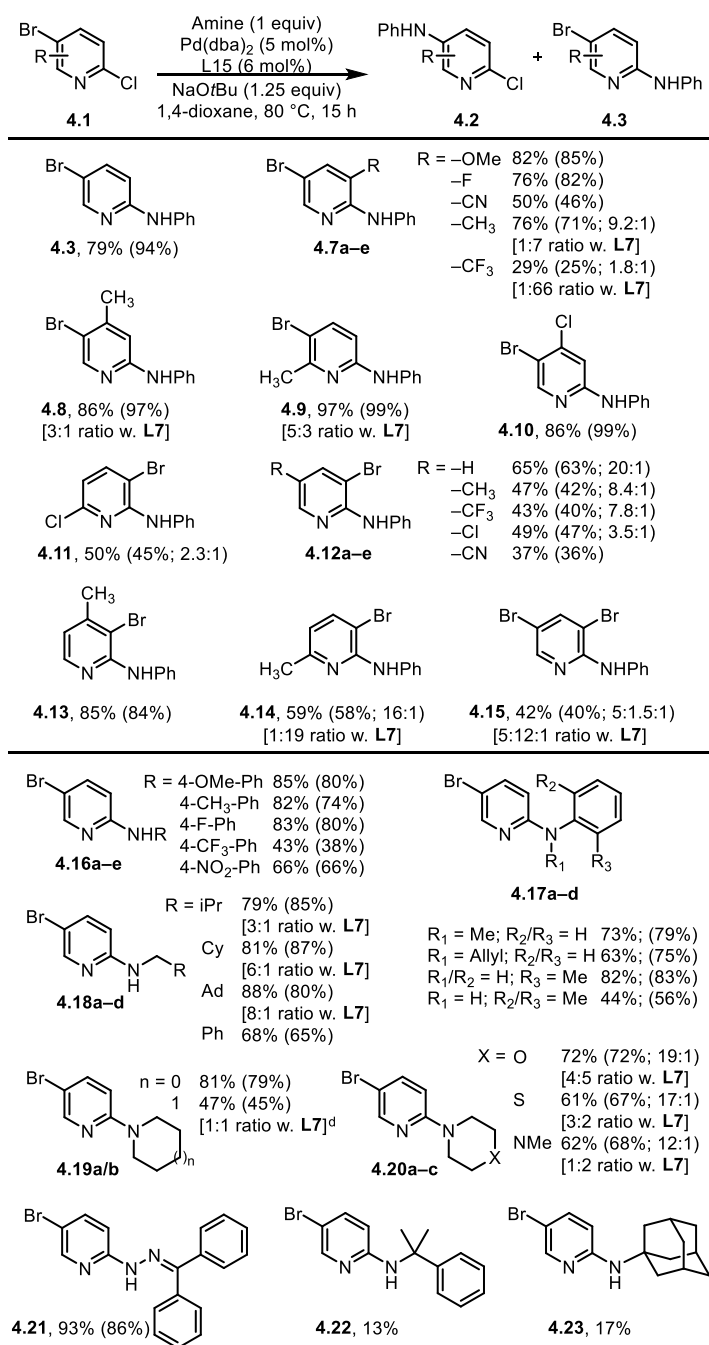


Figure 4.7. Reaction scope. Major product drawn.

readily be formed, allowing facile access to its hydrolysis product. Finally, the coupling of hindered α,α,α -trisubstituted primary amines occurs under the current conditions, albeit in low yields.

In summary, a 2-Cl-selective coupling of multiply halogenated pyridine heterocycles has been achieved through the use of palladium-bisphosphine catalysis. The use of linear regression analysis of truncated model ligands yielded relevant structure-selectivity models, allowing for extrapolation to an unexplored ligand. The unique selectivity of DMAPF under the reaction conditions was interrogated using DFT methods to quantify the origin of the empirical result. The calculations suggest that mono- versus bis-ligation influences the orbital orientation, resulting in the stabilization of the 2-selective pathway with bis-ligated phosphines. Overall, this workflow enabled the identification of an entirely non-intuitive extrapolation, a method that will be applied to future studies.

Experimental

All experimental work was completed at Novartis by Mitch Keylor so only computational data is presented here.

Phosphine oxide structures were optimized in Gaussian 09¹⁷ with M06-2x and def2-TZVP to match previous work.¹⁸ Input geometries contained the phenyl ring parallel to the P=O bond. Solid cone angles were measured in Solid-G¹⁹ by replacing the oxygen with a palladium atom and setting the P–Pd bond distance to 2.28 Å. Phosphine selenide structures were computed at the same level of theory in Gaussian 09 using the output file from the phosphine oxide structures and replacing the oxygen for selenium. NBO charges

were calculated using NBO 6 as implemented in Gaussian 09.²⁰ Table 4.1 contain all data used in Figure 4.3.

DFT Computational Details

All calculations were performed using density functional theory²¹ as implemented in the Jaguar 9.1 suite of ab initio quantum chemistry programs.²² Geometry optimizations were performed with the B3LYP-D3 functional¹² using the 6-31G**/LACVP** basis set.¹³ Single point energies were computed from the optimized geometries using Dunning's correlation-consistent triple- ζ basis set (cc-pVTZ(-f)¹⁴) that includes a double set of polarization functions. Vibrational frequencies were computed at the B3LYP-D3/6-31G** level of theory were used to derive zero point energy and vibrational entropy corrections from unscaled frequencies. Solvation energies were evaluated by a self-consistent reaction field (SCRF) approach with the dielectric constant $\epsilon = 2.25$ (1,4-dioxane) using the optimized gas phase structures.¹⁵ Gibbs energy was calculated according to the formula $G = (E(\text{SCF}) * 23.0605423 + \text{ZPE}) - 353.15 * S + G(\text{solv})$. ΔG is compared to **4.4** for each ligand. All energies from these calculations are reported in Table 4.2.

Table 4.1. Data for Figure 4.3.

Phosphine	4.3 yield	4.2 yield	$\Delta\Delta G^\ddagger$ kcal/mol	Cone Angle ($^\circ$)	Se NBO charge	^{31}P NMR (δ)
DPPF	33.6	30.5	0.066	131.38	-0.50454	-16.6
DIPPF	59.5	22.2	0.672	133.16	-0.54427	0.5
DTBPF	67.9	7.8	1.475	148.27	-0.54855	27.5
DCYPF	37.8	26.8	0.234	144.80	-0.52593	-8.0
DMAPF	94.2	0.3	3.928	133.83	-0.55051	95.4
DEAPF	84.9	3.0	2.278	148.23	-0.55550	90.5
DIPAPF	2.0	11.7	-1.204	159.38	-0.56195	49.9
Hiersophos	4.6	22.7	-1.088	124.73	-0.46701	-64.9
Me-Ferrocene	15.9	6.1	0.653	130.58	-0.51863	-0.3
Et-Ferrocene	45.1	11.3	0.943	137.49	-0.52303	-7.0
<i>i</i> Pr-Ferrocene	58.8	19.3	0.759	140.46	-0.52515	-9.5

Phosphine	Pd–Cl distance (\AA)	$\Delta\Delta G^\ddagger$ kcal/mol
DPPF	2.373	0.067
DTBPF	2.381	1.472
Diphenylphosphino ethane (dppe)	2.383	1.966
Diphenylphosphino benzene (dppbz)	2.376	0.806
Diphenylphosphino propane (dppp)	2.380	1.462
Diphenylphosphino butane (dppb)	2.374	1.037
2,2'-Bis(diphenylphosphinomethyl)- 1,1'-biphenyl (BISBI)	2.369	-1.022

Table 4.2. Computational energy data.

Structure	E(SCF) (eV)	ZPE (kcal/mol)	S (cal/mol)	G(solv) (kcal/mol)	ΔG (kcal/mol)
DTBPF 4.4	-72690.817	449.80	256.04	-2.64	0.00
DTBPF 4.5-TS	-72690.345	447.65	254.76	-4.14	7.69
DTBPF 4.5	-72691.565	451.47	244.56	-6.09	-14.98
DTBPF 4.6-TS	-72690.521	450.26	246.30	-4.72	8.65
DTBPF 4.6	-72691.662	451.76	245.12	-7.42	-18.45
DTBPF mono ligated	-72690.266	449.74	261.19	-3.85	9.62
DMAPF 4.4	-70155.973	348.86	244.20	-3.29	0.00
DMAPF 4.5-TS	-70155.712	349.13	235.11	-6.00	6.79
DMAPF 4.5	-70156.882	350.74	232.37	-7.57	-19.19
DMAPF 4.6-TS	-70155.715	349.34	232.22	-5.27	8.68
DMAPF 4.6	-70157.086	350.23	238.50	-8.04	-27.03
DMAPF mono ligated	-70155.339	349.14	251.94	-4.05	11.41
DIPAPF 4.4	-87278.741	636.29	317.58	-2.57	0.00
DIPAPF 4.5-TS	-87278.263	636.10	310.79	-2.86	12.94
DIPAPF 4.5	-87279.299	637.99	308.42	-5.24	-10.60
DIPAPF 4.6-TS	-87278.305	636.95	308.99	-4.54	11.78
DIPAPF 4.6	-87279.411	638.79	305.99	-6.69	-12.98
DIPAPF mono ligated	-87278.150	635.44	326.87	-3.38	8.69
FerroPtBu₂ 4.4	-54822.754	300.39	207.86	-3.02	0.00
FerroPtBu₂ 4.5-TS	-54822.249	299.49	203.04	-3.81	11.66
FerroPtBu₂ 4.5	-54823.067	300.30	206.34	-4.49	-8.24
FerroPtBu₂ 4.6-TS	-54822.505	299.84	200.79	-4.03	6.68
FerroPtBu₂ 4.6	-54823.617	300.76	204.67	-7.99	-23.37

References

1. Almond-Thynne, J.; Blakemore, D. C.; Pryde, D. C.; Spivey, A. C., Site-Selective Suzuki-Miyaura Coupling of Heteroaryl Halides - Understanding the Trends for Pharmaceutically Important Classes. *Chem. Sci.* **2017**, *8* (1), 40-62.
2. (a) Ji, J.; Li, T.; Bunnelle, W. H., Selective Amination of Polyhalopyridines Catalyzed by a Palladium–Xantphos Complex. *Org. Lett.* **2003**, *5* (24), 4611-4614; (b) Herrebout, W. A.; Nagels, N.; Verbeeck, S.; van der Veken, B. J.; Maes, B. U. W., A DFT Study of Site-Selectivity in Oxidative Addition Reactions with Pd0 Complexes: The Effect of an Azine Nitrogen and the Use of Different Types of Halogen Atoms in the Substrate. *Eur. J. Org. Chem.* **2010**, *2010* (16), 3152-3158.
3. (a) Dai, X.; Chen, Y.; Garrell, S.; Liu, H.; Zhang, L.-K.; Palani, A.; Hughes, G.; Nargund, R., Ligand-Dependent Site-Selective Suzuki Cross-Coupling of 3,5-Dichloropyridazines. *J. Org. Chem.* **2013**, *78* (15), 7758-7763; (b) Ashcroft, C. P.; Fussell, S. J.; Wilford, K., Catalyst Controlled Regioselective Suzuki Cross-Coupling of 2-(4-bromophenyl)-5-chloropyrazine. *Tetrahedron Lett.* **2013**, *54* (34), 4529-4532; (c) Strotman, N. A.; Chobanian, H. R.; He, J.; Guo, Y.; Dormer, P. G.; Jones, C. M.; Steves, J. E., Catalyst-Controlled Regioselective Suzuki Couplings at Both Positions of Dihaloimidazoles, Dihaloazoles, and Dihalthiazoles. *J. Org. Chem.* **2010**, *75* (5), 1733-1739; (d) Cheng, J.; Trudell, M. L., Synthesis of N-Heteroaryl-7-azabicyclo[2.2.1]heptane Derivatives via Palladium–Bisimidazol-2-ylidene Complex Catalyzed Amination Reactions. *Org. Lett.* **2001**, *3* (9), 1371-1374.
4. (a) Wolfe, J. P.; Buchwald, S. L., A Highly Active Catalyst for the Room-Temperature Amination and Suzuki Coupling of Aryl Chlorides. *Angew. Chem. Int. Ed.* **1999**, *38* (16), 2413-2416; (b) Barder, T. E.; Walker, S. D.; Martinelli, J. R.; Buchwald, S. L., Catalysts for Suzuki–Miyaura Coupling Processes: Scope and Studies of the Effect of Ligand Structure. *J. Am. Chem. Soc.* **2005**, *127* (13), 4685-4696.
5. (a) van Leeuwen, P. W. N. M.; Kamer, P. C. J.; Reek, J. N. H.; Dierkes, P., Ligand Bite Angle Effects in Metal-catalyzed C–C Bond Formation. *Chem. Rev.* **2000**, *100* (8), 2741-2770; (b) Birkholz, M.-N.; Freixa, Z.; van Leeuwen, P. W. N. M., Bite Angle Effects of Diphosphines in C-C and C-X Bond Forming Cross Coupling Reactions. *Chem. Soc. Rev.* **2009**, *38* (4), 1099-1118.
6. (a) Dierkes, P.; W. N. M. van Leeuwen, P., The Bite Angle Makes the Difference: a Practical Ligand Parameter for Diphosphine Ligands. *J. Chem. Soc., Dalton Trans.* **1999**, (10), 1519-1530; (b) van Haaren, R. J.; Goubitz, K.; Fraanje, J.; van Strijdonck, G. P. F.; Oevering, H.; Coussens, B.; Reek, J. N. H.; Kamer, P. C. J.; van Leeuwen, P. W. N. M., An X-ray Study of the Effect of the Bite Angle of Chelating Ligands on the Geometry of Palladium(allyl) Complexes: Implications for the Regioselectivity in the Allylic Alkylation. *Inorg. Chem.* **2001**, *40* (14), 3363-3372; (c) Hayashi, T.; Konishi, M.; Kobori, Y.; Kumada, M.; Higuchi, T.; Hirotsu, K., Dichloro[1,1'-Bis(diphenylphosphino)ferrocene]palladium(II): An Effective Catalyst for Cross-

Coupling of Secondary and Primary Alkyl Grignard and Alkylzinc Reagents with Organic Halides. *J. Am. Chem. Soc.* **1984**, *106* (1), 158-163; (d) Casey, C. P.; Whiteker, G. T.; Melville, M. G.; Petrovich, L. M.; Gavney, J. A.; Powell, D. R., Diphosphines with Natural Bite Angles Near 120° Increase Selectivity for n-Aldehyde Formation in Rhodium-Catalyzed Hydroformylation. *J. Am. Chem. Soc.* **1992**, *114* (14), 5535-5543; (e) Kranenburg, M.; Kamer, P. C. J.; van Leeuwen, P. W. N. M.; Vogt, D.; Keim, W., Effect of the Bite Angle of Diphosphine Ligands on Activity and Selectivity in the Nickel-Catalysed Hydrocyanation of Styrene. *J. Chem. Soc., Chem. Commun.* **1995**, (21), 2177-2178; (f) Hofmann, P.; Perez-Moya, L. A.; Steigelmann, O.; Riede, J., η -2-(C,O) Ketene Coordination at Nickel(O). Synthesis, Bonding, and Molecular Structure of (dtbpm)Ni[η -2-(C,O)-Ph₂C₂O] [dtbpm = Bis(di-tert-butylphosphino)methane]. *Organometallics* **1992**, *11* (3), 1167-1176; (g) Stradiotto, M.; Lundgren, R. J.; Buchwald, S. L.; Milstein, D., *Ligand Design in Metal Chemistry: Reactivity and Catalysis*. Wiley: 2016.

7. (a) Flener Lovitt, C.; Frenking, G.; Girolami, G. S., Donor–Acceptor Properties of Bidentate Phosphines. DFT Study of Nickel Carbonyls and Molecular Dihydrogen Complexes. *Organometallics* **2012**, *31* (11), 4122-4132; (b) Daniels, D. S. B.; Jones, A. S.; Thompson, A. L.; Paton, R. S.; Anderson, E. A., Ligand Bite Angle-Dependent Palladium-Catalyzed Cyclization of Propargylic Carbonates to 2-Alkynyl Azacycles or Cyclic Dienamides. *Angew. Chem. Int. Ed.* **2014**, *53* (7), 1915-1920.

8. Freixa, Z.; van Leeuwen, P. W. N. M., Bite Angle Effects in Diphosphine Metal Catalysts: Steric or Electronic? *Dalton transactions* **2003**, (10), 1890-1901.

9. Carbó, J. J.; Maseras, F.; Bo, C.; van Leeuwen, P. W. N. M., Unraveling the Origin of Regioselectivity in Rhodium Diphosphine Catalyzed Hydroformylation. A DFT QM/MM Study. *J. Am. Chem. Soc.* **2001**, *123* (31), 7630-7637.

10. (a) Fey, N.; Harvey, J. N.; Lloyd-Jones, G. C.; Murray, P.; Orpen, A. G.; Osborne, R.; Purdie, M., Computational Descriptors for Chelating P,P- and P,N-Donor Ligands I. *Organometallics* **2008**, *27* (7), 1372-1383; (b) Jover, J.; Fey, N.; Harvey, J. N.; Lloyd-Jones, G. C.; Orpen, A. G.; Owen-Smith, G. J. J.; Murray, P.; Hose, D. R. J.; Osborne, R.; Purdie, M., Expansion of the Ligand Knowledge Base for Chelating P,P-Donor Ligands (LKB-PP). *Organometallics* **2012**, *31* (15), 5302-5306; (c) Jover, J.; Fey, N., Screening Substituent and Backbone Effects on the Properties of Bidentate P,P-Donor Ligands (LKB-PPscreen). *Dalton Trans.* **2013**, *42* (1), 172-181.

11. (a) Moloy, K. G.; Petersen, J. L., N-Pyrrolyl Phosphines: An Unexploited Class of Phosphine Ligands with Exceptional π -Acceptor Character. *J. Am. Chem. Soc.* **1995**, *117* (29), 7696-7710; (b) Clarke, M. L.; Cole-Hamilton, D. J.; Slawin, A. M. Z.; Woollins, J. D., P-N Bond Formation as a Route to Highly Electron Rich Phosphine Ligands. *Chem. Commun.* **2000**, (20), 2065-2066.

12. (a) Slater, J. C., *Quantum Theory of Molecules and Solids : v4: the Self-Consistent Field for Molecules and Solids*. Mc-Graw-Hill: New York, 1974; (b) Vosko,

S. H.; Wilk, L.; Nusair, M., Accurate Spin-Dependent Electron Liquid Correlation Energies for Local Spin Density Calculations: a Critical Analysis. *Can. J. Phys.* **1980**, *58* (8), 1200-1211; (c) Becke, A. D., Density-Functional Exchange-Energy Approximation with Correct Asymptotic Behavior. *Phys. Rev. A* **1988**, *38* (6), 3098-3100; (d) Lee, C.; Yang, W.; Parr, R. G., Development of the Colle-Salvetti Correlation-Energy Formula into a Functional of the Electron Density. *Phys. Rev. B* **1988**, *37* (2), 785-789; (e) Grimme, S.; Antony, J.; Ehrlich, S.; Krieg, H., A Consistent and Accurate Ab Initio Parametrization of Density Functional Dispersion Correction (DFT-D) for the 94 Elements H-Pu. *J. Chem. Phys.* **2010**, *132* (15), 154104.

13. (a) Hay, P. J.; Wadt, W. R., Ab Initio Effective Core Potentials for Molecular Calculations. Potentials for the Transition Metal Atoms Sc to Hg. *J. Chem. Phys.* **1985**, *82* (1), 270-283; (b) Wadt, W. R.; Hay, P. J., Ab Initio Effective Core Potentials for Molecular Calculations. Potentials for Main Group Elements Na to Bi. *J. Chem. Phys.* **1985**, *82* (1), 284-298; (c) Hay, P. J.; Wadt, W. R., Ab Initio Effective Core Potentials for Molecular Calculations. Potentials for K to Au Including the Outermost Core Orbitals. *J. Chem. Phys.* **1985**, *82* (1), 299-310.

14. Jr., T. H. D., Gaussian Basis Sets for Use in Correlated Molecular Calculations. I. The Atoms Boron Through Neon and Hydrogen. *J. Chem. Phys.* **1989**, *90* (2), 1007-1023.

15. (a) Marten, B.; Kim, K.; Cortis, C.; Friesner, R. A.; Murphy, R. B.; Ringnalda, M. N.; Sitkoff, D.; Honig, B., New Model for Calculation of Solvation Free Energies: Correction of Self-Consistent Reaction Field Continuum Dielectric Theory for Short-Range Hydrogen-Bonding Effects. *J. Phys. Chem.* **1996**, *100* (28), 11775-11788; (b) Friedrichs, M.; Zhou, R.; Edinger, S. R.; Friesner, R. A., Poisson-Boltzmann Analytical Gradients for Molecular Modeling Calculations. *J. Phys. Chem. B* **1999**, *103* (16), 3057-3061; (c) Edinger, S. R.; Cortis, C.; Shenkin, P. S.; Friesner, R. A., Solvation Free Energies of Peptides: Comparison of Approximate Continuum Solvation Models with Accurate Solution of the Poisson-Boltzmann Equation. *J. Phys. Chem. B* **1997**, *101* (7), 1190-1197.

16. Bickelhaupt, F. M.; Houk, K. N., Analyzing Reaction Rates with the Distortion/Interaction-Activation Strain Model. *Angew. Chem. Int. Ed.* **2017**, *56* (34), 10070-10086.

17. Frisch, M. J.; Trucks, G. W.; Schlegel, H. B.; Scuseria, G. E.; Robb, M. A.; Cheeseman, J. R.; Scalmani, G.; Barone, V.; Mennucci, B.; Petersson, G. A.; Nakatsuji, H.; Caricato, M. L.; X.; Hratchian, H. P.; Izmaylov, A. F.; Bloino, J.; Zheng, G.; Sonnenberg, J. L.; Hada, M.; Ehara, M.; Toyota, K.; Fukuda, R.; Hasegawa, J.; Ishida, M.; Nakajima, T.; Honda, Y.; Kitao, O.; Nakai, H.; Vreven, T.; Montgomery, J. A., Jr.; Peralta, J. E.; Ogliaro, F.; Bearpark, M.; Heyd, J. J.; Brothers, E.; Kudin, K. N.; Staroverov, V. N.; Kobayashi, R.; Normand, J.; Raghavachari, K.; Rendell, A.; Burant, J. C.; Iyengar, S. S.; Tomasi, J.; Cossi, M.; Rega, N.; Millam, N. J.; Klene, M.; Knox, J. E.; Cross, J. B.; Bakken, V.; Adamo, C.; Jaramillo, J.; Gomperts, R.; Stratmann, R. E.; Yazyev, O.; Austin, A. J.; Cammi, R.; Pomelli, C.; Ochterski, J. W.; Martin, R. L.;

Morokuma, K.; Zakrzewski, V. G.; Voth, G. A.; Salvador, P.; Dannenberg, J. J.; Dapprich, S.; Daniels, A. D.; Farkas, Ö.; Foresman, J. B.; Ortiz, J. V.; Cioslowski, J.; Fox, D. J. *Gaussian 09, Revision D.01*, Gaussian, Inc.: Wallingford, CT, 2009.

18. (a) Zhao, Y.; Truhlar, D., The M06 Suite of Density Functionals for Main Group Thermochemistry, Thermochemical Kinetics, Noncovalent Interactions, Excited States, and Transition Elements: Two New Functionals and Systematic Testing of Four M06-Class Functionals and 12 Other Functionals. *Theor. Chem. Acc.* **2008**, *120* (1-3), 215-241; (b) Weigend, F.; Ahlrichs, R., Balanced Basis Sets of Split Valence, Triple Zeta Valence and Quadruple Zeta Valence Quality for H to Rn: Design and Assessment of Accuracy. *PCCP* **2005**, *7* (18), 3297-3305.

19. Guzei, I. A.; Wendt, M., An Improved Method for the Computation of Ligand Steric Effects Based on Solid Angles. *Dalton Trans.* **2006**, (33), 3991-3999.

20. Glendening, E. D.; Landis, C. R.; Weinhold, F., NBO 6.0: Natural Bond Orbital Analysis Program. *J. Comput. Chem.* **2013**, *34* (16), 1429-1437.

21. Parr, R. G.; Weitao, Y., *Density-Functional Theory of Atoms and Molecules*. Oxford University Press: 1994.

22. Bochevarov, A. D.; Harder, E.; Hughes, T. F.; Greenwood, J. R.; Braden, D. A.; Philipp, D. M.; Rinaldo, D.; Halls, M. D.; Zhang, J.; Friesner, R. A., Jaguar: A High-Performance Quantum Chemistry Software Program with Strengths in Life and Materials Sciences. *Int. J. Quantum Chem.* **2013**, *113* (18), 2110-2142.

CHAPTER 5

QUANTIFICATION OF ACYCLIC DIAMINO CARBENE LIGAND EFFECTS IN A GOLD(I) CATALYZED ISOMERIZATION- CYCLIZATION

Concurrent to the studies of gold catalysis presented in Chapter 2, we were presented with an opportunity to explore a recently developed class of carbene ligands with the Toste team. This ligand class had been reported previously for rendering three reactions enantioselective with moderate success. The range of enantiomeric excess was broad for a reaction that the Toste lab had been working to develop, yet they had been unable to increase the selectivity to useful levels. Thus, our groups decided to expand the collaboration to develop new parameters to describe this ligand class with the goal of better understanding the roles the ligand plays in imparting enantioselectivity. The totality of this project is encapsulated in this chapter. It is important to note that Dmitri Krakhovsky and Suresh Pindi performed all experiments.

Introduction

Gold catalysis has rapidly expanded over the previous decade, as noted in Chapter 3.¹ This expansion has been enabled by diverse ligand structures, notably phosphines² and carbenes.³ However, enantioselective gold-catalyzed reactions have generally relied

on phosphorus ligands,⁴ as carbene ligands are limited by their “fence-like” structure, which orients the “arms” of the ligands away from the reaction site.⁵ Additionally, relatively few parameters are known for carbene ligands, dominated by the Tolman electronic parameter, percent buried volume, and bond dissociation energies.⁶ These parameters offer limited insight into the controlling features of this ligand class, resulting in few enantioselective transition metal-catalyzed transformations utilizing carbenes.⁷

However, there is recent work from multiple groups that has started to identify structural motifs of carbene ligands that can induce useable levels of enantioselectivity in homogeneous gold catalysis (Figure 5.1). The Espinet group identified acyclic diamino carbenes as possible carbene ligand structures, testing the organogold complexes in two reactions.⁸ The first, an enantioselective cyclopropanation of styrene derivatives yielded a maximum of 24% ee with a carbene ligand. The second, an enantioselective hydroalkoxylation of an allene, resulted in a maximum ee of 22%. Both of these results were significantly improved with (S)-DTBM-SEGPHOS, a phosphorus ligand. Fortunately, further development of this structural motif by the Slaughter⁹ and Toste groups¹⁰ has revealed ligand structures that have resulted in high enantioselectivity in gold carbene catalyzed reactions.

Specifically, the Toste lab has focused their efforts on acyclic diaminocarbene (ADC) ligands with appended aryl groups at the 3,3' positions of the ligand backbone to attenuate the enantioselectivity. Their initial report utilizing this ligand class unveiled a dynamic kinetic asymmetric cyclization of propargyl esters.^{10a} Presumably, this reaction proceeds through an initial [3,3] rearrangement of propargyl esters, resulting in the generation of allenes. This intermediate can interact with the cationic gold to produce an

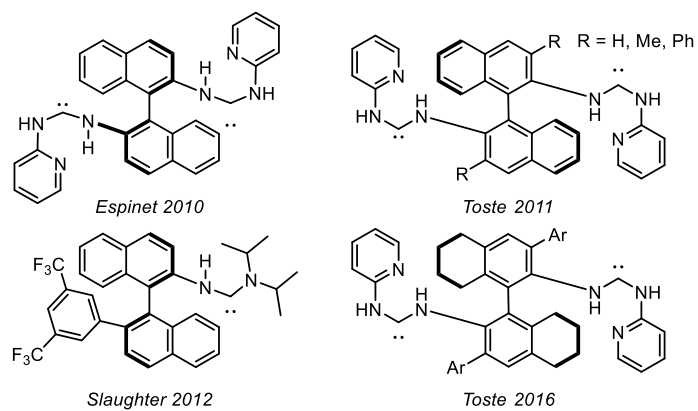


Figure 5.1. Diamino carbene ligands utilized by various groups.

achiral intermediate that can be trapped by the pendant phenol nucleophile. Variations about the 3,3' aryl group on the binaphthyl backbone allowed the group to quickly identify an appropriate ligand for this transformation. Following this disclosure, the group was able to report conditions that yield allylic amines or allylic azides starting from the appropriate allene.^{10b} However, each of these reactions necessitated the use of a different optimal ligand structure. Further applications using this ligand class were limited by the lack of information of the structural effects of the molecular framework.

Therefore, the goals of the study were twofold: first, could we identify molecular parameters to interrogate structure selectivity effects, and second, could these be applied to a novel reaction to render it enantioselective. We elected to study a tandem [3,3]-sigmatropic rearrangement-[2+2]-cyclization reaction of propargyl esters that had previously only been published as a racemic variant.¹¹ This reaction furnishes a highly functionalized heterocycle, making an enantioselective reaction attractive. The models derived offer insight into the origin of selectivity and simultaneously build a foundation to improve asymmetric catalysis.

Development and Analysis of Descriptors for ADC Catalysts

Initial efforts were aimed at building a training set for analysis (Figure 5.2). The ADC ligands are highly variable, though differences had focused on two areas. The 3,3' positions of the ligand backbone had been essential in controlling selectivity in previous reactions; therefore, substitution about the aryl groups included both electron donating and withdrawing substituents. Additionally, the pyridine portion was interchangeable through the use of commercial pyridines that included a 2-amino group. Other

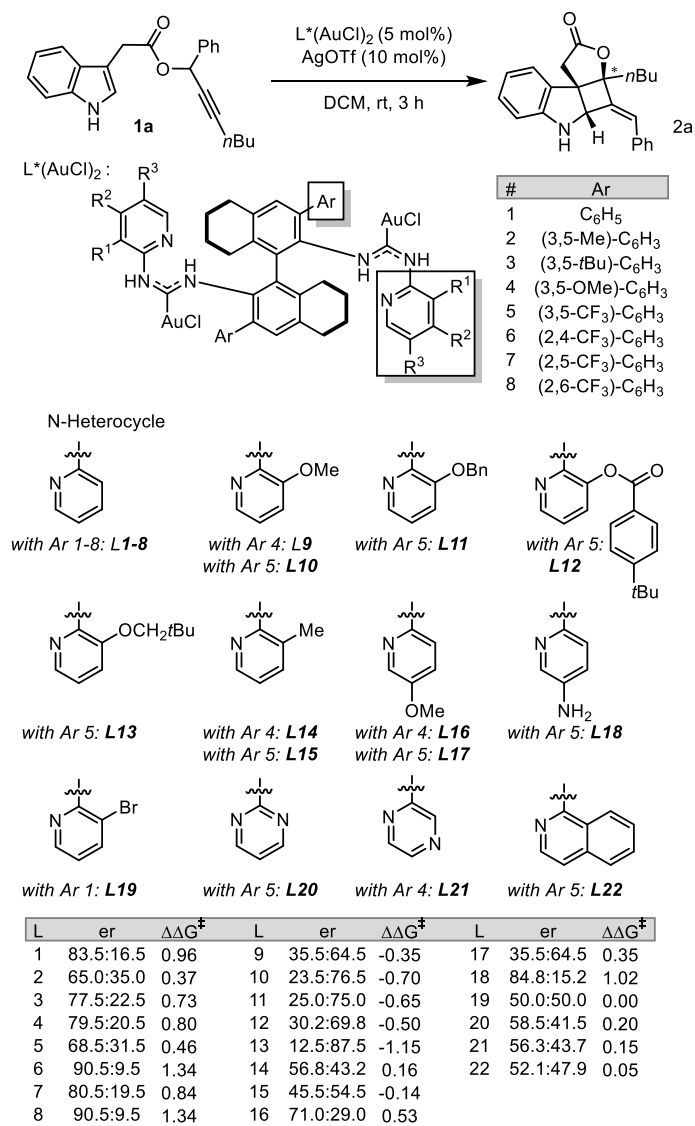


Figure 5.2. Tandem [3,3]-sigmatropic rearrangement-[2+2]-cyclization under study and results from an initial screen.

heterocycles were considered but found ineffectual (*vide infra*). The backbone was chosen to be constant as the H₈-BINAM scaffold was crucial for easy ligand purification and stabilization.

The initial training set revealed a few notable observations. First, the enantioselectivity induced by varying the aryl group was relatively large, spanning a range from 90.5:9.5 to 65.0:35.0 ($\Delta\Delta G^\ddagger = 1.34$ to 0.37 kcal/mol) with the best performers being electron-withdrawing. Secondly, non-pyridine heterocycles resulted in nearly racemic products. Lastly, substitution at R¹ had a profound influence on selectivity, wherein the facial selection was switched upon replacement of hydrogen by an oxygen substituent. In an effort to model these effects, we chose to model two individual surrogate structures containing the aryl group and heterocycles. This additionally drastically reduced the computational load, allowing for more rapid modeling.

To simulate the two diversity points, computational molecular models were constructed (Figure 5.3). The aryl group was visualized using a biaryl carboxylic acid that allowed for the torsion between the aryl group and the backbone to be simulated. It should be noted that other structures were considered including a simple aryl carboxylic acid and a methoxy biaryl moiety. These were each discarded in favor of the biaryl carboxylic acid, computed using M06-2x and def2TZVP.¹² The heterocycle attached to the diaminocarbene was simulated (with M06-2x and jun-cc-PVTZ¹³) using a urea structure that conserved a hydrogen bond between the terminal urea hydrogen and the heterocycle, an initial design element. Ground state geometries were optimized and various molecular descriptors were extracted. These parameters included charges,¹⁴ molecular distances, IR frequencies and intensities,¹⁵ and molecular size measurements.¹⁶

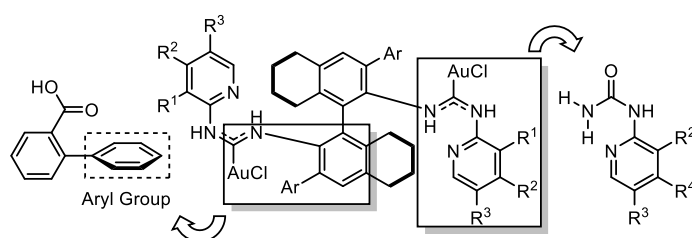


Figure 5.3. Two surrogate molecules were computationally constructed to analyze the appropriate aryl and heterocycle structures.

With the parameters in hand we analyzed the initial results. The nearly racemic reactions from the nonpyridine heterocycles were of particular interest, prompting the hypothesis that some ligands may be reacting in a mechanistically distinct manner. To evaluate this possibility, we sought out single parameter correlations where the non-pyridine heterocycles were found to be outliers (Figure 5.4).¹⁷ This resulted in the identification that the proposed hydrogen bond between the heterocycle nitrogen and the terminal urea hydrogen was either significantly longer or shorter for each of the three non-pyridine heterocycles.

Having gained an understanding of the role of the heterocycle, we returned to the observation of selectivity inversion due to substitution at R¹. We again searched for univariate correlations to the reaction outcomes, with additional parameters seeking to specifically probe this question. It was identified that oxygen substitution resulted in a distorted sp² carbon at C³ of the arene, wherein the R¹-C³-C² angle was significantly less than the idealized 120°. For example, methoxy substitution at R¹ resulted in an angle of 115°, whereas the similarly sized methyl substitution results in an R¹-C³-C² angle of 121°. Despite the similar size, the methoxy substitution yields a smaller R¹-C³-C² angle, indicating a plausible attractive interaction between the oxygen and the internal urea hydrogen. Indeed, upon measuring the distance from R¹ to the internal urea hydrogen, clustering of the substitution patterns is revealed with high sensitivity to $\Delta\Delta G^\ddagger$ (Figure 5.5). Specifically, hydrogen or oxygen substitution about R¹ yielded a range of enantioselectivity, whereas other atoms resulted in nearly racemic reactions.

To further confirm the presumed hydrogen bonding framework, we selected a novel scaffold for synthesis and crystallization containing -OCH₂(1-adamantyl) at R¹.

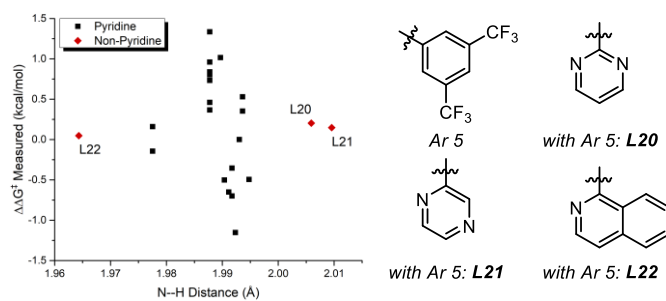


Figure 5.4. Nonpyridine heterocycles were outliers compared to the pyridines.

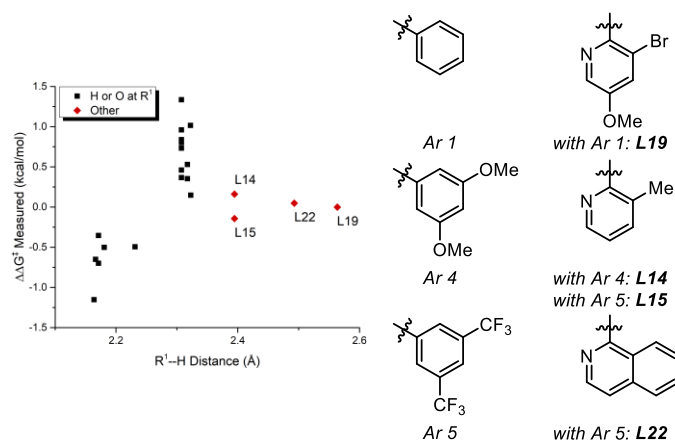


Figure 5.5. The nature of the R¹ atom had a significant effect on enantioselectivity.

Solid state analysis (Figure 5.6) confirmed our suspicions, where the O-C³-C² angle was matched with the computed surrogate (115° for both). Pleasingly, this result indicates that the surrogate structures are accurately portraying the relevant structural features of the heterocycles, inspiring confidence in the previously identified trends.

Returning to the initial training set, we removed the six outlier structures that were presumed to react in a mechanistically distinct manner. Multivariate modeling was recommenced, and fortunately, a surprisingly simple model quickly emerged that contained two parameters: the NBO charge of the carbonyl carbon atom (NBO_C) from the biaryl carboxylic acid, and the distance between R¹ to the internal urea hydrogen (Figure 5.7). This model, identified with 16 training set ligand results, accurately describes 6 validation points. One final external validation was well-predicted, confirming the statistical robustness of the model. In sum, the predicted versus measured values are in excellent agreement with an R² of 0.90 and an average error of 0.21 kcal/mol.

The simplicity of the overall model rendered a facile interpretation. The R¹-H distance, as previously noted, primarily dictates the facial selectivity. Both hydrogen and oxygen substitutions result in a clustering of distances, with oxygen substitutions being closer to the urea hydrogen. The binary effect of this substitution can be implicated as the origin of bifurcation of enantioselectivity in the overall reaction, despite the (*S*)-enantiomer of the binaphthyl backbone being maintained throughout all catalysts. Therefore, the degree of enantioselectivity is primarily dictated by the aryl group via through space and inductive effects, as represented by NBO_C. Complexes that induce more positive enantioselectivity contain 2-substituted aryl groups (**L6-8**) which reorients the dihedral between the arene and the backbone (aryl-aryl dihedral = 80-88°).

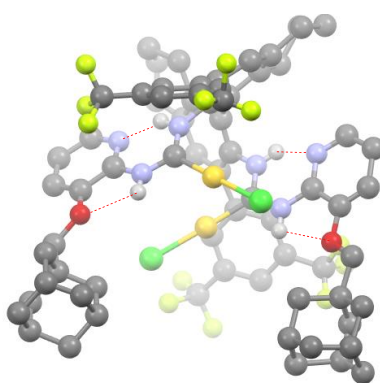


Figure 5.6. Crystal structure of complex $L23^*(AuCl_2)_2$.

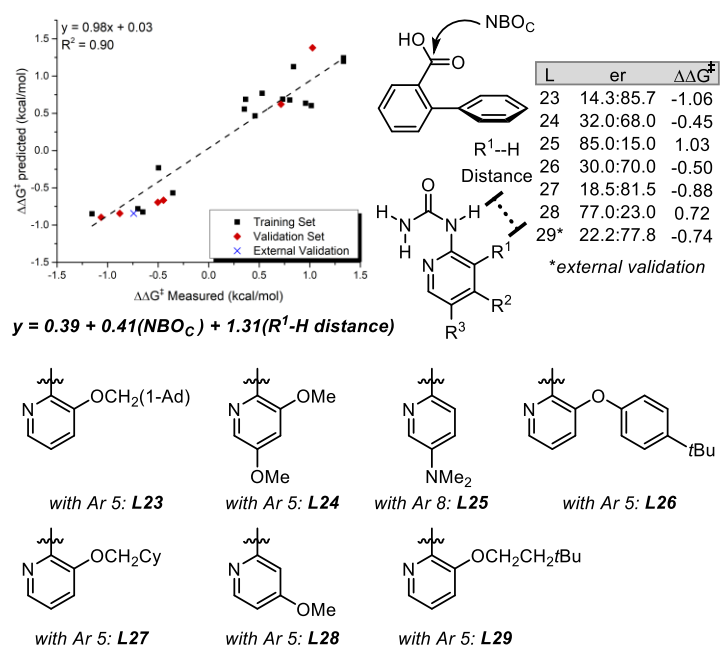


Figure 5.7. Overall multivariate model containing training and validation sets, as well as an external validation.

Accordingly, each of the simulated biaryl carboxylic acids have relatively higher charges on the carbonyl carbon, with the highest enantioselectivity being associated with the highest NBO_C (2,6-(CF₃)₂C₆H₃ **L8**, $\Delta\Delta G^\ddagger = 1.35$, $NBO_C = 0.788$). Intriguingly, the biaryl carboxylic acid accurately recreates the differing reactivity between 2,6-(CF₃)₂C₆H₃ and 3,5-(CF₃)₂C₆H₃. In essence, use of 3,5-(CF₃)₂C₆H₃ results in a more negative selectivity, and this result is mirrored in the NBO_C , with a relatively less positive charge (0.777). This result can be attributed to the aryl-aryl ring overlap and the dihedral angle between the carboxylic acid and the aryl ring. For example, the 3,5 substituted biaryl carboxylic acid structures (aryl group 1-5) each contain a similar aryl-aryl dihedral (50-55°). However, the 3,5-CF₃ arene contains the most overlap between the carboxylic acid and the aryl ring (dihedral = 20° versus 27-31°) resulting in a less positively charged carbon. The ability to describe the nuanced effects of the aryl ring substitution highlights the utility of the computed biaryl carboxylic acid structures.

Satisfied by the simple model offering easy interpretation, we returned to optimizing the rearrangement-cyclization reaction under study. Proposed catalyst structures to increase enantioselectivity were not synthetically plausible; therefore, we focused on augmenting other reaction factors. Due to the importance of the hydrogen bonding network, we hypothesized that a less polar solvent would facilitate a better reaction. Indeed, upon changing the solvent from dichloromethane to toluene, higher yields and enantioselectivities were obtained. Importantly, the selectivity trends did not change (Figure 5.8). A small array of substrates was tested that displayed the utility of this reaction as well as some limitations (Figure 5.9). Substituted indoles were generally well tolerated, with the exception of substitution about C⁴. Bulkier substituents at R''

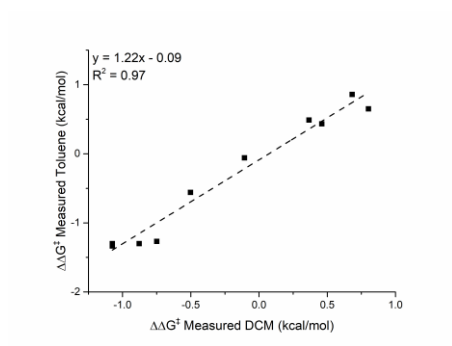


Figure 5.8. Comparison of reaction enantioselectivity between dichloromethane (DCM) and toluene.

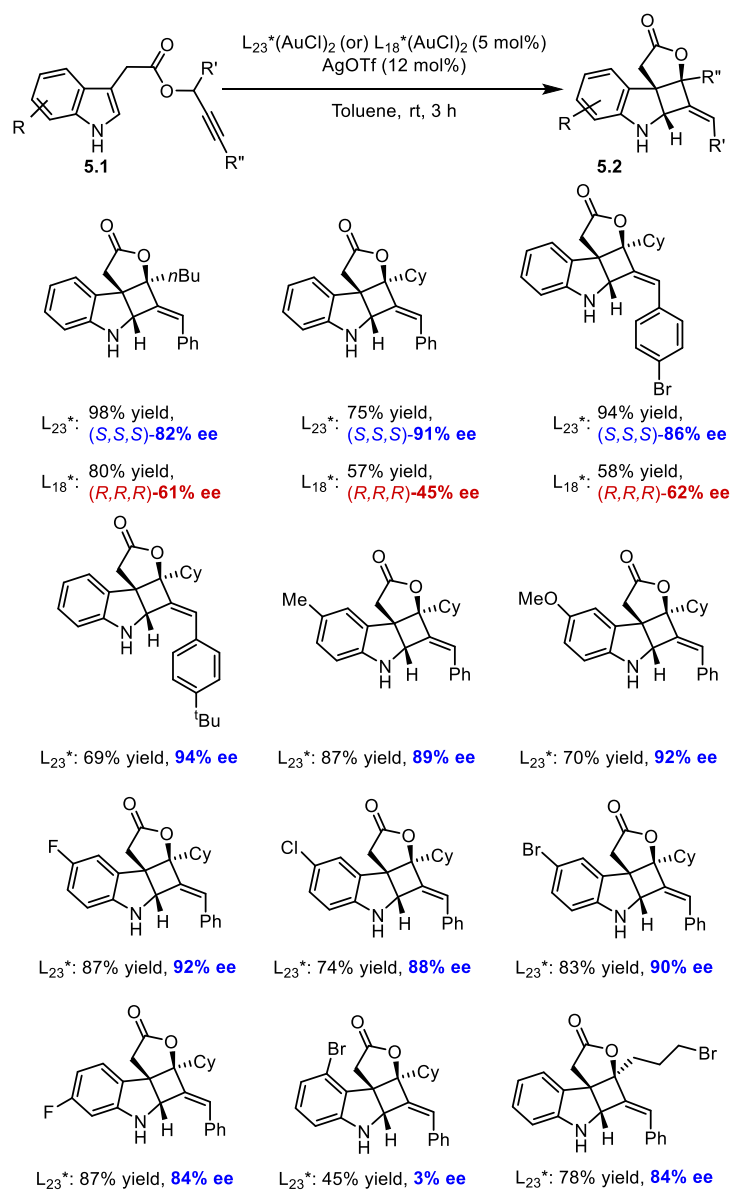


Figure 5.9. Substrate scope of [3,3]-sigmatropic rearrangement-[2+2]-cyclization

increased the enantiodiscrimination when **L23** was utilized; however, an opposite effect was observed with **L18**.

Conclusion

In total, a gold catalyzed [3,3]-sigmatropic rearrangement-[2+2]-cyclization reaction was used to interrogate acyclic diaminocarbene ligands. Computational modeling of surrogate structures identified the disparate role of the aryl group and the heterocycle structure, a surprising result. The ability to identify nonintuitive results displays the power of molecular modeling for future mechanistic studies.

Experimental

All synthetic work was completed by the Toste team and thus only computational work is detailed here.

Biaryl carboxylic acids used for parameterization were submitted to a geometry optimization in Gaussian 09¹⁸ using the Def2TZVP basis set and M06-2x functional. This basis set and functional has been shown to be accurate for a large number of main group systems.^{12, 19} Input geometry for the unsubstituted biaryl carboxylic acid used a 90° dihedral angle between the two aryl rings, and a 0° dihedral angle between the carboxylic acid and the aryl ring. The –OH moiety of the carboxylic acid was pointed away from the second aryl ring. The optimized geometry of the unsubstituted biaryl carboxylic acid was used as the starting point for all subsequent calculations, with the 2-substitution being deemed the carbon closer in space to the carboxylic acid. Geometry optimization was then carried out on these structures.

Urea molecules used for parameterization were submitted to a geometry optimization in Gaussian 09 using the Jun-CC-pVTZ basis set and M06-2x functional. This basis set was chosen as a compromise between computation efficiency and accuracy with possible hydrogen bonding interactions.¹³ Input geometry for the unsubstituted pyridine-urea ($R^2, R^3, R^4 = H$) used a fully planar molecule. Output from this geometry optimization was used to build the input geometries for all subsequent molecules. Input geometries generally utilized planar molecules, with the exception of the $-NMe_2$ group, which had one bond in plane with the pyridine, and one 30° out of plane to conserve the sp^3 hybridization.

Triple zeta potential basis sets were chosen along with the M06-2x functional, as these generally lead to quantitative correlations. Infrared frequency and NBO charge^{14a} distribution calculations were carried out on the optimized geometry. Linear scaling factors were not used as this would not affect the correlations.²⁰ All optimized structures lacked any imaginary frequencies and were thus deemed ground states and not transition states. Sterimol values were calculated using Molecular Modeling Pro.²¹ Multivariate models were constructed and analyzed using Matlab Statistical toolbox version 2014a.²²

Figure 5.10 includes the catalyst structures, the computed biaryl carboxylic acids, and the computed urea structures.

Figure 5.11 displays the labels used in Table 5.1, which tabulates the data for the biaryl carboxylic acids. Figure 5.12 displays the labels used in Table 5.2, which tabulates the data for the ureas. Table 5.3 contains the measured versus predicted values for Figure 5.7 as well as the normalized values of the parameters for the same figure.

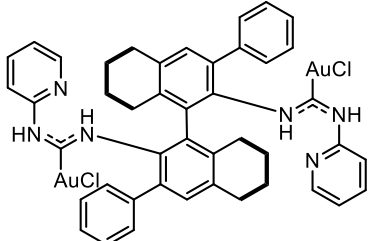
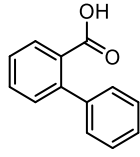
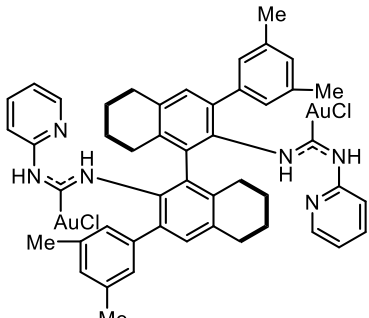
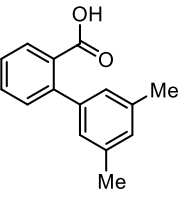
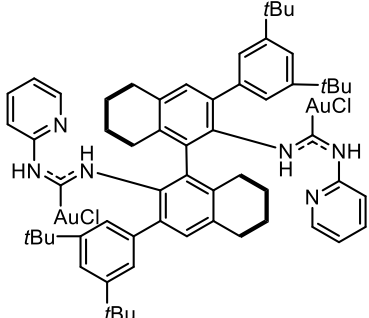
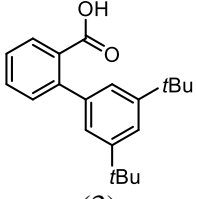
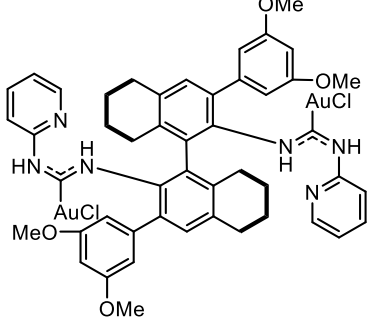
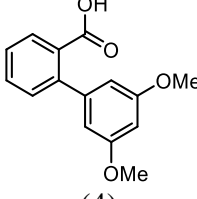
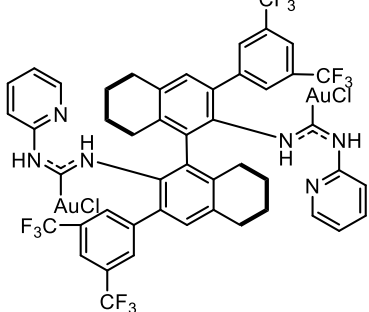
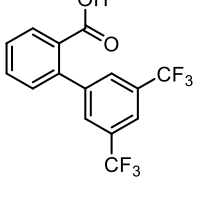
#	Structure	Aryl Group (#)
1		 <p>(1)</p>
2		 <p>(2)</p>
3		 <p>(3)</p>
4		 <p>(4)</p>
5		 <p>(5)</p>

Figure 5.10. Catalysts and the computed surrogate structures.

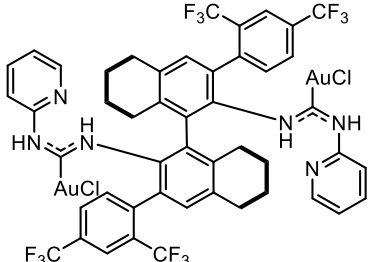
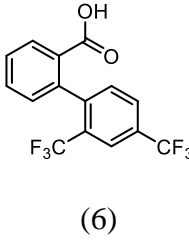
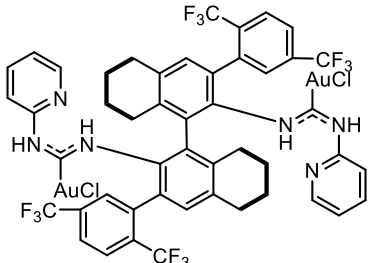
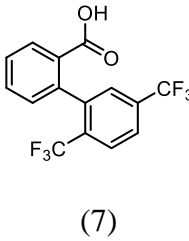
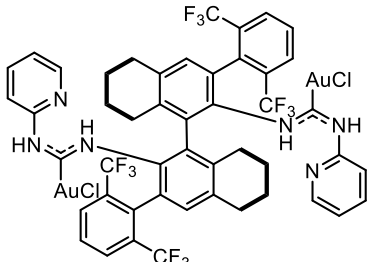
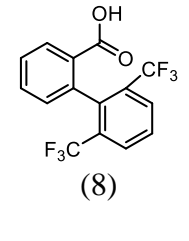
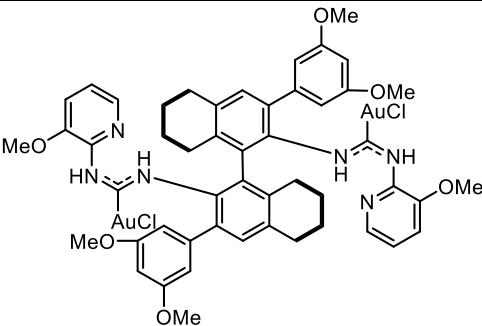
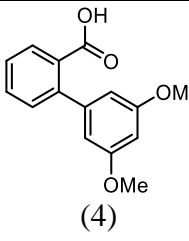
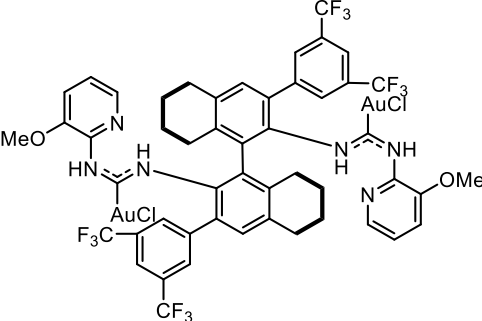
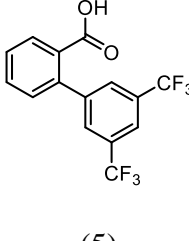
#	Structure	Aryl Group (#)
6		 <p>(6)</p>
7		 <p>(7)</p>
8		 <p>(8)</p>
9		 <p>(4)</p>
10		 <p>(5)</p>

Figure 5.10. Continued.

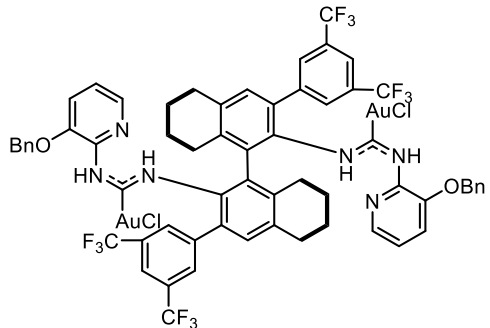
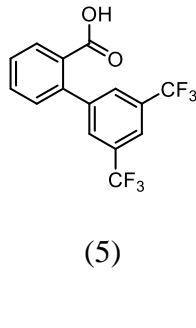
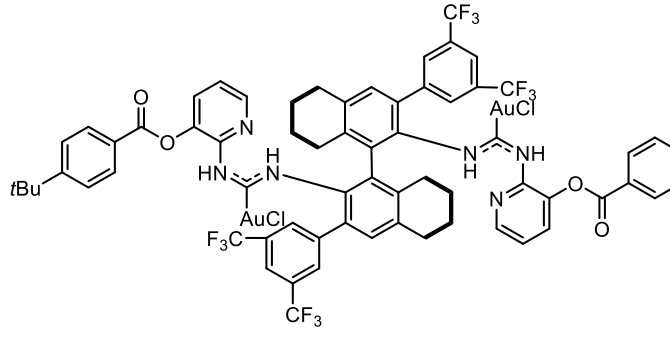
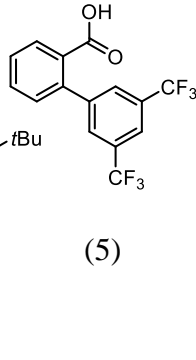
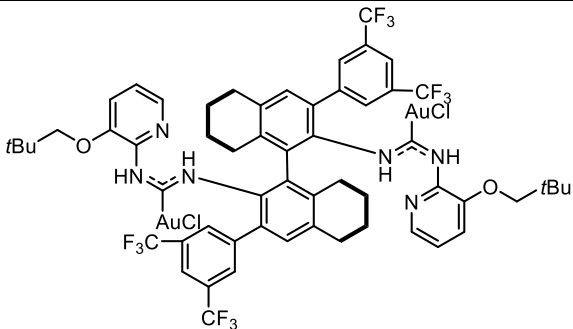
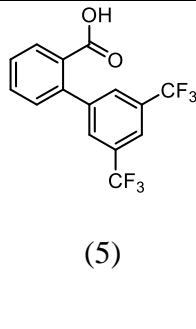
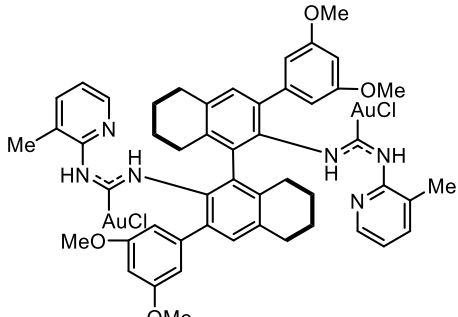
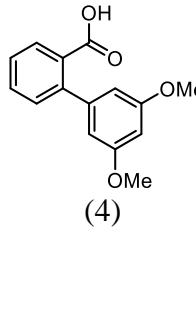
#	Structure	Aryl Group (#)
11		 <p>(5)</p>
12		 <p>(5)</p>
13		 <p>(5)</p>
14		 <p>(4)</p>

Figure 5.10. Continued.

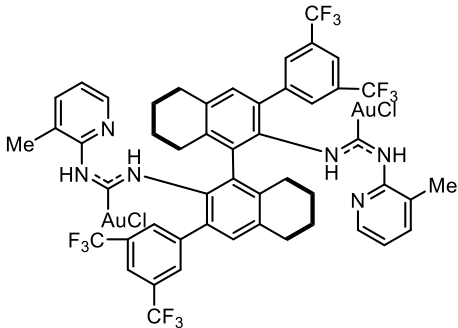
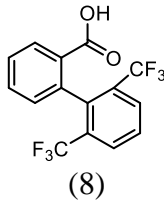
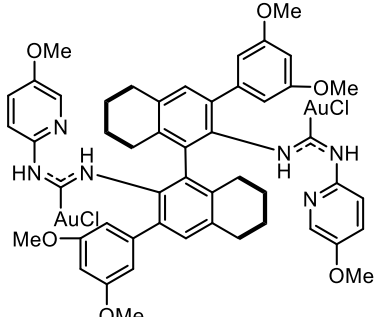
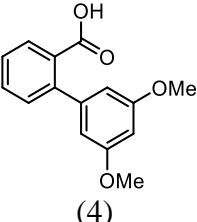
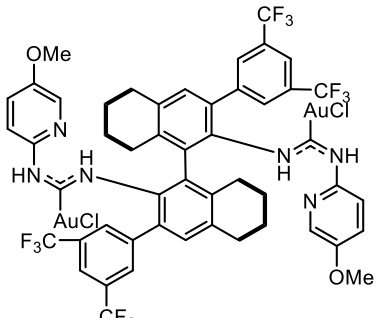
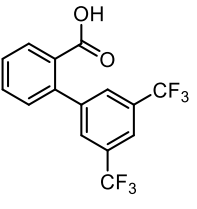
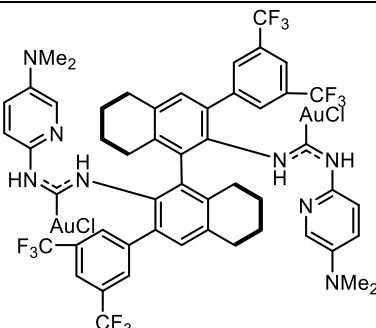
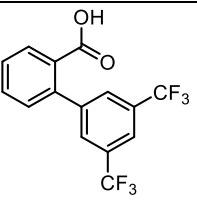
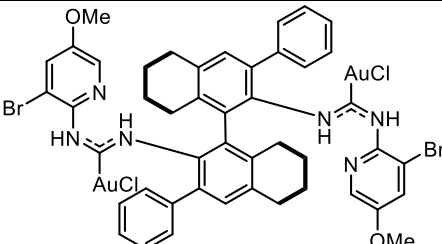
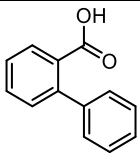
#	Structure	Aryl Group (#)
15		 <p>(8)</p>
16		 <p>(4)</p>
17		 <p>(5)</p>
18		 <p>(5)</p>
19		 <p>(1)</p>

Figure 5.10. Continued.

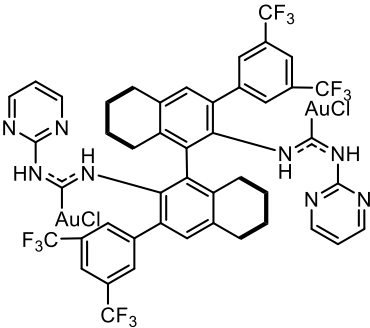
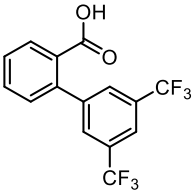
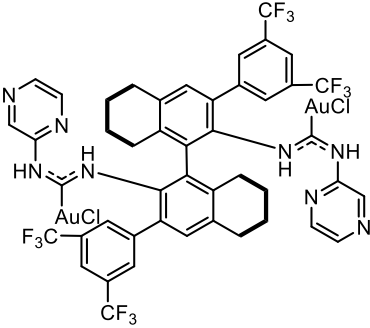
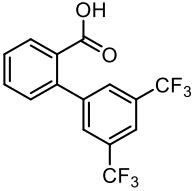
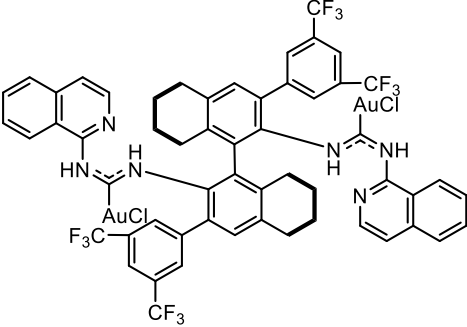
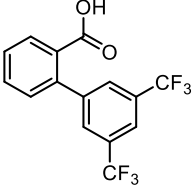
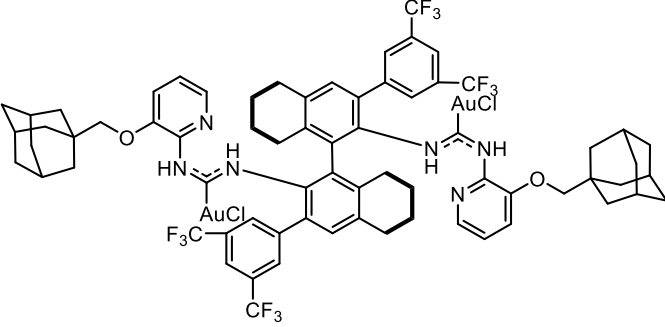
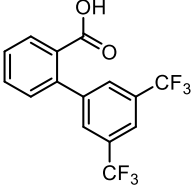
#	Structure	Aryl Group (#)
20		 (5)
21		 (5)
22		 (5)
23		 (5)

Figure 5.10. Continued.

#	Structure	Aryl Group (#)
24		<p>(5)</p>
25		<p>(8)</p>
26		<p>(5)</p>
27		<p>(5)</p>

Figure 5.10. Continued.

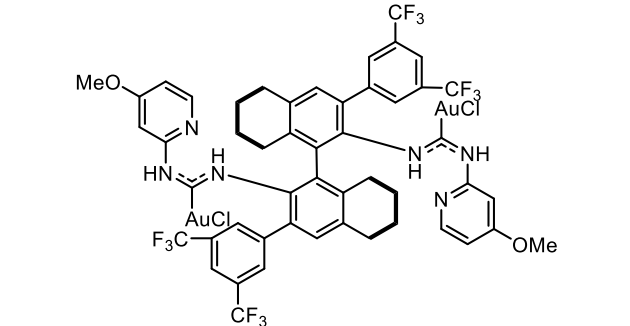
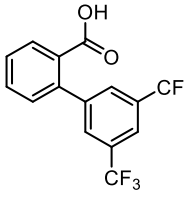
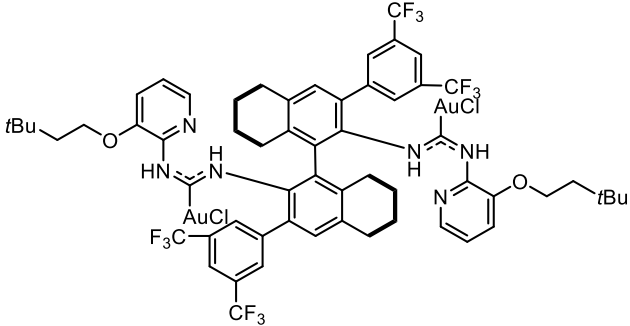
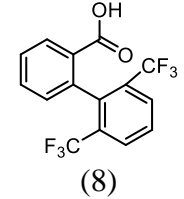
#	Structure	Aryl Group (#)
28		 <p>(5)</p>
29		 <p>(8)</p>

Figure 5.10. Continued.

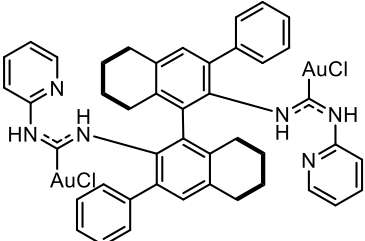
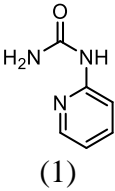
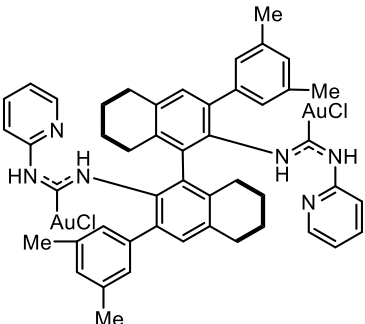
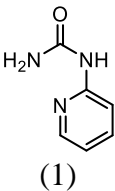
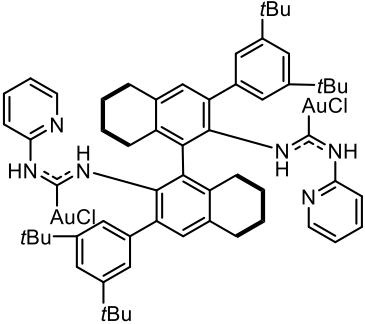
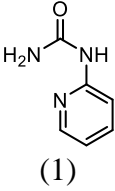
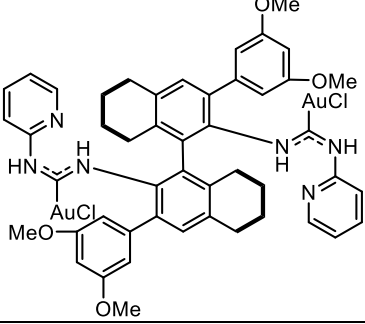
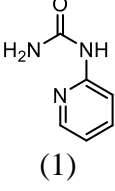
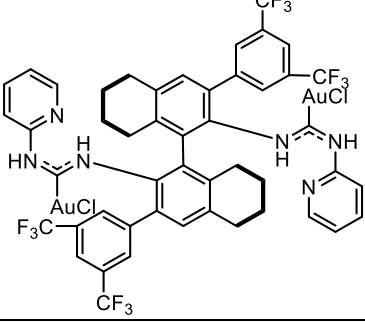
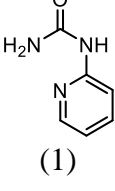
#	Structure	Urea (#)
1		 (1)
2		 (1)
3		 (1)
4		 (1)
5		 (1)

Figure 5.10. Continued.

#	Structure	Urea (#)
6		<p>(1)</p>
7		<p>(1)</p>
8		<p>(1)</p>
9		<p>(2)</p>
10		<p>(2)</p>

Figure 5.10. Continued.

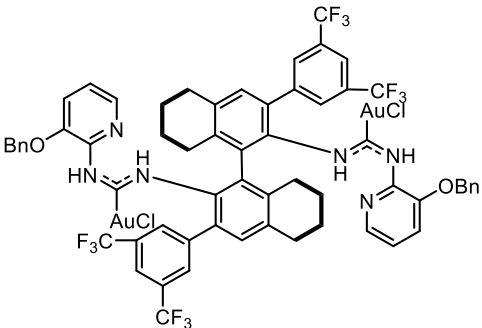
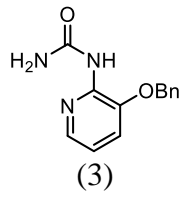
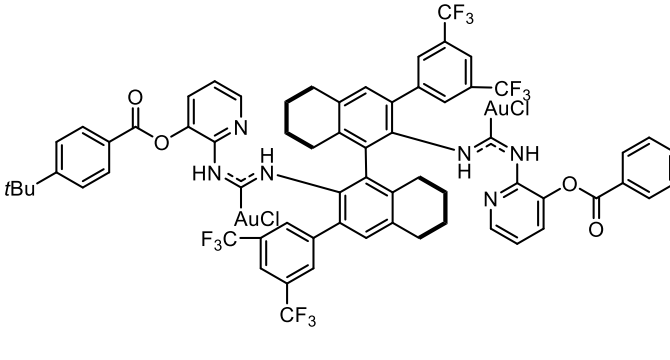
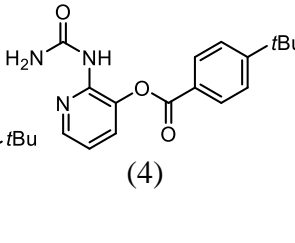
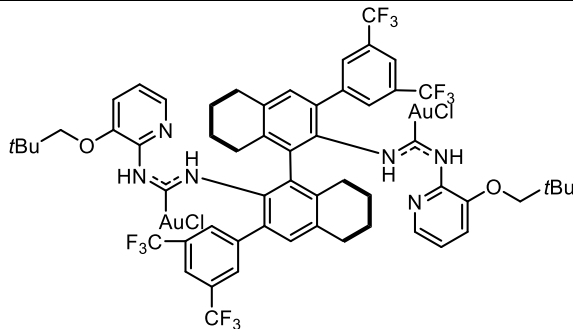
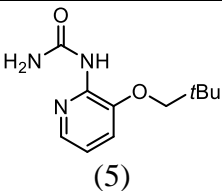
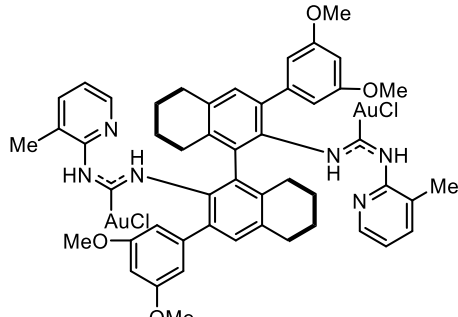
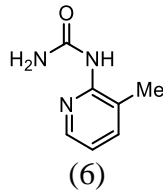
#	Structure	Urea (#)
11		 (3)
12		 (4)
13		 (5)
14		 (6)

Figure 5.10. Continued.

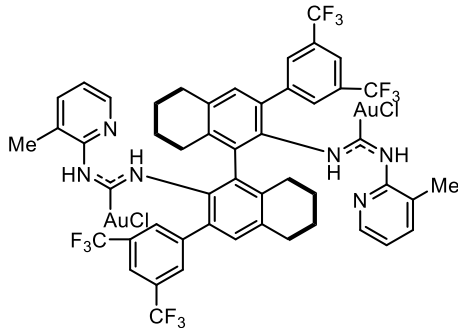
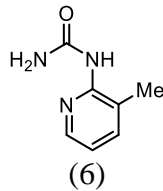
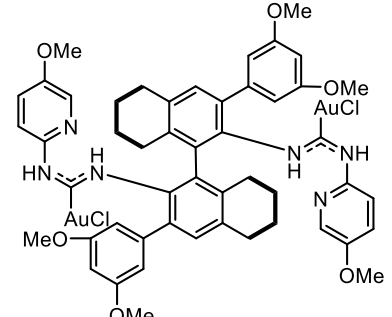
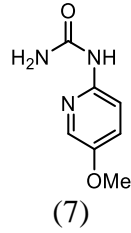
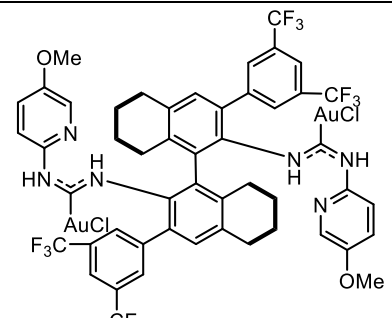
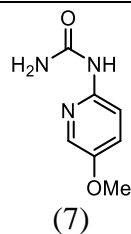
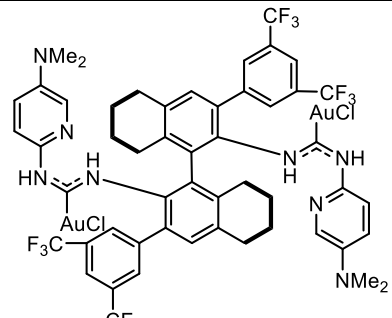
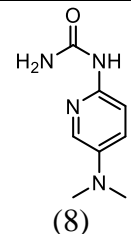
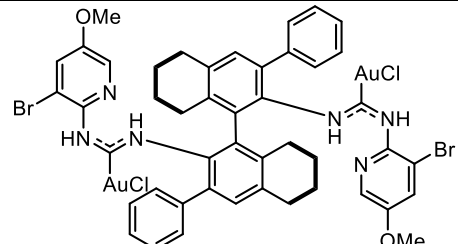
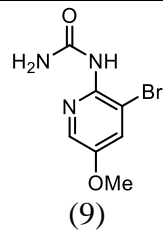
#	Structure	Urea (#)
15		 <p>(6)</p>
16		 <p>(7)</p>
17		 <p>(7)</p>
18		 <p>(8)</p>
19		 <p>(9)</p>

Figure 5.10. Continued.

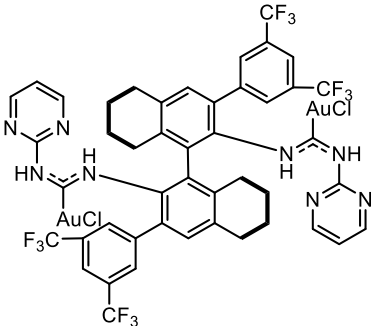
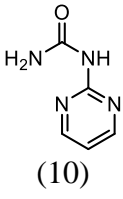
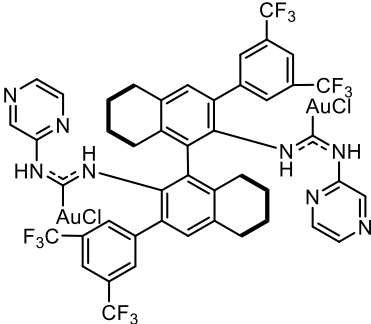
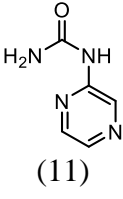
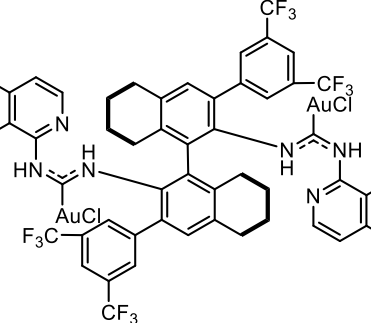
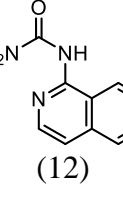
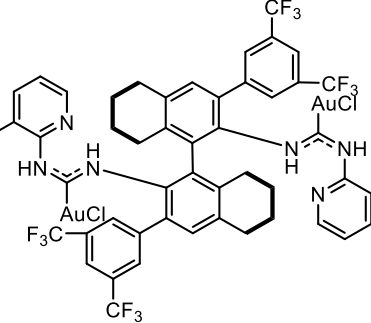
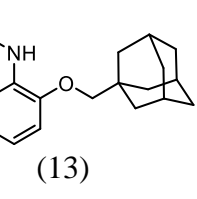
#	Structure	Urea (#)
20		 <p>(10)</p>
21		 <p>(11)</p>
22		 <p>(12)</p>
23		 <p>(13)</p>

Figure 5.10. Continued.

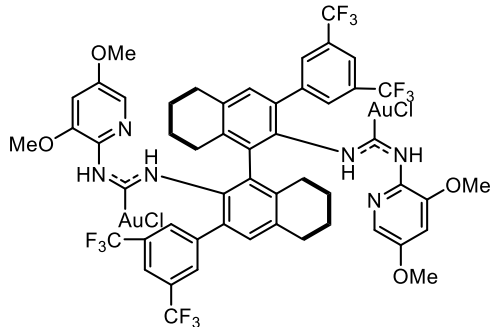
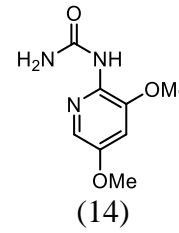
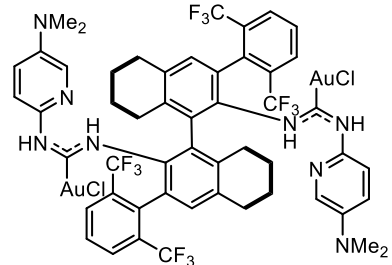
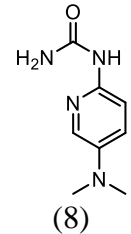
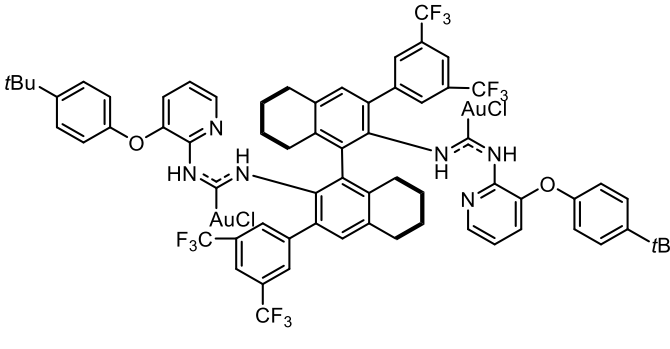
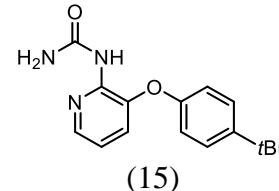
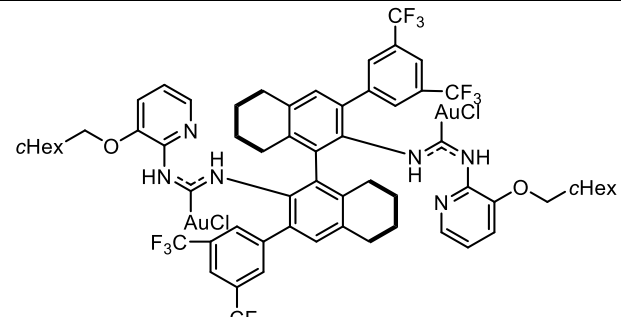
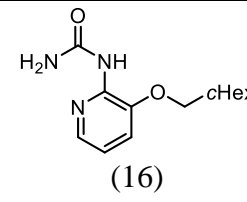
#	Structure	Urea (#)
24		 <p>(14)</p>
25		 <p>(8)</p>
26		 <p>(15)</p>
27		 <p>(16)</p>

Figure 5.10. Continued.

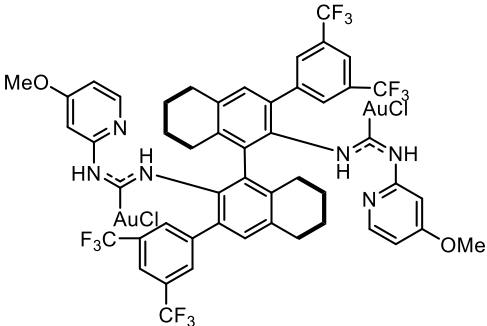
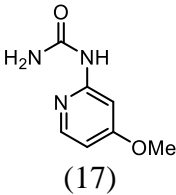
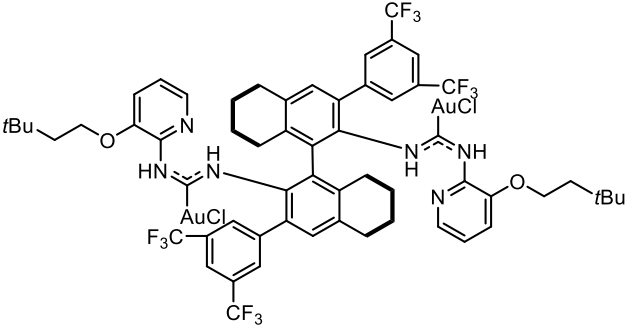
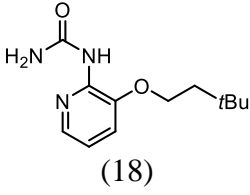
#	Structure	Urea (#)
28		 <p>(17)</p>
29		 <p>(18)</p>

Figure 5.10. Continued.

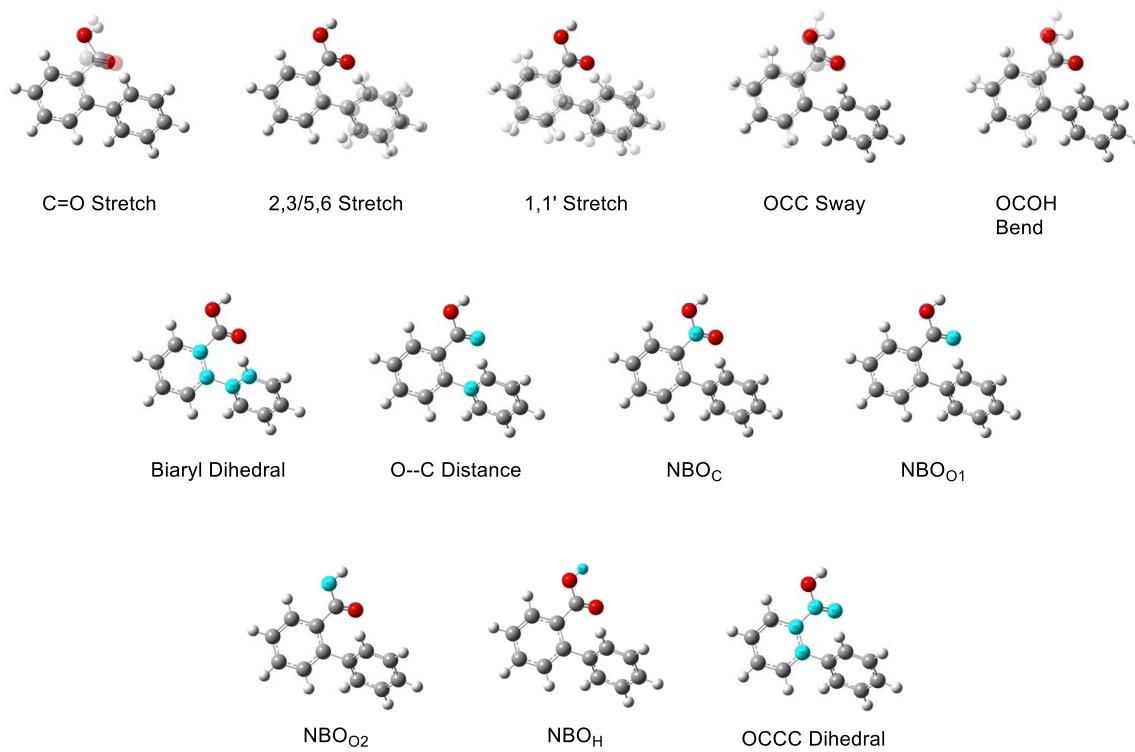


Figure 5.11. Labels used for biaryl carboxylic acids.

Table 5.1. Tabulated data for biaryl carboxylic acids.

Biaryl Carboxylic acid #	C=O stretch Frequency (cm ⁻¹)	C=O Stretch Intensity	2,3/5,6 Stretch Frequency (cm ⁻¹)	2,3/5,6 Stretch Intensity	1,1' Stretch Frequency (cm ⁻¹)	1,1' Stretch Intensity
1	1858.34	341.1736	1688.33	1.0418	1558.90	2.7241
2	1857.77	342.1896	1685.94	11.3233	1548.29	13.3398
3	1859.04	336.3355	1677.51	25.8803	1545.59	31.9882
4	1863.37	340.6566	1694.34	142.4133	1552.38	25.8095
5	1855.24	355.1680	1701.23	5.3772	1678.04	6.5687
6	1854.09	360.8599	1707.51	38.7875	1572.63	4.2720
7	1851.38	362.8027	1705.80	2.1496	1544.48	13.6410
8	1849.34	361.5283	1690.77	13.9801	1554.57	6.7959

Biaryl Carboxylic acid #	OCC Sway Frequency (cm ⁻¹)	OCC Sway Intensity	OCOH Bend Frequency (cm ⁻¹)	OCOH Bend Intensity	Biaryl Dihedral (°)	O--C Distance (Å)
1	1388.10	115.2057	1222.86	219.1623	54.41	2.91940
2	1385.48	115.2831	1218.27	193.8588	53.66714	2.93723
3	1385.80	110.4202	1219.03	195.6319	50.94804	2.94753
4	1386.55	113.5134	1224.03	168.2045	54.22598	2.94595
5	1392.83	134.5383	1220.02	192.8528	55.51729	2.85557
6	1398.04	145.8788	1222.42	189.9250	80.26448	2.76589
7	1395.47	128.0073	1221.36	207.9752	82.19531	2.75754
8	1396.24	142.4949	1220.61	181.7475	88.27557	2.72472

Biaryl Carboxylic acid #	NBO _C	NBO _{O1}	NBO _{O2}	NBO _H	OCCC Dihedral (°)
1	0.77962	-0.57415	-0.68885	0.49707	27.34645
2	0.78035	-0.57490	-0.68901	0.49600	29.08915
3	0.78037	-0.57616	-0.68884	0.49543	30.04504
4	0.78022	-0.57290	-0.68806	0.49575	31.20879
5	0.77732	-0.57847	-0.68341	0.50020	20.2494
6	0.78729	-0.58453	-0.68256	0.50066	16.35259
7	0.78631	-0.58425	-0.68338	0.50080	13.75359
8	0.78793	-0.58741	-0.68394	0.50060	4.15664

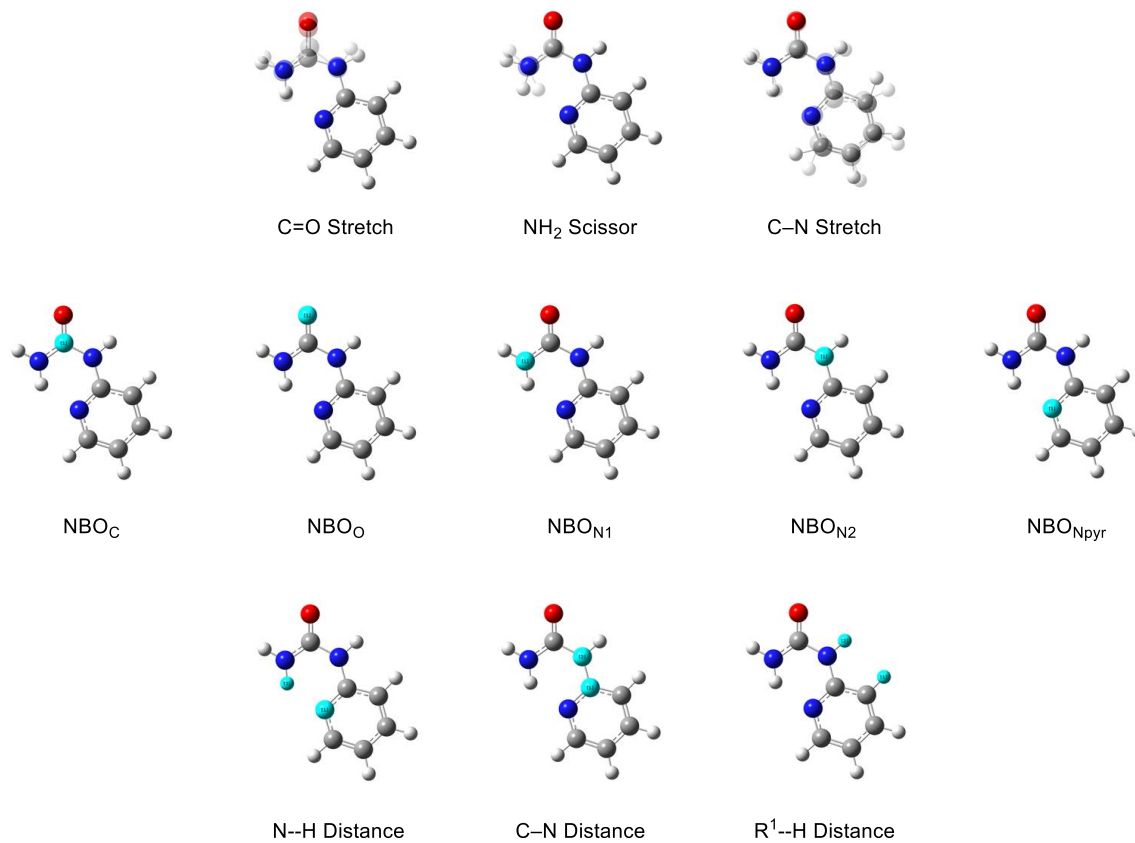


Figure 5.12. Labels used for ureas.

Table 5.2. Tabulated data for ureas.

Urea (#)	C=O Stretch Frequency (cm ⁻¹)	C=O Stretch intensity	NH ₂ Scissor Frequency (cm ⁻¹)	NH ₂ Scissor intensity	C-N Stretch Frequency (cm ⁻¹)	C-N Stretch intensity
1	1812.26	719.8500	1593.91	420.2538	1539.53	134.5852
2	1809.28	741.5668	1596.02	452.3287	1556.00	401.0913
3	1810.35	670.8827	1596.60	463.4122	1555.41	378.9649
4	1815.44	674.1773	1597.21	439.2809	1551.15	345.7587
5	1807.86	689.5108	1596.56	467.3407	1554.21	382.3888
6	1809.05	695.9058	1591.84	438.1336	1537.68	255.3079
7	1806.80	764.7300	1596.51	346.2401	1559.79	487.5909
8	1804.17	799.7262	1597.21	371.2573	1560.89	489.5687
9	1811.88	715.9719	1592.88	360.1643	1553.68	613.3307
10	1818.21	703.7302	1598.82	394.2805	1545.92	464.3906
11	1820.30	720.7243	1600.44	370.5854	1538.73	207.3897
12	1817.63	697.1746	1591.14	391.2295	1523.99	158.5279
13	1802.79	657.8325	1594.75	471.7443	1553.51	386.1295
14	1805.51	780.7431	1598.50	404.5116	1563.21	581.6123
15	1809.95	724.4114	1596.06	488.0869	1551.71	383.9920
16	1807.63	686.7122	1595.65	473.4317	1554.28	384.1221
17	1809.93	708.1454	1590.92	481.5817	1532.96	206.3635
18	1807.76	704.6705	1596.09	471.1118	1553.30	375.3427

Urea (#)	NBO _C	NBO _O	NBO _{N1}	NBO _{N2}	NBO _{Npvr}
1	0.80419	-0.66130	-0.84622	-0.63986	-0.52532
2	0.80474	-0.65987	-0.84750	-0.64497	-0.51350
3	0.80503	-0.65970	-0.84751	-0.64573	-0.51214
4	0.80453	-0.65350	-0.85649	-0.64740	-0.51634
5	0.80450	-0.66167	-0.84743	-0.64550	0.51400
6	0.80597	-0.66282	-0.84551	-0.64834	-0.52275
7	0.80293	-0.66560	-0.84855	-0.64282	-0.50787
8	0.80280	-0.66756	-0.84910	-0.64218	-0.50936
9	0.80536	-0.65673	-0.84631	-0.64884	-0.49558
10	0.80379	-0.65054	-0.84546	-0.63834	-0.54423
11	0.80401	-0.65253	-0.84395	-0.63838	-0.49172
12	0.80624	-0.66026	-0.84272	-0.63995	-0.54222
13	0.80517	-0.66255	-0.84759	-0.64551	-0.51244
14	0.80395	-0.66432	-0.84986	-0.64810	-0.49508
15	0.80405	-0.65940	-0.84796	-0.64418	-0.51433
16	0.80483	-0.66200	-0.84776	-0.64553	-0.51317

Table 5.2 continued.

Urea (#)	NBO _C	NBO _O	NBO _{N1}	NBO _{N2}	NBO _{Npyr}
17	0.80446	-0.66320	-0.84730	-0.63916	-0.54708
18	0.80425	-0.66133	-0.84790	-0.64539	-0.51487

Urea (#)	N--H Distance (Å)	C--N Distance (Å)	R ₂ --H Distance (Å)
1	1.988	1.383	2.307
2	1.992	1.379	2.171
3	1.991	1.379	2.167
4	1.995	1.379	2.231
5	1.992	1.380	2.164
6	1.978	1.385	2.395
7	1.994	1.389	2.317
8	1.990	1.389	2.322
9	1.993	1.381	2.564
10	2.006	1.384	*
11	2.010	1.378	2.323
12	1.964	1.379	2.493
13	1.990	1.378	2.159
14	1.997	1.384	2.184
15	1.990	1.379	2.181
16	1.991	1.380	2.165
17	1.979	1.384	2.325
18	1.991	1.379	2.165

Table 5.3. Values for Figure 5.7.

Ligand	Measured $\Delta\Delta G^\ddagger$ (kcal/mol)	Predicted $\Delta\Delta G^\ddagger$ (kcal/mol)	Normalized NBO _C	Normalized R ¹ —H (Å)
1	0.960	0.634	0.04236	0.147
2	0.367	0.687	0.25387	0.147
3	0.732	0.689	0.25966	0.147
4	0.803	0.678	0.21620	0.147
5	0.460	0.465	-0.62403	0.147
6	1.335	1.196	2.26464	0.147
7	0.840	1.124	1.98070	0.147
8	1.335	1.243	2.45007	0.147
9	-0.354	-0.569	0.21620	-1.102
10	-0.699	-0.782	-0.62403	-1.102
11	-0.651	-0.826	-0.62403	-1.145
12	-0.495	-0.233	-0.62403	-0.552
13	-1.152	-0.849	-0.62403	-1.169
16	0.530	0.767	0.21620	0.237
17	0.354	0.554	-0.62403	0.237
18	1.016	0.601	-0.62403	0.284
23	-1.063	-0.897	-0.62403	-1.217
24	-0.446	-0.666	-0.62403	-0.985
25	1.027	1.380	2.45007	0.284
26	-0.502	-0.695	-0.62403	-1.015
27	-0.878	-0.843	-0.62403	-1.163
28	0.716	0.622	-0.62403	0.305
29	-0.741	-0.844	-0.62403	-1.164

References

1. (a) Dorel, R.; Echavarren, A. M., Gold(I)-Catalyzed Activation of Alkynes for the Construction of Molecular Complexity. *Chem. Rev.* **2015**, *115* (17), 9028-9072; (b) Joost, M.; Amgoune, A.; Bourissou, D., Reactivity of Gold Complexes towards Elementary Organometallic Reactions. *Angew. Chem. Int. Ed.* **2015**, *54* (50), 15022-15045; (c) Pflasterer, D.; Hashmi, A. S. K., Gold Catalysis in Total Synthesis - Recent Achievements. *Chem. Soc. Rev.* **2016**, *45* (5), 1331-1367; (d) Miró, J.; del Pozo, C., Fluorine and Gold: A Fruitful Partnership. *Chem. Rev.* **2016**, *116* (19), 11924-11966; (e) Wei, Y.; Shi, M., Divergent Synthesis of Carbo- and Heterocycles via Gold-Catalyzed Reactions. *ACS Catalysis* **2016**, *6* (4), 2515-2524.
2. Gorin, D. J.; Sherry, B. D.; Toste, F. D., Ligand Effects in Homogeneous Au Catalysis. *Chem. Rev.* **2008**, *108* (8), 3351-3378.
3. Marion, N.; Nolan, S. P., N-Heterocyclic Carbenes in Gold Catalysis. *Chem. Soc. Rev.* **2008**, *37* (9), 1776-1782.
4. Zi, W.; Dean Toste, F., Recent Advances in Enantioselective Gold Catalysis. *Chem. Soc. Rev.* **2016**, *45* (16), 4567-4589.
5. Wang, Y.-M.; Lackner, A. D.; Toste, F. D., Development of Catalysts and Ligands for Enantioselective Gold Catalysis. *Acc. Chem. Res.* **2014**, *47* (3), 889-901.
6. (a) Díez-González, S.; Nolan, S. P., Stereoelectronic Parameters Associated with N-Heterocyclic Carbene (NHC) Ligands: A Quest for Understanding. *Coord. Chem. Rev.* **2007**, *251* (5), 874-883; (b) Gusev, D. G., Electronic and Steric Parameters of 76 N-Heterocyclic Carbenes in Ni(CO)₃(NHC). *Organometallics* **2009**, *28* (22), 6458-6461; (c) Dröge, T.; Glorius, F., The Measure of All Rings—N-Heterocyclic Carbenes. *Angew. Chem. Int. Ed.* **2010**, *49* (39), 6940-6952.
7. (a) Cesar, V.; Bellemin-Lapponnaz, S.; Gade, L. H., Chiral N-Heterocyclic Carbenes as StereoDirecting Ligands in Asymmetric Catalysis. *Chem. Soc. Rev.* **2004**, *33* (9), 619-636; (b) Janssen-Muller, D.; Schlepphorst, C.; Glorius, F., Privileged Chiral N-Heterocyclic Carbene Ligands for Asymmetric Transition-Metal Catalysis. *Chem. Soc. Rev.* **2017**, *46* (16), 4845-4854.
8. Bartolomé, C.; García-Cuadrado, D.; Ramiro, Z.; Espinet, P., Synthesis and Catalytic Activity of Gold Chiral Nitrogen Acyclic Carbenes and Gold Hydrogen Bonded Heterocyclic Carbenes in Cyclopropanation of Vinyl Arenes and in Intramolecular Hydroalkoxylation of Allenes. *Inorg. Chem.* **2010**, *49* (21), 9758-9764.
9. Handa, S.; Slaughter, L. M., Enantioselective Alkynylbenzaldehyde Cyclizations Catalyzed by Chiral Gold(I) Acyclic Diaminocarbene Complexes Containing Weak Au-Arene Interactions. *Angew. Chem. Int. Ed.* **2012**, *51* (12), 2912-2915.

10. (a) Wang, Y.-M.; Kuzniewski, C. N.; Rauniyar, V.; Hoong, C.; Toste, F. D., Chiral (Acyclic Diaminocarbene)Gold(I)-Catalyzed Dynamic Kinetic Asymmetric Transformation of Propargyl Esters. *J. Am. Chem. Soc.* **2011**, *133* (33), 12972-12975; (b) Khrakovsky, D. A.; Tao, C.; Johnson, M. W.; Thornbury, R. T.; Shevick, S. L.; Toste, F. D., Enantioselective, Stereodivergent Hydroazidation and Hydroamination of Allenes Catalyzed by Acyclic Diaminocarbene (ADC) Gold(I) Complexes. *Angew. Chem. Int. Ed.* **2016**, *55*, 6079-6083.
11. Zhang, L., Tandem Au-Catalyzed 3,3-Rearrangement-[2 + 2] Cycloadditions of Propargylic Esters: Expeditious Access to Highly Functionalized 2,3-Indoline-Fused Cyclobutanes. *J. Am. Chem. Soc.* **2005**, *127* (48), 16804-16805.
12. Zhao, Y.; Truhlar, D., The M06 Suite of Density Functionals for Main Group Thermochemistry, Thermochemical Kinetics, Noncovalent Interactions, Excited States, and Transition Elements: Two New Functionals and Systematic Testing of Four M06-Class Functionals and 12 Other Functionals. *Theor. Chem. Acc.* **2008**, *120* (1-3), 215-241.
13. Papajak, E.; Zheng, J.; Xu, X.; Leverentz, H. R.; Truhlar, D. G., Perspectives on Basis Sets Beautiful: Seasonal Plantings of Diffuse Basis Functions. *J. Chem. Theory. Comput.* **2011**, *7* (10), 3027-3034.
14. (a) Glendening, E. D.; Landis, C. R.; Weinhold, F., NBO 6.0: Natural Bond Orbital Analysis Program. *J. Comput. Chem.* **2013**, *34* (16), 1429-1437; (b) Weinhold, F., Natural Bond Orbital Analysis: A Critical Overview of Relationships to Alternative Bonding Perspectives. *J. Comput. Chem.* **2012**, *33* (30), 2363-2379; (c) Glendening, E. D.; Landis, C. R.; Weinhold, F., Natural Bond Orbital Methods. *Wiley Interdisciplinary Reviews: Computational Molecular Science* **2012**, *2* (1), 1-42; (d) Santiago, C. B.; Milo, A.; Sigman, M. S., Developing a Modern Approach To Account for Steric Effects in Hammett-Type Correlations. *J. Am. Chem. Soc.* **2016**, *138* (40), 13424-13430.
15. (a) Milo, A.; Bess, E. N.; Sigman, M. S., Interrogating Selectivity in Catalysis Using Molecular Vibrations. *Nature* **2014**, *507* (7491), 210-214; (b) Bess, E. N.; Guptill, D. M.; Davies, H. M. L.; Sigman, M. S., Using IR Vibrations to Quantitatively Describe and Predict Site-Selectivity in Multivariate Rh-Catalyzed C-H Functionalization. *Chem. Sci.* **2015**, *6* (5), 3057-3062; (c) Milo, A.; Neel, A. J.; Toste, F. D.; Sigman, M. S., A Data-Intensive Approach to Mechanistic Elucidation Applied to Chiral Anion Catalysis. *Science* **2015**, *347* (6223), 737-743; (d) Niemeyer, Z. L.; Milo, A.; Hickey, D. P.; Sigman, M. S., Parameterization of Phosphine Ligands Reveals Mechanistic Pathways and Predicts Reaction Outcomes. *Nat. Chem.* **2016**, *8* (6), 610-617.
16. (a) Harper, K. C.; Sigman, M. S., Three-Dimensional Correlation of Steric and Electronic Free Energy Relationships Guides Asymmetric Propargylation. *Science* **2011**, *333* (6051), 1875-1878; (b) Harper, K. C.; Bess, E. N.; Sigman, M. S., Multidimensional Steric Parameters in the Analysis of Asymmetric Catalytic Reactions. *Nat. Chem.* **2012**, *4* (5), 366-374; (c) Verloop, A., *Drug Design Vol. III*. Academic Press: 1976; p 133.

17. Anslyn, E. V.; Dougherty, D. A., *Modern Physical Organic Chemistry*. University Science: Sausalito, CA, 2006.
18. Frisch, M. J.; Trucks, G. W.; Schlegel, H. B.; Scuseria, G. E.; Robb, M. A.; Cheeseman, J. R.; Scalmani, G.; Barone, V.; Mennucci, B.; Petersson, G. A.; Nakatsuji, H.; Caricato, M. L.; X.; Hratchian, H. P.; Izmaylov, A. F.; Bloino, J.; Zheng, G.; Sonnenberg, J. L.; Hada, M.; Ehara, M.; Toyota, K.; Fukuda, R.; Hasegawa, J.; Ishida, M.; Nakajima, T.; Honda, Y.; Kitao, O.; Nakai, H.; Vreven, T.; Montgomery, J. A., Jr.; Peralta, J. E.; Ogliaro, F.; Bearpark, M.; Heyd, J. J.; Brothers, E.; Kudin, K. N.; Staroverov, V. N.; Kobayashi, R.; Normand, J.; Raghavachari, K.; Rendell, A.; Burant, J. C.; Iyengar, S. S.; Tomasi, J.; Cossi, M.; Rega, N.; Millam, N. J.; Klene, M.; Knox, J. E.; Cross, J. B.; Bakken, V.; Adamo, C.; Jaramillo, J.; Gomperts, R.; Stratmann, R. E.; Yazyev, O.; Austin, A. J.; Cammi, R.; Pomelli, C.; Ochterski, J. W.; Martin, R. L.; Morokuma, K.; Zakrzewski, V. G.; Voth, G. A.; Salvador, P.; Dannenberg, J. J.; Dapprich, S.; Daniels, A. D.; Farkas, Ö.; Foresman, J. B.; Ortiz, J. V.; Cioslowski, J.; Fox, D. J. *Gaussian 09, Revision D.01*, Gaussian, Inc.: Wallingford, CT, 2009.
19. Weigend, F.; Ahlrichs, R., Balanced Basis Sets of Split Valence, Triple Zeta Valence and Quadruple Zeta Valence Quality for H to Rn: Design and Assessment of Accuracy. *PCCP* **2005**, *7* (18), 3297-3305.
20. Merrick, J. P.; Moran, D.; Radom, L., An Evaluation of Harmonic Vibrational Frequency Scale Factors. *J. Phys. Chem. A* **2007**, *111* (45), 11683-11700.
21. Quinn, J. A. *Molecular Modeling Pro*, 6.36; Norgwyn Montgomery Software Inc.: North Wales, PA
22. *MATLAB and Statistics Toolbox Release 2014a*, The MathWorks, Inc.: Natick, Massachusetts, United States, 2014.